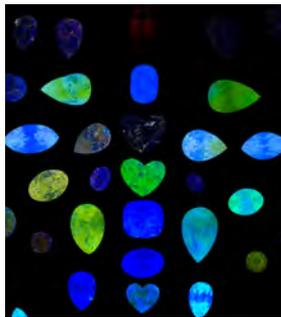Photoluminescence Spectroscopy
for Diamond Analysis

Australian Chrysoberyl

Serpentine from the Italian Alps

2016 Tucson Report

pg. 3

pg. 21

pg. 51

pg. 93

GEMS & GEMOLOGY®

gia.edu/gems-gemology

About the Cover

This issue features G&G's coverage of the 2016 Tucson gem and mineral shows. The cover photo shows Brian Cook's "Wheel of Light" Numinous pendant, which received first place in the AGTA Spectrum Awards' Fashion Forward category. To create the pendant, Mr. Cook drilled a channel into the apex of an 825 ct quartz disk and inserted rough crystals of Paraíba tourmaline, haüyne, ruby, and spessartine garnet. The colors of these crystals are seen as concentric rings. A 24K gold setting, braided leather straps, a rutilated quartz length adjuster, and fire agate beads complete the piece. Photo by Robert Weldon/GIA, courtesy of Brian Cook (Nature's Geometry).

FSC
www.fsc.org
MIX
Paper from
responsible sources
FSC® C006300

Tucson: A Showcase of Colored Gemstone Innovation

Welcome to 2016's first *Gems & Gemology*!

The Tucson shows are renowned for showcasing nature's finest gems and minerals. They're also the venues to see imaginative use of gem materials in unfamiliar combinations. Our cover exemplifies this innovation with the "Wheel of Light"— a spectacular necklace featuring elements of sagenitic quartz, fire agate, Paraíba tourmaline, and braided leather, centered on a clear quartz disk wrapped with 24K gold. The rough gems and minerals placed inside the disk's central axis reflect within the quartz to produce strikingly colored concentric bands. This piece amply demonstrates the ingenuity that makes the Tucson gem and mineral shows such refreshing and vital experiences. We hope you find this issue equally enjoyable.

We offer five feature articles on diverse topics: photoluminescence (PL) spectroscopy, Australian chrysoberyl, Italian serpentine, Tajikistan's variscite, and treated "pistachio" cultured pearls from Tahiti. You'll also find our latest Lab Notes and Micro-World entries, along with in-depth coverage of the February 2016 Tucson shows in our Gem News International section.

Drs. Sally Eaton-Magaña and Christopher M. Breeding of GIA's Carlsbad lab are the authors of our lead article, which provides an overview of PL analysis and its increasing importance for detecting treatment, determining natural or synthetic origin, and verifying origin of color in type II diamonds. PL spectroscopy is now a vital tool for gemologists to authenticate the most valuable large or fancy-color gems.

Photoluminescence spectroscopy is now a vital tool to authenticate the most valuable diamonds.

In our second paper, a team of researchers led by Dr. Karl Schmetzer characterizes the gemological properties and growth structures of chrysoberyl recovered from the sapphire placer deposits in New South Wales, Australia.

Two other articles cover ornamental gem materials: First, Dr. Ilaria Adamo and colleagues offer a detailed mineralogical and gemological investigation of serpentine with gem potential from Pizzo Tremogge in Val Malenco, Italy. Next, Dr. Andrey Litvinenko and his coauthors report on a largely untapped source of the ornamental mineral variscite in central Tajikistan.

Finally, Dr. Chunhui Zhou and his team from GIA's New York lab document the identification of treated pistachio-colored cultured pearls produced by the Ballerina Pearl Co.

We also offer hearty congratulations to the winners of the 2015 Dr. Edward J. Gübelin Most Valuable Article Award. We're delighted with the fantastic response to our reader ballot, which showed a significant increase in participation over last year—a big "thank you" to everyone who voted. Please see the results on page 37. Also, don't forget to take this year's *G&G* Challenge, our annual multiple-choice quiz, on pages 66 and 67.

Please enjoy the Spring issue!

Duncan Pay | Editor-in-Chief | dpay@gia.edu

AN INTRODUCTION TO PHOTOLUMINESCENCE SPECTROSCOPY FOR DIAMOND AND ITS APPLICATIONS IN GEMOLOGY

Sally Eaton-Magaña and Christopher M. Breeding

Photoluminescence (PL) spectroscopy is frequently mentioned in the gemological literature, but its relevance to the wider trade audience is rarely discussed. Due to the possibility of an undisclosed treatment or a synthetic origin, all type II diamonds (both colorless and fancy-color) and colorless type IaB diamonds submitted to gemological laboratories should ideally be tested using PL spectroscopy. Although the proportion of samples that require this testing is small, the failure to properly identify treated and synthetic diamonds could destabilize the diamond industry. This article seeks to clarify the underlying physics and methodology of this important tool for gemologists.

Photoluminescence (PL) spectroscopy, as applied in gemology, is a nondestructive analytical technique in which a material is illuminated with light, usually from a laser, and the resulting luminescence is recorded as a plot of emitted light intensity versus wavelength. In the last decade, PL has become an essential tool used by major gemological laboratories to separate treated and synthetic diamonds from their natural counterparts (e.g., Breeding et al., 2010; Lim et al., 2010). Atomic-scale features (often termed *optical centers, optical defects,* or simply *defects*) occur within the diamond structure; examples include carbon, nitrogen, boron, and vacant carbon-atom locations in the lattice (i.e., vacancies). The configuration of these defects varies with the growth conditions and subsequent geological or treatment history. PL provides a very sensitive tool for detecting deviations in atomic configurations and defects even at concentrations of less than ten in a billion carbon atoms (Wotherspoon et al., 2003). Today, nearly all type II colorless to near-colorless and fancy-color diamonds require PL analysis for de-

finitive characterization as natural, treated, or synthetic. Type IIa pink and type IIb blue natural diamonds, for instance, can be extremely valuable, commanding prices upward of $1 million per carat. The natural origin of such diamonds is often verified principally through features in their PL spectra (figure 1).

Treated and synthetic diamonds may each display distinctive visual features—graphitized inclusions, metallic inclusions, facet-related color zoning, graining patterns, or altered surfaces—that are visible under magnification. But these characteristics are not always present, or necessarily specific to treated, synthetic, or natural stones. Gemological laboratories often rely on absorption and luminescence spectroscopic techniques to conclusively identify diamonds submitted for examination (e.g., Collins et al., 2000; Collins, 2003; Shigley and Breeding, 2013). High-pressure, high-temperature (HPHT) treatment of diamonds for color enhancement has become increasingly widespread in the trade over the past several years; more recently this process has been combined with irradiation and annealing to produce an even wider range of desirable diamond colors. The combination of multiple treatments and the constant evolution of treatment and synthesis technologies present significant challenges for these laboratories (Schmetzer, 2010; Lim et al., 2010).

Figure 1. Diamonds can show a wide range of hues and fluorescence colors. GIA regularly uses photoluminescence spectroscopy to confirm the natural origin of such diamonds. PL is a sensitive technique that allows one to characterize the atomic-level lattice defects that act as a fingerprint of the growth and possible treatment history of diamonds; this method is similar in principle to observed fluorescence. Here, a portion of the Aurora Butterfly of Peace (left) is shown as a fluorescence image illuminated by a long-wave UV lamp (right). Photos by Robert Weldon.

A diamond's origin—whether it was mined from the earth or created in a lab—and subsequent treatment history can be a major factor in its value. PL analysis is a remarkable translator of each diamond's story; its extremely sensitive detection of trace concentrations of defects is unmatched by other non-destructive characterization techniques. Therefore, PL analysis has become an integral part of the diamond grading process. While the number of diamonds that require PL testing is relatively small—approximately 2% of all diamonds are type II—these are often the largest or most highly valued stones.

Despite PL's importance for diamond and other gemstone analysis, it is not widely available outside of gemological laboratories due to the relatively high costs of the equipment, maintenance, training, and specialized sample requirements. The necessary microscopes, lasers, and spectrometers that make up most PL systems together cost several hundred thousand dollars. Smaller desktop and portable units using a charge-coupled device (CCD) provide some of the important functionality of more expensive systems, but they are generally lacking in other areas, such as resolution (their ability to distinguish individual peaks). The PL features of defects in diamond also tend to be sharper, and thus appear more intense, at very cold temperatures. Consequently, spectra are usually collected with the diamond cooled to liquid nitrogen temperature (–196°C). These requirements, along with the inherent danger of high-energy light sources such as lasers, introduce important safety considerations as well.

Most importantly, a diamond's formation and color origin can be confirmed only when data are evaluated against information obtained from known natural, treated, and synthetic diamonds, so a database of such samples is vital. PL spectra also function in concert with other spectroscopic analyses (e.g., infrared and UV-Vis-NIR absorption), fluorescence imaging (namely the DiamondView), and gemological observations. Due to complex treatments and the evolution of synthetic diamond growth techniques, the accurate assessment of color origin is best left to fully equipped gemological laboratories. Nevertheless, members of the gem industry should have some understanding of the analytical techniques on which many color origin determinations are based.

Gemological journals such as this one regularly present PL spectra within scientific studies, but the underlying theory and data collection procedures are perhaps not well understood by the typical gemologist who relies on these articles for vital knowledge. This article is not intended as a comprehensive review of PL or the features scientists use to make an origin determination. Instead it seeks to explain, in somewhat simplified terms, what PL spectroscopy is; how it relates to other types of luminescence measurements such as fluorescence, phosphorescence, and Raman spectroscopy; and why it is important to gemologists. PL is most commonly used with diamond analysis, but it has some important applications for other gemstones as well, which are briefly mentioned at the end of this article and in table 1.

TABLE 1. Summary of luminescence techniques used in gemology.

Type	Energy source	General features observed	Applications in gemology	Advantages	Disadvantages
Photoluminescence	Laser	Sharp diagnostic peaks in spectra, sometimes with underlying broad bands. A spectral technique.	Determination if diamond is treated and if it is of natural or synthetic origin. Evaluation of the color origin of coral and separation of natural, synthetic, or heat-treated spinel.	Very sensitive measurements for defects at low concentrations (ppb level)	Diamond must be very cold (i.e., in liquid nitrogen) for reliable collection of sharp peaks. Equipment can be prohibitively expensive.
Fluorescence (long-wave and short-wave)	UV light source (mercury lamp, deuterium lamp, UV LED, etc.)	Broad spectral bands, or observation of color. Both a spectral and an imaging technique.	Color observation in diamond can provide a distinguishing characteristic (as on a laboratory grading report). Wide range of uses for other gemstone identification and treatment determinations.	Simple, inexpensive technique	Fluorescence is not diagnostic of diamond color origin.
Deep UV fluorescence (DiamondView) (Welbourn et al., 1996)	High-energy, high-intensity UV light source	An imaging technique	Shows diamond growth features in terms of spatial patterns and variations in fluorescence color	Determination if diamond is natural, synthetic, or (in very rare cases) treated	Low throughput. Generally not diagnostic for natural vs. treated diamonds.
Phosphorescence	UV light source (deuterium lamp, UV LED, etc.)	Both a spectral and an imaging technique	Can help identify colorless HPHT synthetics and synthetic IIb diamonds, which do not phosphoresce at 660 nm (Eaton-Magaña et al., 2008, Eaton-Magaña and Lu, 2011). Can also aid in the identification of natural opal.	Simple, inexpensive technique	Limited usefulness in diamond
Cathodoluminescence	Electrons (from an electron gun)	Both a spectral and an imaging technique	Provides information comparable to PL spectra and DiamondView imaging	Determination if diamond is natural, treated (in rare cases), or synthetic	Usefulness limited by the requirements of a vacuum chamber and an electron gun
X-ray fluorescence	X-rays	Both a spectral (as energy-dispersive XRF) and an imaging technique	EDXRF produces spectra that provide chemical composition information. It can help determine country of origin for certain colored stones and glass filling treatment in diamonds. X-ray fluorescence imaging is useful for sorting diamond from non-diamond material and distinguishing origin of pearls.	EDXRF is non-destructive and has variable sampling areas. XRF imaging can help reveal the distribution pattern of chemical elements in a material.	EDXRF is less sensitive than other analytical methods, and it cannot effectively detect chemical elements lighter than sodium.
Thermoluminescence	Laser excitation/subsequent heating	At present, mostly for novel observations of luminescence	Mostly historical usage in type IIb diamonds (e.g., Halperin and Chen, 1966)	At present, no major advantages for testing diamonds	
Electroluminescence	Electrical current	At present, mostly for novel observations of luminescence	Occasionally seen in type IIb diamonds (e.g., Inns and Breeding, 2007)	At present, no major advantages for testing diamonds	

Therefore, most of the technique information is also applicable for gems other than diamond (although they should not be cooled to liquid nitrogen temperatures). There are several excellent reviews of diamond spectroscopy that describe the various defects that occur in natural, synthetic, and treated diamonds (Collins, 2001, 2003; Zaitsev, 2003; Dischler, 2012; Dobrinets et al., 2013; Shigley and Breeding, 2013). We encourage the reader to consult these references for more information.

SPECTROSCOPY AND LUMINESCENCE THEORY

Spectroscopy can be defined as the branch of science concerned with the investigation and measurement of spectra produced when matter interacts with or emits electromagnetic radiation. These interactions are very useful for the analytical testing of gemstones because the energy of visible light or other types of radiation can closely match the energy difference of a wide variety of chemical bonds in minerals. The energy of the chemical bonds within diamond and many other gemstones is relatively constant. Over the past century, considerable research work has been done to identify the atomic configuration of spectral features. Consequently, spectroscopy is an accurate identification tool for a wide variety of gemstones. The high sensitivity of PL in particular allows for detection of many spectral peaks that are impossible to measure by other techniques, thus revealing important details about a stone's history, such as growth or treatment.

Luminescence, the emission of visible light, occurs when an energy source (laser, UV lamp, etc.) knocks an electron out of its stable "ground" state and elevates it to an "excited" state. As the electron returns to its normal ground state, energy is released, much of it in the form of visible light. In almost all cases, the emitted light is of a lower energy in the electromagnetic spectrum than the original light from the energy source. Since wavelength and energy are inversely proportional, a lower energy always translates to a higher wavelength. Therefore, PL spectra always encompass a wavelength range that is higher than the wavelength of the excitation source. The relationship between energy (in eV), wavelength (in nm), and wavenumber (in cm^{-1}) is given by equation 1:

$$E\ (eV) = \frac{hc}{\lambda} \approx \frac{1240}{\lambda(nm)} \approx \frac{1240\nu(cm^{-1})}{10^7}\ [1]$$

where E is the energy in units of eV, or electron volts, λ is the wavelength measured in nanometers (nm), and ν is the wavenumber, which has units of cm^{-1} and is the reciprocal of wavelength. The 1240 value derives from physical constants and conversion factors: h is Planck's constant (6.6261×10^{-34} joule-seconds), and c is the speed of light (2.9979×10^8 meters/second); 1 eV converts to 1.6022×10^{-19} joules, and 1 nanometer converts to 1×10^{-9} m. Figure 2 shows the ranges of values for wavelength (in nm), wavenumber (in cm^{-1}), and energy (in eV) from the ultraviolet through the infrared portion of the electromagnetic spectrum.
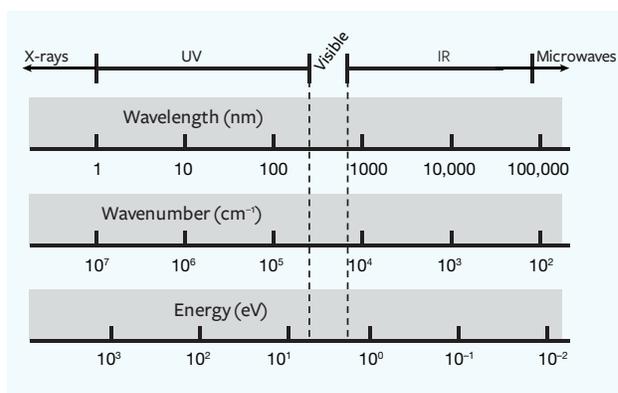
Figure 2. The wavelength, frequency (in wavenumber), and energy divisions of the electromagnetic spectrum show that frequency and energy are proportional while wavelength is inversely proportional to them. Adapted from Sauer et al. (2010).

With luminescence, there can be a variety of energy sources (UV lamp, laser, electron gun, X-ray), different pathways for the electron to return to the ground state (direct, or delayed by one or more intermediate states), and various conditions that affect the rate of the process (temperature, the presence of other defects, etc.). Figure 3 shows a chart of several types of luminescence and how they relate.

In Brief

- Photoluminescence (PL) spectroscopy is one of the most important tools used by gem laboratories to detect treatment and distinguish between natural or synthetic origin of diamonds.

- While fluorescence and PL spectroscopy are based on many of the same principles, the more sophisticated equipment and data collection procedures allow the detection of defects down to the parts per billion (ppb) level.

- The gemological applications of PL spectroscopy will continue to expand in the coming years.

Within gemology, there are several measurement techniques that, as now practiced, differ from their given scientific definitions: phosphorescence, fluorescence, and photoluminescence, for example. In these cases, both the scientific definition and the de facto practice within gemology are provided. Table 1 summarizes several types of luminescence, some of which are important in gemology.
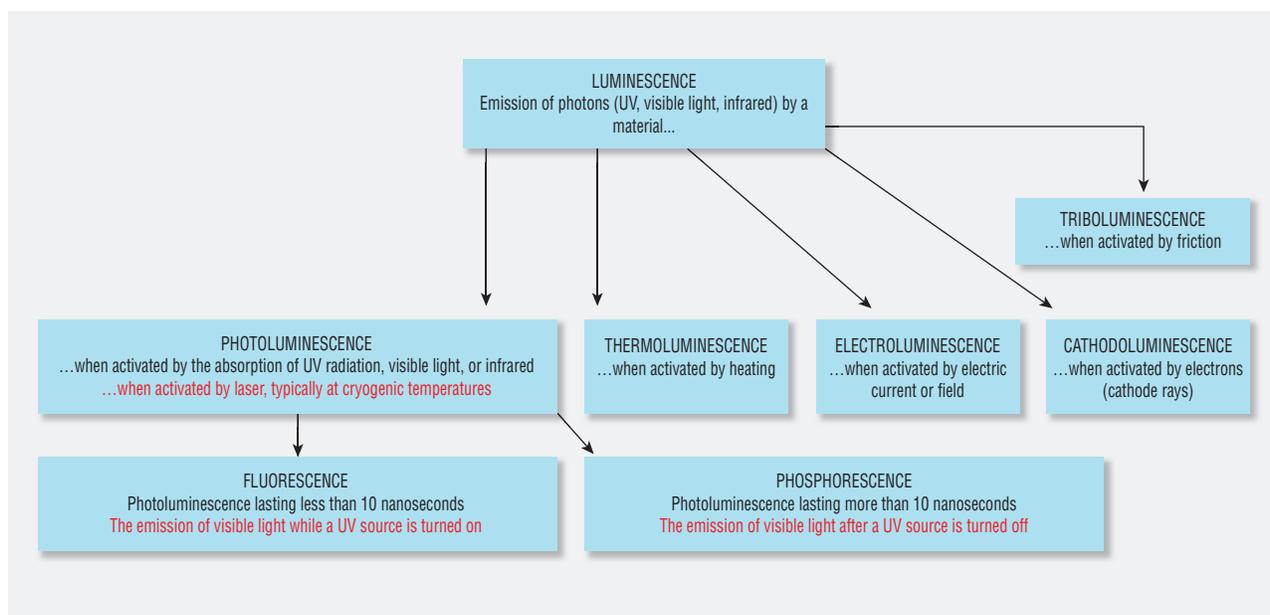
Figure 3. This chart shows the interrelationships between various forms of luminescence, particularly photoluminescence, which includes fluorescence and phosphorescence. A few other types of luminescence relevant to gemology are shown as well (note that other types of luminescence such as chemiluminescence and bioluminescence are not included in this illustration). When the scientific definition (in black) is distinctly different from the gemological usage (in red), both definitions are shown for clarity.

Optically Active Defects. Gemological laboratories rely on nondestructive analytical techniques for diamond that are based mainly on optical methods such as absorption and PL spectroscopy. Only defects that emit light (i.e., optically active defects) can be detected by PL, and these detections are further constrained by operating conditions such as temperature and excitation laser wavelength. These constraints often limit our knowledge about the full range of impurities and defects present in gemstones, forcing us to focus any assessments on information obtained principally from optically active defects.

Fortunately, most impurities in diamond are optically active in some manner. For example, a pair of PL peaks at 736.6 and 736.9 nm (the SiV^- doublet) indicates the presence of silicon impurities in diamond. These impurities are very rarely seen in natural diamond but typically occur in CVD synthetic diamond and thus assist in their identification (Breeding and Wang, 2008). Many well-known defects in diamond are various combinations of nitrogen impurities with vacancies in the lattice (such as N3, H2, H3, H4, and NV centers) and have been characterized extensively over the past decade (see recommended references in the introduction). Several other PL peaks occur in natural diamond and have been correlated with diamond color, type, or geographic origin, but the composition

of the associated lattice defects has not been conclusively identified by scientists. Eaton-Magaña and Lu (2011), among others, correlated several PL peaks, such as those at 648.2 nm and 776.4 nm, with gray to blue color and boron concentration in phosphorescing type IIb diamonds. Later researchers ascribed the 648.2 nm defect to a boron-interstitial complex (Green, 2013), while the configuration of the 776.4 nm peak remains undefined.

To understand how luminescence techniques like PL reveal useful information about diamond formation and color origin, we must first discuss the anatomy of a carbon atom and how it interacts with energy to produce luminescence. Figure 4 provides a simplified model for an isolated carbon atom within the diamond lattice, showing the nucleus and electron orbits, including the "excited" state. It is important to remember that in solids, atoms are not isolated and do interact with surrounding atoms. These interactions broaden the allowed energy states into bands (valence and conduction, at the center of the figure). The energy region between these bands, where certain energy states associated with a perfect diamond lattice are forbidden, is known as the band gap. In figure 4, the band gap is expanded. The excitation energies provided by a range of fluorescence lamps and commonly used

lasers are shown, as well as the states of typical diamond defects that fall within the band gap. In spectroscopy, particularly with sensitive techniques like PL, such atomic-level defects are quite helpful in identifying a diamond's origin and subsequent treatment. These optical centers function as storytellers of a diamond's history.

In addition, the excitation source generally has an energy equal to or greater than the emission energy; in other words, a 633 nm laser (2.0 eV) will not activate the N3 center in diamond (3.0 eV; 415 nm). In practice, certain defects are also more efficiently excited by particular laser wavelengths. For example, most PL peaks in the 900–1000 nm range are more intense when activated by a 785 or 830 nm laser than by a 325 nm laser. Hence, PL spectra are typically acquired using lasers of various wavelengths.

Photons and Phonons: ZPLs and Sidebands. A *photon* is a single (quantum) particle of visible light and other forms of electromagnetic radiation, while a *phonon* is a quantum particle of directional vibration for a group of atoms (such as a luminescence-exciting defect) within the crystal lattice. The zero-phonon line (ZPL) is the wavelength at which a photon is emitted between energy levels when no phonons— that is, no vibrations—are involved.

The photon energy of the emitted light from an optical center corresponds to the energy released when an excited electron returns to its ground state; there is also a contribution of internal energy loss due to the lattice vibration. The optical center is usually an imperfection of the crystal lattice—from either the presence of an impurity atom or an interruption in the lattice structure. This distortion modifies the vibration characteristics of the atoms in the vicinity of the optical center within the host material. Therefore, many optical defects show not only an electronic transition but also this vibronic contribution, known as a "phonon sideband." Depending on the strength of the

Figure 4. At left is a simplified model for a carbon atom showing the nucleus and electron orbits, including an "excited" state (dashed line). Carbon atoms within the diamond lattice are also affected by adjacent carbon atoms (center) and represented by the band gap model for an electrically insulating material such as diamond. In insulators, the electrons are located within the valence band and separated by a large energy gap from the conduction band. At right, the difference between the valence band (populated by electrons) and the conduction band, known as the band gap, is expanded. When studying diamond, scientists use energies less than its band gap of 5.5 eV (> ~225 nm) to excite internal defects rather than the diamond itself. Only the defects within this range can be studied using PL.
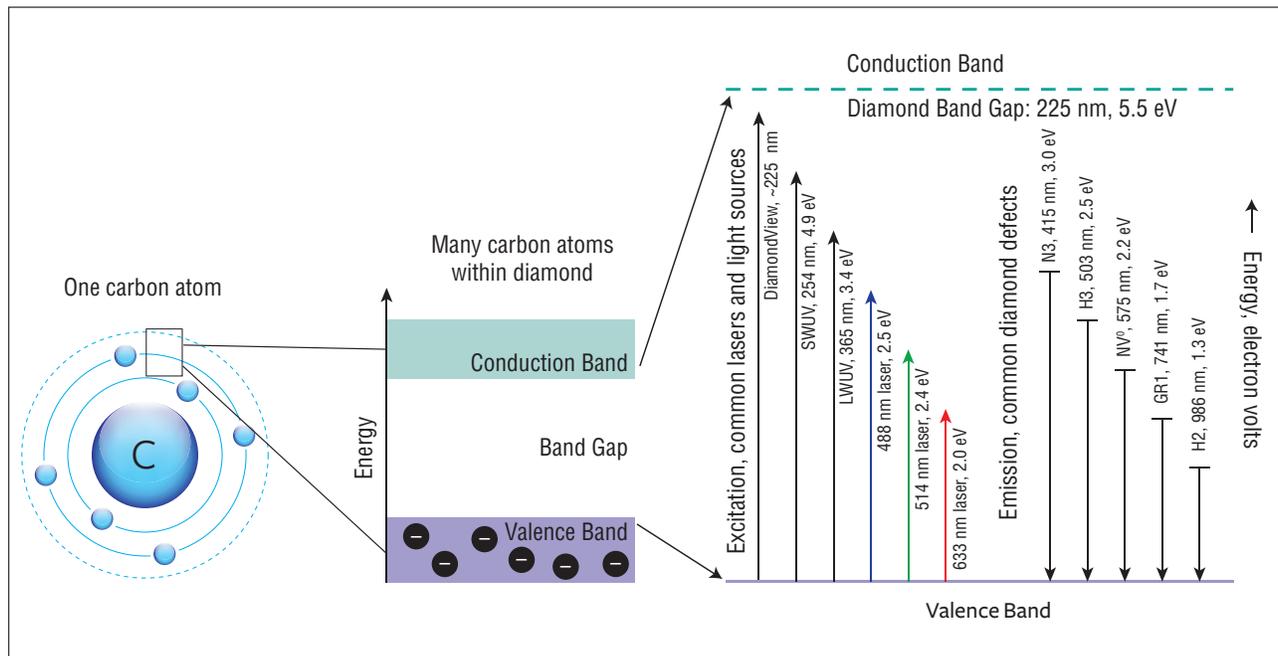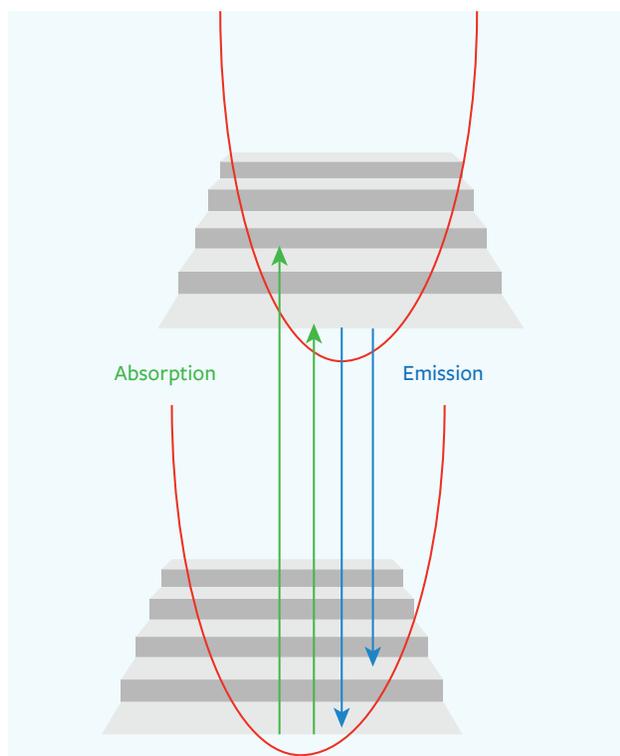
Figure 5. This illustration of the stairwell analogy is a slight modification of the standard Franck-Condon principle energy diagram showing electron transitions with phonon coupling. Both absorption and emission are shown. The red parabolas indicate the potential wells for the energies.

vibronic contribution, the purely electronic transition (i.e., the zero-phonon line) sometimes can only be detected at cryogenic temperatures.

The energy levels of the valence band and the conduction band shown in figure 4 are simplified representations. Contained within these electronic energy levels are subdivisions based on vibrational energy levels, which are determined by the way the defects can vibrate within the diamond lattice.

One might envision, in very simplified terms, that the ground state is the ground floor of a building and the excited state is the first-floor landing (figure 5). The vibrational levels would be steps on a staircase between the two floors. In PL spectroscopy, the ZPL can be seen as a direct jump from the first-floor landing to the ground floor; as its name implies, a ZPL generally does not involve phonons (i.e., vibration).

In absorption, the electron resting on the ground floor can be excited up to the first-floor landing or to the first or second step above the first-floor landing. In fluorescence, an electron might be sitting on the

first-floor landing and then jump down to either the ground floor or the first or second step above the ground floor. This variability in the starting and ending staircase steps spreads out the energy released by the resulting photons, creating both the broad fluorescence bands observed at room temperature and the sidebands of the ZPLs usually observed at liquid nitrogen temperatures (figure 6).

The ZPL is a sharp peak often referred to in PL spectra precisely because its wavelength is exact, specific to a certain defect, and unambiguous; however, its underlying mechanism may not be understood by scientists who use PL spectra daily. The width of the ZPL is determined by the lifetime of the excited state (Sauer et al., 2010), though in practice it will be broadened by strains in the crystal.

For a diamond immersed and cooled in liquid nitrogen (77 K, –196°C; figure 6), most of the electrons reside at the ground state. When activated, they will create emission at the ZPL wavelength. As temperature is increased, the electronic transitions are dispersed over broader ranges so that the resulting fluorescence is distributed across a wider wavelength range. At room temperature, the ZPL all but disappears in most cases and only the sideband remains. Usually the distribution of intensity between the ZPL and the phonon side band is strongly dependent on temperature. At room temperature, there is enough thermal energy to excite many phonons, and the probability of zero-phonon transition is much lower (again, see figure 6).

Comparison with Fluorescence and Phosphorescence. Occasionally, definitions of terms within a scientific context are different from, and perhaps at odds with, their common usage. Within the field of gemology, the terms *fluorescence*, *phosphorescence*, and *photoluminescence* have evolved from their general scientific definitions and taken on different meanings. Fluorescence and PL are scientifically regarded as similar processes in which fluorescence is a subset of PL with lifetimes less than 10 nanoseconds (again, see figure 3). Gemology draws a different distinction between these two terms. Both fluorescence and PL detect the same features within gemstones, but the experimental output is vastly different. In gemology, fluorescence has traditionally been measured at room temperature, typically with a broadband or multi-band lamp (although LED lamps have been a significant improvement; Luo and Breeding, 2013). The eye or a low-resolution spectrometer functions as the detector. Conversely, PL
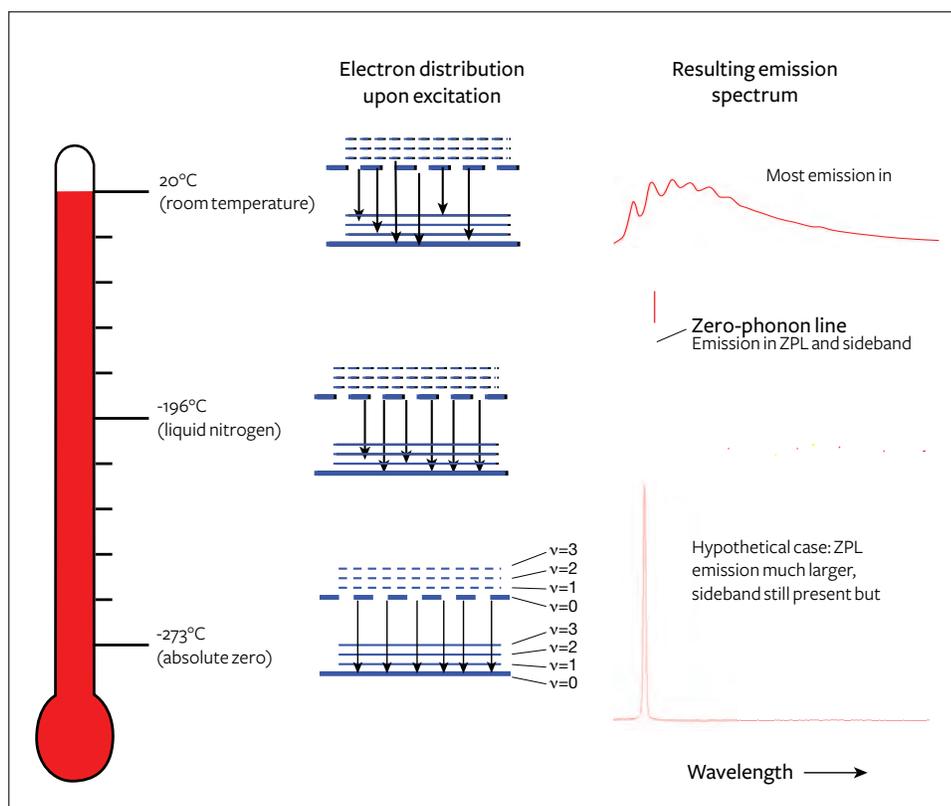
Figure 6. In the hypothetical case of absolute zero temperature, electrons reside at the lowest energy level of the ground state (solid lines), where phonons (vibrations, or ν) equal zero. Then they are excited to the ν = 0 level of the "excited" state (dashed lines). This theoretically results in a nearly 100% ZPL emission. As temperature increases to room temperature, electrons are in higher vibrational energy states (where ν = 1, 2, 3, etc.), creating an ever-increasing distribution of luminescence pathways (black arrows). The resulting emission is spread across a wide wavelength range as a sideband with little to no ZPL emission.

spectra of diamond are collected at liquid nitrogen temperature using laser excitation and a high-resolution spectrometer (figure 7). Figure 8 shows how temperature, excitation source, and spectrometer resolution affect the quality of the emission spectra collected from both traditional fluorescence measurement and PL analysis.

A laser used for PL spectroscopy offers several advantages over both standard UV lamps and tunable spectrofluorometer instruments in detecting fluorescence. Many traditional mercury-based long- and short-wave UV lamps excite multiple different wavelengths simultaneously (Williams, 2007; Luo and Breeding, 2013), which can create variability in the observed fluorescence color (Eaton-Magaña et al., 2007). Spectrofluorometers are able to filter a single excitation wavelength to a narrow range, but the resulting intensity is reduced because of the lower illumination power. The use of lasers addresses both problems by providing intense illumination over a very narrow wavelength range. In combination with sample cooling, laser excitation often reveals smaller PL peaks that might not be visible at room temperature or with other excitation sources (e.g., figure 9).

Physicists define fluorescence as luminescence with a decay time of 10 nanoseconds or less, while phosphorescence is delayed luminescence with a decay time greater than approximately 10 nanoseconds (again, see figure 3). Sophisticated analytical tools can measure these very short decay times (their potential usefulness will be discussed below). Within gemology, fluorescence is colloquially defined as the emission from the gemstone when a UV source is turned on, and phosphorescence is the observed emission after the UV source is turned off. Practically speaking, gemologists can visually detect phosphorescence only when the decay time is about one second or longer. A few natural diamonds, such as chameleons and type IIb stones, show visible phosphorescence (e.g., Hainschwang et al., 2005; Eaton-Magaña and Lu, 2011), as do some HPHT synthetics (Shigley et al., 1997) and HPHT-treated CVD synthetics (Wang et al., 2012). Beyond that, the usefulness of phosphorescence is somewhat limited.

Fluorescence and phosphorescence techniques both offer simple, inexpensive methods to create additional identifiers of an individual gem (i.e., to better distinguish similar-looking diamonds). For additional information on specific fluorescence and phosphorescence reactions, see Shigley and Breeding (2013) and Luo and Breeding (2013).

Figure 7. The commercial Renishaw inVia Raman microspectrometer is equipped with several lasers, such as the 514 nm laser shown here. In normal operation (with the shields in place and the door closed), the system safely operates as a Class I laser. This photo demonstrates the internal optics and the laser beam's path as it travels from the laser to the microscope, back through the microscope (along with emission from the diamond at longer wavelengths), and then to the spectrometer. Photo by Kevin Schumacher.

Sensitivity of PL. Many nitrogen-containing defects, such as the neutral and negatively charged NV centers (ZPLs at 575 and 637 nm, respectively; Zaitsev, 2003), are routinely observed using PL in type II diamonds, which by definition contain negligible nitrogen impurities measurable by infrared absorption. As mentioned earlier, a major advantage of PL analysis is its high sensitivity to weak emission of light. Even in diamonds with nitrogen impurity concentrations below the 1–5 parts per million detection limits for infrared absorption instruments (i.e., type II diamonds), PL can detect NV concentrations of 10 ppb or less (Wotherspoon et al., 2003). Therefore, the type II designation does not indicate "no nitrogen whatsoever," but that the diamond has potentially very low quantities of this impurity. Nitrogen-bearing defects (such as H2, H3, H4, NV centers, and N3) are typically the dominant features in PL spectra of type IIa diamonds. However, nitrogen A and B aggregates in type Ia diamonds do not have characteristic emissions identifiable using PL, and their presence is best detected with FTIR absorption spectroscopy (Zaitsev, 2003). In practice, FTIR is performed first on a diamond to identify the diamond type. This diamond type determination allows gemologists to filter out type II diamonds, which are potentially treated or synthetic, from type Ia, which represent the vast majority of natural diamonds (Breeding and Shigley, 2009).

USE OF PL IN GEMOLOGY

PL came to widespread prominence in the diamond industry in 1999, when General Electric (GE) announced an HPHT treatment method for decolorizing type II brown diamonds ("Pegasus Overseas…," 1999; Shigley et al., 1999). Standard gemological testing could not identify the HPHT-treated diamonds, but the sensitivity of PL allowed the separation of these goods from their natural-color counterparts. Since then, the evolution of treatments and synthesis techniques has made the use of these complex analytical identification methods and instruments, such as mapping spectrometers and automated gem testing, more widespread in major gemological laboratories.

HPHT-Treated Diamonds. After the initial industry panic that followed GE's revelation, extensive research showed that PL spectroscopy of diamond at

LUMINESCENCE OF H3 CENTER IN YELLOW-GREEN DIAMONDS

A
Room temperature
Filtered broadband UV source (365 nm)
Low-resolution spectrometer
30-second collection time
Ocean Optics USB2000 spectrometer

B
Room temperature
365 nm LED
High-resolution spectrometer
1-second collection time
Ocean Optics HR2000 spectrometer

C
H3 ZPL
(503.2 nm)
Room temperature
488 nm laser; 0.5% power
High-resolution Renishaw inVia spectrometer

D
H3 ZPL (503.2 nm)
Liquid nitrogen temperature
488 nm laser; 0.05% power
High-resolution Renishaw inVia spectrometer

Figure 8. Yellow-green diamonds often show a visible H3 green fluorescence that can contribute to the bodycolor. These four spectra, collected on one diamond, show the progression in data quality as experimental parameters such as excitation source, spectrometer, and collection temperature are improved. A: The ZPL of the H3 center is not visible and only the sideband is collected, making it difficult to verify whether H3 is the defect responsible for the fluorescence in this diamond. B: A broad, somewhat indistinct ZPL is seen, along with some of the finer sideband structure. C: A definite ZPL at 503.2 nm is observed in the laser-activated, room-temperature measurement, but the spectrum is overwhelmed by the sideband, which could also obscure other peaks within this wavelength range. D: The ZPL is dominant, clearly identifying the cause of fluorescence. Additionally, these spectrometers have very different spectral resolutions, leading to apparent differences in ZPL peak width. Nevertheless, it is the relative prominence of H3 that is important here.

liquid nitrogen temperatures was the most effective method for identifying HPHT treatment (Fisher and Spits, 2000). Natural type IIa brown diamonds are typically the starting material for the decolorizing HPHT treatment process. The brown color of the starting material is thought to be caused by clusters of vacant atom positions (i.e., vacancies) along planes of carbon atoms in the diamond structure that were misaligned by natural plastic deformation processes (Hounsome et al., 2006). When the vacancy clusters are broken up at high temperatures, the brown color is removed, leaving a colorless or near-colorless diamond, but also telltale evidence of the treatment process that is detectable by PL.

Natural diamond formation takes millions of years. Regardless of a treatment's sophistication, there is usually detectable evidence of the much shorter process (minutes to hours in the case of HPHT treatment). The elapsed time of natural diamond formation simply cannot be replicated in a laboratory. Most of the PL features that indicate treatment are not discussed publicly, out of concern that treaters will modify their techniques in an attempt to deceive laboratories. A few have been disclosed, however. It has been widely reported that after HPHT treatment, the intensity of the 637 nm PL peak (NV$^-$) is stronger than its 575 nm (NV^0) counterpart when excited by a 514 nm laser. For most natural type II diamonds, this ratio is inverted. At the treatment conditions required to remove brown col-

PL SPECTRA

Figure 9. The GR1 peak intensity, position, and width vary significantly with diamond sample temperature during PL measurement. This behavior is true of all ZPLs to some extent. In this study, data was collected with 514 nm excitation and a Linkam Examina Dynamics System to control temperature during analysis.

oration, HPHT processing commonly breaks down nitrogen aggregates to create single substitutional nitrogen impurities, which behave as electron donors. Charge transfer of the newly available electrons causes the PL intensity of the 637 nm defect (the negatively charged NV^- center) to increase relative to the 575 nm center (the neutral NV^0 center) (Chalain et al., 2000). Although PL was initially used to determine HPHT treatment in colorless diamonds, it is now often used to detect diamond formation and color origin for both colorless and colored diamonds (Wang et al., 2012).

Combination-Treated Diamonds. In the years since HPHT treatment was first introduced, diamonds have been subjected to HPHT annealing in combination with earlier treatments such as irradiation and lower-temperature annealing; this has made the identification process even more complex. Multi-treatment processes may be used to create certain attractive colors such as pink, but they can also be used to conceal previous treatments and make a diamond appear more spectroscopically "natural." Regardless, absorption and PL spectral features, in conjunction

with gemological properties, are required to identify many treated diamonds. It has become increasingly important to investigate the presence and absence of a combination of PL features, in addition to data from other spectroscopic and gemological techniques, rather than simply rely on analysis of a single feature or a single technique.

Synthetic Diamonds. Over the past several years, gem-quality synthetic diamonds grown either by chemical vapor deposition (CVD) or HPHT methods have become increasingly available in the market, but they still comprise a very small percentage of diamonds analyzed by gemological laboratories. CVD synthetic diamonds have different inclusions and growth morphology from those observed in HPHT-grown synthetics. Rapid advances in CVD synthesis techniques in the last decade have complicated the gemological separation of these materials. High-quality PL spectroscopy has proven essential to their proper identification (e.g., Wang et al., 2007, 2012; Song et al., 2012). PL spectroscopy can discern a CVD origin and determine if any post-growth treatments have been applied.

Other Gem Materials. Although diamonds are the focus of this article, PL spectroscopy can be applied to other gem materials. Raman analysis has been a reliable gemstone identification tool for decades, and its instrumentation often proves quite useful in the collection of PL spectra (see box A for a description of the differences between these techniques). For example, the separation of natural from synthetic spinel can be quite difficult in high-clarity gemstones. Yet PL analysis of stones with chromium fluorescence bands can easily distinguish synthetic spinel (Kitawaki and Okano, 2006). Similar features provide evidence of heat treatment in natural spinel to enhance their color (Saeseaw et al., 2009; Kondo et al., 2010). Bidny et al. (2010) showed that photoluminescence excitation (PLE) spectroscopy, a variation on standard PL, can also separate natural from flux-grown synthetic rubies. While PL uses a single laser and scans the emission wavelengths, PLE holds the emission wavelength fixed and scans the excitation range. For example, excitation spectra for the chromium peaks at 692/694 nm showed an additional band at approximately 290 nm in flux synthetic rubies only (Bidny et al., 2010).

PL spectroscopy has also proven useful for some organic gemstones. Combined with Raman spectroscopy, it can separate natural red coral from dyed

BOX A: RAMAN ANALYSIS VERSUS PHOTOLUMINESCENCE

Raman and PL spectra are collected with the same instrumentation at the same time, and Raman peaks even appear in PL spectra. So what is the difference?

Luminescence peaks are emitted at a constant energy (or wavelength) from a material. For example, the GR1, a defect that imparts green color in diamond by creating a transmission window within the green portion of the visible spectrum, will always show absorption and emission at 741.2 nm (the ZPL), whether the excitation source is sunlight, a UV lamp, a 514 nm laser, or a 633 nm laser. The absorption band and luminescence band will not shift to a different wavelength simply because a different light source is used.

Raman peaks, however, have a constant energy *difference* from their excitation source. Raman scattering was discovered in 1928 by Sir C.V. Raman (figure A-1) and his colleague K.S. Krishnan, and independently discovered by a pair of Soviet scientists. Raman and Krishnan observed, using filtered sunlight, that a miniscule amount of light changed frequency (and therefore wavelength) after impinging on a material. The

Figure A-1. Sir Chandrasekhara Venkata Raman was an Indian physicist and among the discoverers of the Raman effect. He won the Nobel Prize for Physics in 1930 for this work.

light interacts with the molecular vibrations or phonons within the material; this creates a change in frequency when the absorbed light is re-emitted by the material. Raman spectroscopy measures the energy shift caused by these vibrational (and sometimes rotational) energy levels.

Although only one in 100 million photons is shifted by this vibrational energy, the Raman peak is generally the dominant feature in most type IIa diamond PL spectra. This should indicate the extremely low intensity of luminescence peaks in type IIa diamonds, and the highly sensitive equipment needed to accurately measure PL features.

Unlike PL peaks with fixed energies and wavelengths (commonly expressed in nanometers in the gemological literature), Raman peak values are usually not reported in units of energy (eV), but as frequencies, or "wavenumbers" with units of cm^{-1}, that are proportional to energy and inversely proportional to wavelength (see equation 1). In Raman spectra, the reported values are *relative* to the excitation source and are considered Raman shift values. These should not be confused with wavenumbers (cm^{-1}) shown in infrared absorption spectra, which are *absolute* energy values.

The following conversion calculates the wavelength position of a Raman peak in a PL spectrum based on the wavelength of the excitation laser.

$$\frac{Raman\ line}{[nm]} = \frac{1}{\dfrac{1}{Laser\ excitation\ [nm]} - \dfrac{Raman\ line\ [cm^{-1}]}{10^7\ [nm \cdot cm^{-1}]}} \quad [2]$$

For diamond with a characteristic Raman emission at 1332 cm^{-1}, the same peak is located at 522 nm with 488 nm excitation and at 552 nm with 514 nm excitation. Figure A-2 demonstrates how the Raman line shifts to different wavelengths depending on the excitation laser wavelength. The GR1, a luminescence peak, is fixed at 741.2 nm regardless of laser excitation. Figure A-2 also shows a "second-order" Raman line often seen with 514 nm excitation. This feature occurs at twice the Raman shift of the 1332 cm^{-1} peak, or 2664 cm^{-1}, which converts to 596 nm.

Figure A-2. PL spectra were collected on the same greenish diamond using three different lasers (488, 514, and 633 nm) at liquid nitrogen temperature. Each laser shows a different location for the diamond Raman line based on the excitation wavelength. For all three lasers, the energy difference between the excitation wavelength and the Raman line is constant— 1332 cm^{-1}, or 0.165 eV. Each spectrum shows the luminescence feature GR1 and its consistent activation at 741.2 nm, regardless of the excitation source. While the Raman line will shift within the visible range based on the excitation source, the luminescence features will remain at a fixed wavelength.
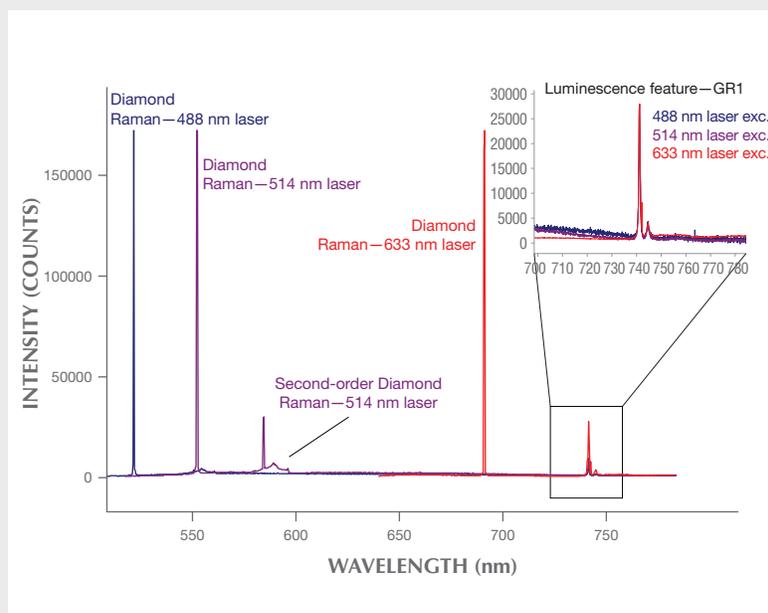
coral (Smith et al., 2007). Features in PL spectra are also able to distinguish natural-color cultured pearls from artificially colored ones (Wang et al., 2006; Karampelas et al., 2011). When combined with gemological techniques, PL shows features that distinguish tortoiseshell from some of its imitations (Hainschwang and Leggio, 2006).

Unfortunately, most gemstones cannot be cooled to liquid nitrogen temperatures to optimize the results from PL spectroscopy. Diamonds have extremely high thermal conductivity and a low thermal expansion coefficient, which allows them to withstand low temperatures. Other gems are exposed to a much higher risk of fracture if cooled. For example, the thermal conductivity of corundum is at least 65 times lower than that of diamond (Read, 2008), and its coefficient of thermal expansion is five times greater (Fiquet et al., 1999).

FUTURE

In the last decade, the use of PL to determine diamond origin has become commonplace in gemological research laboratories, while PL analysis itself has become more complex. When HPHT treatment was first introduced, a visual evaluation of the presence or absence of particular PL peaks from a single laser, analyzing two or three wavelengths at most, was adequate for identification. As diamond treatments and synthetics have become more sophisticated, standard procedure now requires many more resources. Lasers across the UV-visible-NIR wavelength range should be used, as different laser wavelengths efficiently activate different ranges of PL features; the authors regularly use six different laser excitation wavelengths (325, 457, 488, 514, 633, and 830 nm). Over the next decade, PL spectroscopy in gemology will continue to evolve toward smaller, more portable instruments (see Breeding et al., 2010 for an extensive discussion) and different analytical domains, possibly to the less-studied PL dimensions of temperature, time, and spatial mapping.

Temperature- and Time-Resolved PL Analytical Possibilities. For the past decade or so, diamond PL analysis has been performed with the sample temperature stable and the laser power constant. In addition to the exploration of PLE applications (again, see Bidny et al., 2010), further investigations of temperature effects on photoluminescence and how PL features decay within the initial nanoseconds after the laser is switched off (time-resolved PL) may help solve complex identification problems.

For example, NV color centers in diamond appear identical in PL spectra of natural, treated, and synthetic samples. Does this center appear different for natural or treated stones at temperatures between liquid nitrogen and room temperature or at the even colder temperatures produced by liquid helium? Thermoluminescence (TL), the luminescence response as temperature is increased, has not yet been fully explored for gem materials. Researchers have used TL above room temperature in order to distinguish the dose of gamma radiation in treated CVD diamonds. At their experimental conditions, the response of natural diamonds was too weak for comparison (Karczmarska et al., 2012). Additionally, novel TL responses have been observed in diamond (Nelson and Breeding, 2011) and other colored stones (e.g., Choudhary, 2010).

For time-resolved luminescence, scientists examine the peak's behavior in the initial nanoseconds after a laser is turned off and the peak's emission dies off. Investigations of the decay curves of various diamond defects may reveal important differences between natural, treated, and synthetic diamonds that aid in their identification. Studies, particularly in biological fields, have shown that a great deal of molecular information is contained within the length of this decay time and within the shape of its decay curve. Additional intensity information could demonstrate two decay times, indicating the presence of multiple defects or energy states (Lakowicz, 2006). Researchers have also shown that the luminescence lifetime of the NV^0 center (ZPL at 575 nm) in diamond can be shortened by the presence of single substitutional nitrogen (Liaugaudas et al., 2012). Ongoing research is probing the differences in decay times of various color centers between natural, treated, and synthetic gems to expand beyond the standard "steady-state" PL measurements (e.g., figure 10; Eaton-Magaña, 2015).

Database of Large Quantities of Data. Prelas et al. (1998) estimated that 100 vibrational and 400 electronic optically active defects are possible within diamond. This quantity of measurable defects, combined with the large quantities of diamonds analyzed in a gem research laboratory, has generated vast repositories of spectral data—a specialized resource that cannot easily be duplicated in most academic environments. Thus, gemological laboratories are unique in their ability to ascertain large-scale spectral trends across thousands of diamonds. To take full advantage of the data, automatic software

PL Spectrum

Time-resolved Luminescence for H3 Peak
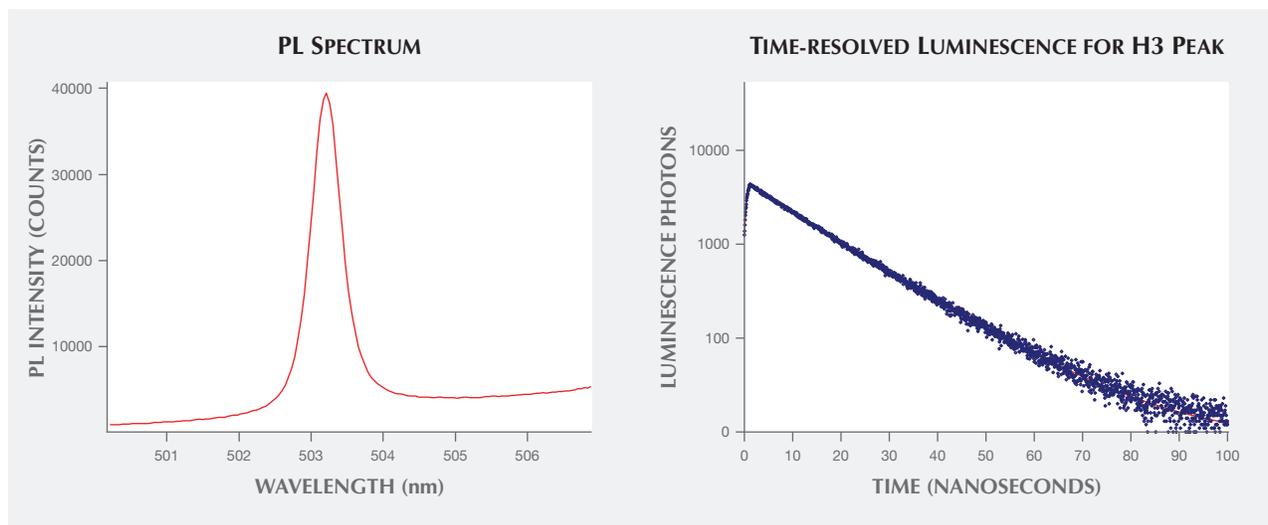
Figure 10. The photoluminescence spectrum for the H3 center (left) is collected with continuous laser power at 488 nm. When the laser is switched off, the luminescence of the H3 center decays very quickly—in about 100 billionths of a second. The rate and the shape of the decay curve can reveal additional information about the optical center. The decay curve shown here is for the H3 luminescence from a type IIa diamond at liquid nitrogen temperatures. By mathematically fitting the shape of the decay curve, it was determined to be bi-exponential. The dominant decay time is 16.6 nanoseconds (close to a previously reported value of 16.7 ± 0.5 ns (Liaugaudas et al., 2009), and the minor component has a decay of 10.7 nanoseconds.

processing is needed to find and analyze spectral peaks and incorporate them into a robust searchable database. Development of reliable peak-finding/ peak-fitting algorithms for rapid automatic process-

Average Peak Height in PL Among 54,208 Natural IIA Diamonds Using 514 nm Laser Excitation
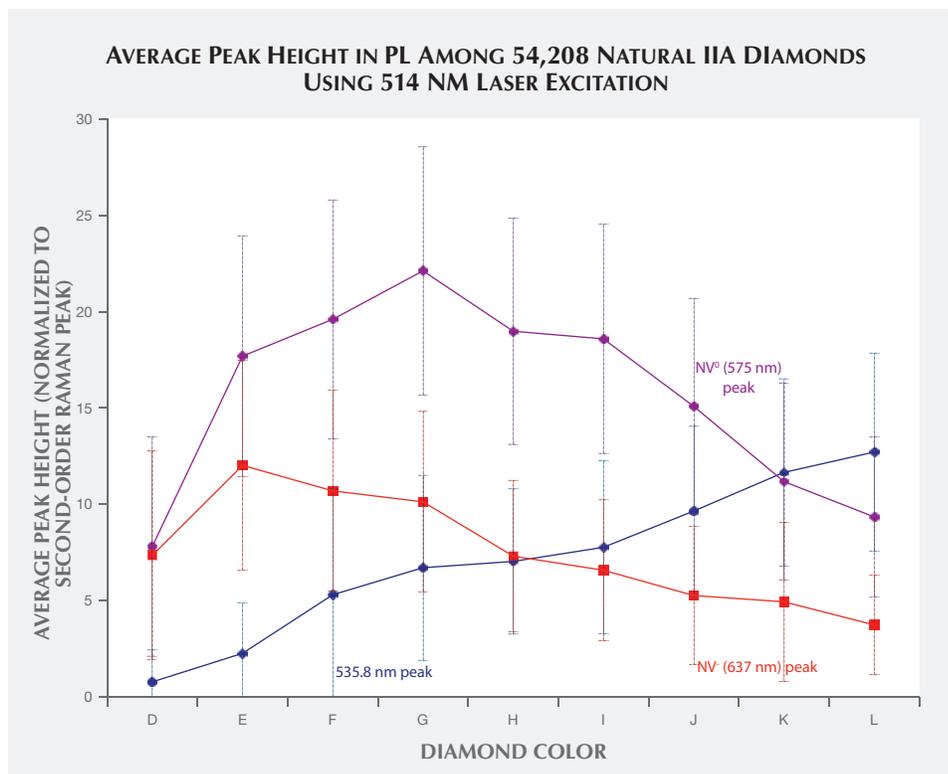
Figure 11. Using automatic peak finding and fitting software with batch processing capability, the incidence of many peaks occurring in PL spectra of diamond, including those at 535.8, 575, and 637 nm, can be determined for large quantities of spectra. Each data point represents at least 400 spectra; some encompass more than 10,000 spectra. All data were collected at liquid nitrogen temperature using 514 nm laser excitation. Peak heights were ratioed to the second-order diamond Raman line (596 nm) to remove the influence of laser power and instrumental fluctuation.

ing of all collected spectra is nearly as important as the analysis itself. Our work is ongoing, but we can find and characterize peaks based on their presence or absence and other peak characteristics such as height, as shown in figure 11. The large-scale data mining of spectra can reveal new patterns. For example, the configuration of the defect causing the 535.8 nm peak is unknown (figure 11), but the steady increase in peak height as color increases from D to L may indicate that its configuration is related to the origin of color in type IIa diamonds. The availability of bulk PL peak information from a vast supply of spectra opens numerous statistical possibilities for data analysis across thousands of samples, revealing trends and connections that were heretofore unseen.

CONCLUSION

Treated-color and synthetic diamonds are readily available in today's diamond market. Every gemstone, whether natural, laboratory grown, or color treated in some way, has a story behind its creation, and every customer has a right to know that story through proper identification. Over the last decade, PL analysis has become one of the most important tools to document these unique stone histories. PL has also proven to be a reliable gemological identification tool, helping laboratories properly disclose the origin and treatment history of diamonds and other gemstones to ensure public trust in the gem and jewelry industry. Ongoing research using PL and other analytical techniques will continue to unlock more of each gemstone's secrets.

ABOUT THE AUTHORS
Dr. Eaton-Magaña is a research scientist and Dr. Breeding is a senior research scientist at GIA's Carlsbad laboratory.

REFERENCES

Bidny A.S., Dolgova O.S., Baksheev I.A., Ekimenkova I.A. (2010) New data for distinguishing between hydrothermal synthetic, flux synthetic, and natural corundum. *Journal of Gemmology*, Vol. 32, No. 1–4, pp. 2–15.

Breeding C.M., Shigley J.E. (2009) The "type" classification system of diamonds and its importance in gemology. *G&G*, Vol. 45, No. 2, pp. 96–111, http://dx.doi.org/10.5741/GEMS.45.2.96

Breeding C.M., Wang W. (2008) Occurrence of the Si-V defect center in natural colorless gem diamonds. *Diamond and Related Materials*, Vol. 17, pp. 1335–1344, http://dx.doi.org/10.1016/j.diamond.2008.01.075

Breeding C.M., Shen A.H., Eaton-Magaña S., Rossman G.R., Shigley, J.E., Gilbertson A. (2010) Developments in gemstone analysis techniques and instrumentation during the 2000s. *G&G*, Vol. 46, No. 3, pp. 241–257, http://dx.doi.org/10.5741/GEMS.46.3.241

Chalain J.-P., Fritsch E., Hänni H.A. (2000) Identification of GE POL diamonds: A second step. *Journal of Gemmology*, Vol. 27, No. 1, pp. 65–72.

Choudhary G. (2010) Gem News International: A strongly thermoluminescent spodumene. *G&G*, Vol. 46, No. 4, pp. 322–323.

Collins A.T. (2001) The colour of diamond and how it may be changed. *Journal of Gemmology*, Vol. 18, No. 1, pp. 341–359.

Collins A.T. (2003) The detection of colour-enhanced and synthetic gem diamonds by optical spectroscopy. *Diamond and Related Materials*, Vol. 12, No. 10/11, pp. 1976–1983.

Collins A.T., Kanda H., Kitawaki H. (2000) Colour changes produced in natural brown diamonds by high-pressure, high-temperature treatment. *Diamond and Related Materials*, Vol. 9, No. 2, pp. 113–122, http://dx.doi.org/10.1016/S0925-9635(00)00249-1

Dischler B. (2012) *Handbook of Spectral Lines in Diamond: Volume 1: Tables and Interpretations*. Springer, Heidelberg, Germany.

Dobrinets I.A., Vins V.G., Zaitsev A.M. (2013) *HPHT-Treated Diamonds: Diamonds Forever*. Springer, Heidelberg, Germany.

Eaton-Magaña S. (2015) Comparison of luminescence lifetimes from natural and laboratory irradiated diamonds. *Diamond and Related Materials*, Vol. 58, pp. 94–102, http://dx.doi.org/10.1016/j.diamond.2015.06.007

Eaton-Magaña S., Lu R. (2011) Phosphorescence in type IIb diamonds. *Diamond and Related Materials*, Vol. 20, pp. 983–989, http://dx.doi.org/10.1016/j.diamond.2011.05.007

Eaton-Magaña S., Post, J. Heaney P.J., Walters R., Breeding C.M., Butler J.E. (2007) Fluorescence spectra of colored diamonds using a rapid, mobile spectrometer. *G&G*, Vol. 43, No. 4, pp. 332–351, http://dx.doi.org/10.5741/GEMS.43.4.332

Eaton-Magaña S., Post, J. Heaney P.J., Freitas J., Klein P., Walters R., Butler J.E. (2008) Using phosphorescence as a fingerprint for the Hope and other blue diamonds. *Geology*, Vol. 36, No. 1, pp. 83–86, http://dx.doi.org/10.1130/G24170A.1

Fiquet G., Richet P., Montagnac G. (1999) High-temperature thermal expansion of lime, periclase, corundum, and spinel. *Physics and Chemistry of Minerals*, Vol. 27, No. 2, pp. 103–111, http://dx.doi.org/10.1007/s002690050246

Fisher D., Spits R.A. (2000) Spectroscopic evidence of GE POL HPHT-treated natural type IIa diamonds. *G&G*, Vol. 36, No. 1, pp. 42–49, http://dx.doi.org/10.5741/GEMS.36.1.42

Green B.L. (2013) Optical and magnetic resonance studies of point defects in single crystal diamond. Doctoral dissertation, University of Warwick, http://wrap.warwick.ac.uk/58600/1/WRAP_THESIS_Green_2013.pdf [Accessed 12/14/15]

Hainschwang T., Leggio L. (2006) The characterization of tortoise shell and its imitations. *G&G*, Vol. 42, No. 1, pp. 36–52, http://dx.doi.org/10.5741/GEMS.42.1.36

Hainschwang, T. Simic D., Fritsch E., Deljanin B., Woodring S. DelRe N. (2005) A gemological study of a collection of chameleon diamonds. *G&G*, Vol. 42, No. 1, pp. 20–35.

Halperin A., Chen R. (1966) Thermoluminescence of semiconducting diamonds. *Physical Review*, Vol. 148, No. 2, pp. 839–845, http://dx.doi.org/10.1103/PhysRev.148.839

Hounsome L.S., Jones R., Martineau P.M., Fisher D., Shaw M.J., Briddon, Öberg S. (2006) Origin of brown coloration in diamond. *Physical Review B*, Vol. 73, pp. 125203-1–125203-8, http://dx.doi.org/10.1103/PhysRevB.73.125203

Inns A.S., Breeding C.M. (2007) Lab Notes: Natural type IIb blue diamond with atypical electroluminescence. *G&G*, Vol. 43, No. 3, pp. 246–248.

Karampelas S., Fritsch E., Hainschwang T., Gauthier J.-P. (2011) Spectral differentiation of natural-color saltwater cultured pearls from *Pinctada margaritifera* and *Pteria sterna*. *G&G*, Vol. 47, No. 2, p. 117.

Karczmarska A., Mitura-Nowak M., Nowak T., Marszalek M. (2012) Study of the thermoluminescence of CVD diamond. *Acta Physica Polonica A*, Vol. 121, No. 2, pp. 510–513.

Kitawaki H., Okano M. (2006) Spinel up to date. *GAAJ Research Lab Report*, http://grjapan.ddo.jp/gaaj_report/2006/2006_0301en.html

Kondo D., Befi R., Beaton D. (2010) Lab Notes: Heat-treated spinel. *G&G*, Vol. 46, No. 2, pp. 145–146.

Lakowicz J.R. (2006) *Principles of Fluorescence Spectroscopy*, 3rd ed. Springer Science + Business Media, New York.

Liaugaudas G., Collins A.T., Suhling K., Davies G., Heintzmann R. (2009) Luminescence-lifetime mapping in diamond. *Journal of Physics: Condensed Matter*, Vol. 21, No. 36, 364210-1–364210-7, http://dx.doi.org/10.1088/0953-8984/21/36/364210

Liaugaudas G., Davies G., Suhling K., Khan R.U.A., Evans D.J.F. (2012) Luminescence lifetimes of neutral nitrogen-vacancy centres in synthetic diamond containing nitrogen. *Journal of Physics: Condensed Matter*, Vol. 24, 435503-1–435503-5.

Lim H., Park S., Cheong H., Choi H.-M., Kim Y.C. (2010) Discrimination between natural and HPHT-treated type IIa diamonds using photoluminescence spectroscopy. *Diamond and Related Materials*, Vol. 19, No. 10, pp. 1254–1258.

Luo Y., Breeding C. (2013) Fluorescence produced by optical defects in diamond: Measurement, characterization, and challenges. *G&G*, Vol. 49, No. 2, pp. 82–97, http://dx.doi.org/10.5741/GEMS.49.2.82

Nelson D., Breeding C.M. (2011) Lab Notes: Thermoluminescence from type IaB diamonds. *G&G*, Vol. 47, No. 1, p. 50.

Pegasus Overseas Limited, Lazare Kaplan International, General Electric Company—press release (1999) Diamonds.net, March 25, http://www.diamonds.net/News/NewsItem.aspx?ArticleID=2801 [Accessed 12/10/2015].

Prelas M.A., Popovici G., Bigelow L.K. (1998) *Handbook of Industrial Diamonds and Diamond Films*. Marcel Dekker, New York.

Read P.G. (2008) *Gemmology*, 3rd ed. Elsevier Butterworth-Heinemann, Oxford, UK.

Saeseaw S., Wang W., Scarratt K., Emmett J.L., Douthit T.R. (2009) "Distinguishing heated spinels from unheated natural spinels and from synthetic spinels," *GIA Research News*, www.gia.edu/gia-news-research-NR32209A [Date accessed: 3/19/15].

Sauer M., Hofkens J., Enderlein J. (2010) *Handbook of Fluorescence Spectroscopy and Imaging: From Ensemble to Single Molecules*. John Wiley & Sons, New York.

Schmetzer K. (2010) High pressure high temperature treatment of diamonds—a review of the patent literature from five decades (1960–2009). *The Journal of Gemmology*, Vol. 32, No. 1–4, pp. 52–65.

Shigley J.E., Breeding C.M. (2013) Optical defects in diamond: A quick reference chart. *G&G*, Vol. 45, No. 2, pp. 107–111, http://dx.doi.org/10.5741/GEMS.49.2.107

Shigley J., Moses T., Reinitz I., Elen S., McClure S.F., Fritsch E. (1997) Gemological properties of near-colorless synthetic diamonds. *G&G*, Vol. 33, No. 1, pp. 42–53, http://dx.doi.org/10.5741/GEMS.33.1.42

Shigley J., Moses T., McClure S., Van Dael M. (1999) GIA reports on GE POL diamonds. *Rapaport Diamond Report*, Vol. 22, No. 36 (October 1), pp. 1, 11, 14, 18.

Smith C.P., McClure S.F., Eaton-Magaña S., Kondo D.M. (2007) Pink-to-red coral: A guide to determining origin of color. *G&G*, Vol. 43, No. 1, pp. 4–15, http://dx.doi.org/10.5741/GEMS.43.1.4

Song Z., Lu T., Lan Y., Shen M., Ke J., Liu J., Zhang Y. (2012) The identification features of undisclosed loose and mounted CVD synthetic diamonds which have appeared recently in the NGTC laboratory. *Journal of Gemmology*, Vol. 33, No. 1–4, pp. 2–15.

Wang W., Scarratt K., Hyatt A., Shen A. H.-T., Hall M. (2006) Identification of "chocolate pearls" treated by Ballerina Pearl Co. *G&G*, Vol. 42, No. 4, pp. 222–235, http://dx.doi.org/10.5741/GEMS.42.4.222

Wang W., Hall M.S., Moe K.S., Tower J., Moses T.M. (2007) Latest generation CVD-grown synthetic diamonds from Apollo Diamond Inc. *G&G*, Vol. 43, No. 4, pp. 294–312, http://dx.doi.org/10.5741/GEMS.43.4.294

Wang W., D'Haenens-Johansson U.F.S., Johnson P., Moe K.S., Emerson E., Newton M.E., Moses T.M. (2012) CVD synthetic diamonds from Gemesis Corp. *G&G*, Vol. 48, No. 2, pp. 80–97, http://dx.doi.org/10.5741/GEMS.48.2.80

Welbourn C.M., Cooper M., Spear P.M. (1996) De Beers natural versus synthetic diamond verification instruments. *G&G*, Vol. 32, No. 3, pp. 156–169, http://dx.doi.org/10.5741/GEMS.32.3.156

Williams B. (2007) Technology update—Ultraviolet light. *Gem Market News*, Vol. 26, No. 1, pp. 8–11.

Wotherspoon A., Steeds J.W., Catmull B., Butler J. (2003) Photoluminescence and positron annihilation measurements of nitrogen doped CVD diamond. *Diamond and Related Materials*, Vol. 12, pp. 652–657, http://dx.doi.org/10.1016/S0925-9635(02)00229-7

Zaitsev A.M. (2003) *Optical Properties of Diamond: A Data Handbook*. Springer-Verlag, Berlin.

CHRYSOBERYL RECOVERED WITH SAPPHIRES IN THE NEW ENGLAND PLACER DEPOSITS, NEW SOUTH WALES, AUSTRALIA

Karl Schmetzer, Franca Caucia, H. Albert Gilg, and Terrence S. Coldham

Mineralogical, chemical, and spectroscopic properties of chrysoberyl crystals recovered from sapphire placer deposits, related to Tertiary volcanic rocks, in the New England gem fields in New South Wales (NSW), Australia, are presented. The samples appeared yellow, yellowish brown, or brown in transmitted light, and some crystals revealed a distinct sectorial zoning between brown *i* (011) and yellow *o* (111) growth areas. In reflected light, the *i* sectors showed a whitish appearance, and cabochon-cut samples with larger whitish *i* sectors displayed chatoyancy. On the basis of morphological properties, trace-element contents, and absorption spectra, the chrysoberyl samples were subdivided into four different groups, possibly originating from different host rocks. The largest such group, comprised of samples with distinct sectorial color zoning, also revealed a pronounced variation in trace-element levels of titanium, niobium, and tantalum between the different growth sectors. Smaller variations were found for boron, magnesium, and iron, and almost no variation was observed for gallium.

Chrysoberyl is formed through various magmatic and metamorphic processes. Two broad categories of deposits are widely known: those related to pegmatitic activity and those related to high-grade metamorphism. In particular, chrysoberyl is frequently crystallized directly from a pegmatite melt or in a reaction zone between a pegmatitic melt and aluminum-rich host rocks. With respect specifically to the chromium-bearing color-change chrysoberyl variety alexandrite, formation often occurs by reaction of a pegmatite intruding mafic or ultramafic rocks. Chrysoberyl is also found in high-grade (amphibolite-facies or granulite-facies) metamorphic rocks. Augmenting these primary occurrences, placer deposits may be derived from any of the foregoing types (Okrusch, 1971; Soman and Druzhinin, 1987; Franz and Morteani, 2002; Černý, 2002; Barton and Young, 2002; Beurlen et al., 2013). Such secondary deposits of gem-quality chrysoberyl related to high-grade metamorphic rocks are found, for example, in Sri Lanka, India, Tanzania, and Madagascar (Menon et al., 1994; Gunaratne and Dissanayake, 1995; Henn and Milisenda, 1997; Dissanayake et al., 2000; Milisenda et al., 2001; Manimaran et al., 2007). Likewise, secondary deposits related to pegmatites or pegmatites intruding aluminum-rich rocks have been discovered, for instance, in various Brazilian states (Proctor, 1988; Cassedanne and Roditi, 1993; Pedrosa-Soares et al., 2009).

Chrysoberyl recovered with sapphires related to volcanic host rocks, in contrast, is extremely rare. Among the limited discoveries, this type of chrysoberyl has been mentioned in connection with secondary deposits in Australia, related to Tertiary volcanic host rocks, including in Anakie, Queensland (Brightman, 1984); in the New England gem fields of New South Wales (NSW; figure 1) (Coenraads, 1990,
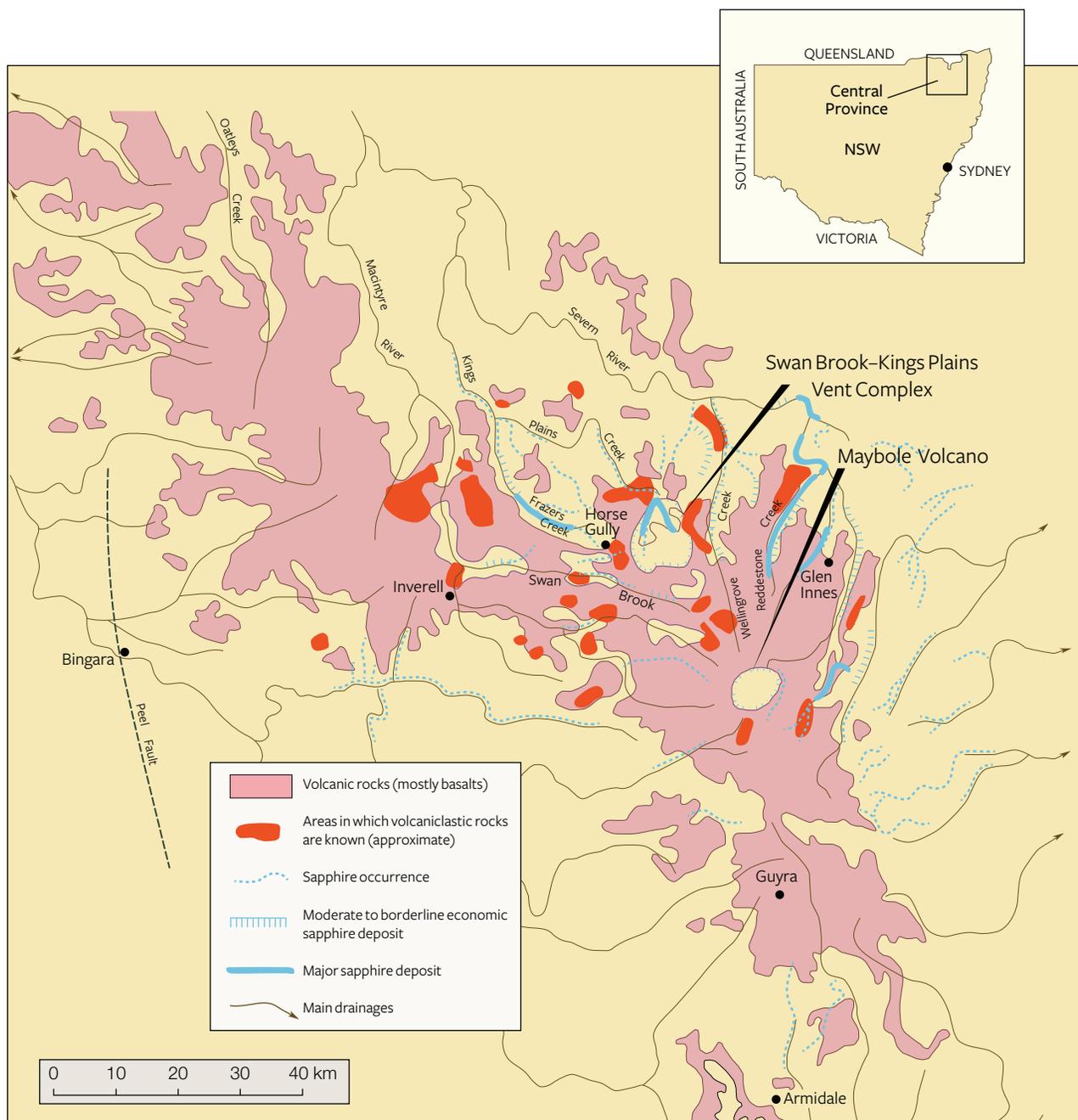
Figure 1. Extent of the Tertiary volcanic rocks of the New England sapphire fields. Rarely chrysoberyl is found associated with sapphire and other minerals in the Swan Brook–Kings Plains Vent Complex and Maybole Volcano occurrences (above right). Specimens in this study were recovered mostly from the Swan Brook–Kings Plains deposits. Adapted from Facer and Stewart (1995).

1991, 1995); and in northeastern Tasmania (Sweeney, 1995; Bottrill, 1996). Further mineralogical or gemological information, however, is minimal. For instance, although chrysoberyl was recognized in the late 19th century as occurring in association with gem-quality sapphires in the secondary New England gem fields (Liversidge, 1876, 1888), no comprehensive description of the material is available. Thus, the present study was undertaken to examine a collection of samples from these New England placer deposits and thereby to determine mineralogical and chemical properties for this type of chrysoberyl.

Figure 2. Left: The mineral concentrate obtained from the processing plant of the New England placer deposits was traditionally sorted and graded on mirrors, as seen in this photo taken in 1967. Right: A collection of unusual minerals from the New England sapphire deposits set aside by sorting staff over a period of years. The pieces indicated by the arrows are possibly chrysoberyl found among silky blue, pink, yellow, green, and golden sapphires, as well as zircons and other minerals. Field of view about 8 × 6 cm. Photos by T.S. Coldham.

MATERIALS AND METHODS

Because chrysoberyl associated with Australian sapphires shedding from Tertiary basalts and pyroclastics occurs only very rarely, miners often do not recognize the crystals. Rather, the stones are mistaken for corundum and sold within parcels of yellow and parti-colored rough sapphires.

The present study began with 39 crystals or crystal fragments and one chatoyant cabochon previously cut from such material. The research material was selected by one of the authors (TSC) from approximately 1 kg of rough, which had been purchased from the late Tom Nunan, one of the larger sapphire miners operating in the New England sapphire fields (Coldham, 2014). The rough parcel was comprised of a collection of atypical-appearing stones that were set aside by sapphire sorters over many years from the production of several mines in the New England region, including Swanbrook Creek, Reddestone Creek, and Kings Plains (for a general overview of the New England sapphire fields, see Coenraads, 1990, 1991, 1994; Abduriyim et al., 2012 a,b). These unusual stones were essentially anything that had

caught the eyes of the sorters by virtue of being different from the blue, yellow, green, and low-quality sapphire commonly seen (figure 2). The collection included multiple types of material rare to the area, such as pink, purple, red, and orange corundum; unusually shaped stones; and those with strange color banding. Most stones within this kilogram of rough material were quite small, under 2 ct in weight.

As might be expected from the process of visual selection just described, the possibility remained that the initial 40 research samples (in total weighing about 65 carats) might still contain some corundum crystals. For this reason, all rough samples were first examined by traditional gemological methods, especially in the immersion microscope to facilitate observation of specific growth structures and sectorial zoning. Because some of the smaller crystal fragments did not show any microscopic properties of diagnostic value (i.e., neither characteristic growth structures nor mineral inclusions), these smaller samples were tested by micro-Raman spectroscopy using a Horiba XploRA confocal Raman microscope facility with a 532 nm laser. Micro-Raman spectroscopy was also employed

to confirm the identity of several larger crystals. In total, 20 samples were examined by Raman spectroscopy; ultimately, six smaller crystal fragments were identified as yellow corundum. The present study is thus based on the remaining 34 chrysoberyl samples originating from the secondary New England sapphire deposits. To have found and selected only this small quantity of chrysoberyl associated with many thousands of kilograms of rough sapphire related to Tertiary volcanics mined over many years reiterated the rarity of the material.

The weight and size of the research material ranged from 11.71 ct (17.4 × 8.9 mm) to 0.45 ct (5.3 × 2.9 mm) for the rough samples. Coenraads (1995) reported similar sizes in the 10 to 5 mm range for chrysoberyl from the New England gem fields.

To better observe the structures without interference from the rough, heavily corroded and/or mechanically abraded or otherwise contaminated surfaces, certain samples were "windowed" with one or two polished faces, and a small group of transparent stones was completely faceted (figure 3, left). A few samples with larger whitish areas were cut as cabochons showing chatoyancy (figure 3, right).

In the present paper, the term "sectorial zoning" or "sectorial color zoning" is used to describe a different coloration between adjacent growth sectors, while "color zoning" refers to different colors within a specific growth sector. For all the chrysoberyls studied (samples in the as-received state, windowed crystals, or cut samples), growth structures, sectorial

zoning, and color zoning were determined by immersion microscopy in methylene iodide using the methods described by Schmetzer (2011). Four cabochon-cut samples showing chatoyancy were examined in reflected light using a Leitz Ortholux II Pol-BK polarization microscope at high magnification (up to 1000×).

In Brief

- Gem-quality chrysoberyl crystals in yellow to brownish colors have been recovered in very small quantities over a period of many years from the sapphire placer deposits in the New England gem fields, New South Wales, Australia.

- Some samples exhibit chatoyancy after cutting as cabochons.

- Variations in morphology, growth zoning, color zoning, trace element contents, and spectroscopic properties enabled the samples to be divided into four groups.

- The largest two groups of the chrysoberyls showed distinct sectorial growth zoning combined with color zoning, and yellowish brown or brown growth sectors displayed pleochroism.

To obtain an overview of the qualitative chemical composition, 10 chrysoberyls were tested by energy-dispersive X-ray fluorescence spectroscopy (EDXRF) using a Bruker Tracer III-SD handheld unit.

Figure 3. Some of the chrysoberyl research samples from the sapphire placer deposits in the New England area were faceted, while others were cut as cabochons, showing chatoyancy. Left: The faceted yellow sample weighs 0.53 ct and measures 5.8 × 4.4 mm. Right: The cat's-eye cabochons range from 1.34 ct (6.5 × 5.9 mm) to 0.64 ct (5.1 × 4.7 mm). Photos by K. Schmetzer.

Quantitative trace-element composition of 12 chrysoberyls was determined by means of laser ablation–inductively coupled plasma–mass spectroscopy (LA-ICP-MS), employing a Quantel Brilliant 266 nm Nd:YAG laser coupled to a PerkinElmer DRCe quadrupole ICP-MS. NIST SRM 610 glass was used as the external calibration standard, and Al served as the internal standard. The spot size was set to approximately 50 μm and the frequency to 10 Hz. To determine chemical zoning within the samples, traverses consisting of four to twelve single analysis points were recorded for all 12 chrysoberyls examined by LA-ICP-MS. The analysis was carried out on 55 elements; only those elements with concentrations higher than the detection limits are reported (see table 3).

Absorption spectra were obtained for six of the chemically analyzed samples with a CCD-type Czerny-Turner spectrometer in combination with an integrating sphere (for further details, see Schmetzer et al., 2013a). Only non-polarized spectra were recorded.

RESULTS

The chrysoberyls from the New England placer deposits in New South Wales were free of mineral inclusions when examined using the magnification of the gemological microscope (up to 100×), but they showed variation in chemical composition, internal

Figure 4. Examples of chrysoberyl samples recovered from the sapphire placer deposits in the New England gem fields. The research samples were subdivided into four groups (indicated I through IV in black). The Arabic numerals correlate with the analyses given in table 3. The faceted yellow sample 1 (upper left) measures 5.8 × 4.4 mm and weighs 0.53 ct. Photo by K. Schmetzer.

TABLE 1. Morphology of chrysoberyls from the New England sapphire fields, NSW, Australia.

Crystal form	Designation	Miller indices (hkl)*
Pinacoid	a	{100}
	b	{010}
Prism	i	{011}
	s	{120}
	r	{130}
Dipyramid	o	{111}
	w	{122}
	n	{121}

*Based on a morphological cell with a = 4.42, b = 9.39, c = 5.47

Characteristic views

Direction of view	Symbol	Faces observed
Parallel to the a-axis	[100]	b, i
Parallel to the c-axis	[001]	a, b, s, r
Intermediate between b- and c-axes (parallel to the prism i and the dipyramid o)	[011]	i, w, o, a
Intermediate between a-, b-, and c-axes	[111]	i, n

morphology (growth structures and sectorial zoning), color, and color zoning. Thus, trace-element contents, color, internal growth features, sectorial zoning, color zoning, and spectroscopic properties were used to subdivide the samples into four primary groups, designated as groups I through IV in this study (figure 4). The few samples from the original group of 40 that showed mineral inclusions in the gemological microscope (e.g., zircon crystals with tension cracks) were all identified by Raman spectroscopy as corundum.

Morphology and Growth Features. The different crystal forms present in the New England chrysoberyls are listed in table 1. The habit of the samples was formed by the combination of two pinacoids *a* and *b*; three prism faces *i*, *s*, and *r*; and three dipyramids *o*, *w*, and *n*.

When examined in the immersion microscope, there were three main directions of view presenting the major internal growth features: parallel to the a-axis, parallel to the c-axis, and intermediate between the b- and c-axes. A fourth direction intermediate between the a-, b-, and c-axes was of less importance (see also table 1). A characteristic crystal showing the

main crystal forms is depicted in figure 5A. In a view parallel to the a-axis, growth features parallel to the prism *i* and occasionally parallel to the pinacoid *b* were observed (figures 5C and 6). In a view parallel to the c-axis, growth features and faces seen were the

Figure 5. Morphology of a chrysoberyl crystal from the New England gem fields with prismatic habit. A: This clinographic projection shows the pinacoids a (100) and b (010), the prisms s (120) and i (011), and the dipyramid o (111). B: In a view parallel to the c-axis, growth zoning and morphological features parallel to the faces a, b, and s are observed. C: In a view parallel to the a-axis, growth zoning and morphological features parallel to the faces b and i are observed. D: In a view parallel to the prism i and the dipyramid o (indicated by an arrow in A), growth zoning and morphological features parallel to the faces a, o, and i are observed; within the four groups of samples, the relative sizes of the i prism and the o dipyramid vary (D1, D2, D3). Illustrations by K. Schmetzer.
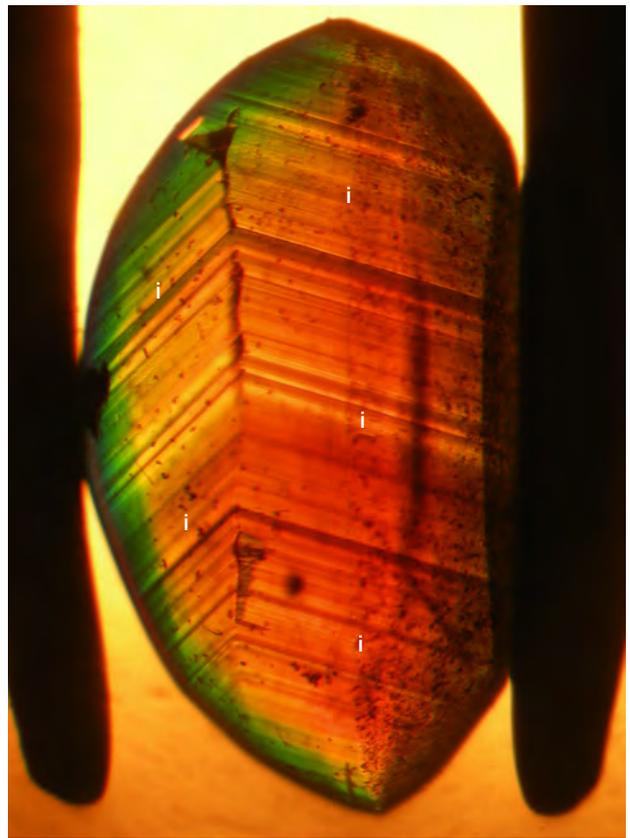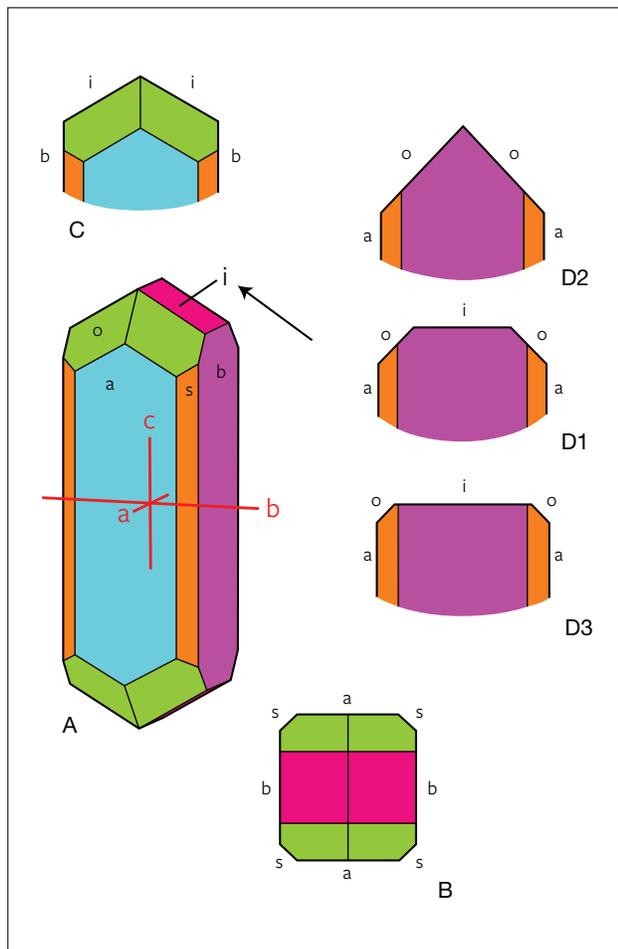
Figure 6. A view of a cabochon-cut chrysoberyl parallel to the a-axis shows growth zoning parallel to the prism i. Immersion, field of view 5.1 × 3.8 mm. Photomicrograph by K. Schmetzer.

pinacoids *a* and *b*, the prism *s*, and less frequently the prism *r* (figures 5B and 7). The different growth sectors in this latter view could also show sectorial zoning and color zoning.

In a view between the b- and c-axes and parallel to the [011] direction (i.e., parallel to the prism *i* and the dipyramid *o*), the faces *a*, *o*, and *i* were observed, occasionally in combination with a small *w* dipyramid. This view also revealed the principal variation among the samples in crystal morphology (figure 5, D1, D2, and D3). In some samples, the size of the *i* prism faces was balanced with the size of the o dipyramids (figure 5, D1). In others, either the *o* or the *i* faces predominated. If the *o* faces were dominant, the *i* prism was small or not observed (figure 5, D2). If the *i* faces were dominant, the *o* dipyramid was smaller (figure 5, D3).

In an intermediate direction between the a-, b-, and c-axes, a combination of *i* and *n* faces was occasionally seen (figure 14).
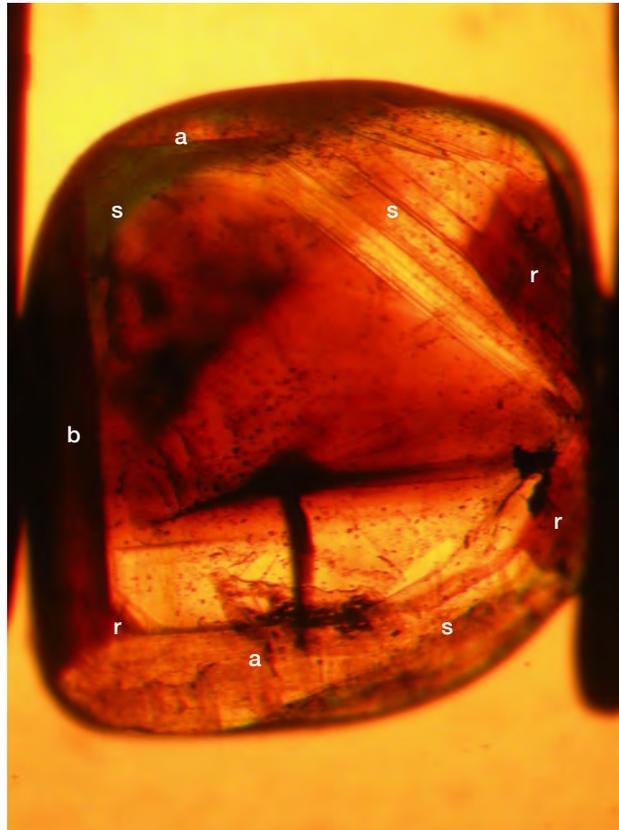
Figure 7. A view of a rough chrysoberyl crystal parallel to the c-axis shows growth zoning associated with sectorial zoning and color zoning parallel to the pinacoids a *and* b *as well as parallel to the prism faces* s *and* r. *Immersion, field of view 5.3 × 4.0 mm. Photomicrograph by K. Schmetzer.*

Taking into account color and these just-described morphological features, the four groups were characterized as follows (see table 2 and figure 8, examples I through IV):

- Group I: yellow color, *o* dipyramids dominant, no sectorial zoning, no color zoning
- Group II: yellow color, size of *o* dipyramids and *i* prism faces balanced, weak to absent color zoning or sectorial zoning
- Group III: yellow to brownish yellow or yellowish brown color, size of *o* dipyramids and *i* prism faces balanced, strong sectorial zoning in which *o* growth sectors were yellow and *i* growth sectors had a whitish appearance in reflected light but were yellowish brown to brown in transmitted light, color zoning in various

zones but primarily in *i* growth sectors (see also figures 9 and 10)

- Group IV: brownish yellow or yellowish brown color, *i* prism faces dominant, sectorial zoning in which small *o* growth sectors were yellow and *i* growth sectors were whitish in reflected light but yellowish brown to brown in transmitted light, color zoning mainly in *i* growth sectors. This group also contained the only two twinned crystals within the 34 chrysoberyls examined (figure 11).

The samples of groups I and II and the predominantly yellow zones of chrysoberyls from groups III

Figure 8. A view parallel to the prism i *and the dipyramid* o *of four rough chrysoberyl crystals (one from each of the groups I through IV) shows growth zoning for all of the samples. Sectorial color zoning parallel to the pinacoid* a, *to the prism* i, *and to the dipyramid* o *is observed for samples from groups III and IV. A variation in habit is caused by the relative size of the prism* i *and the dipyramid* o *(see figure 5). Immersion, field of view 4.9 × 3.7 mm (I), 3.9 × 2.9 mm (II), 3.5 × 2.6 mm (III), 6.0 × 4.5 mm (IV). Photomicrographs by K. Schmetzer.*
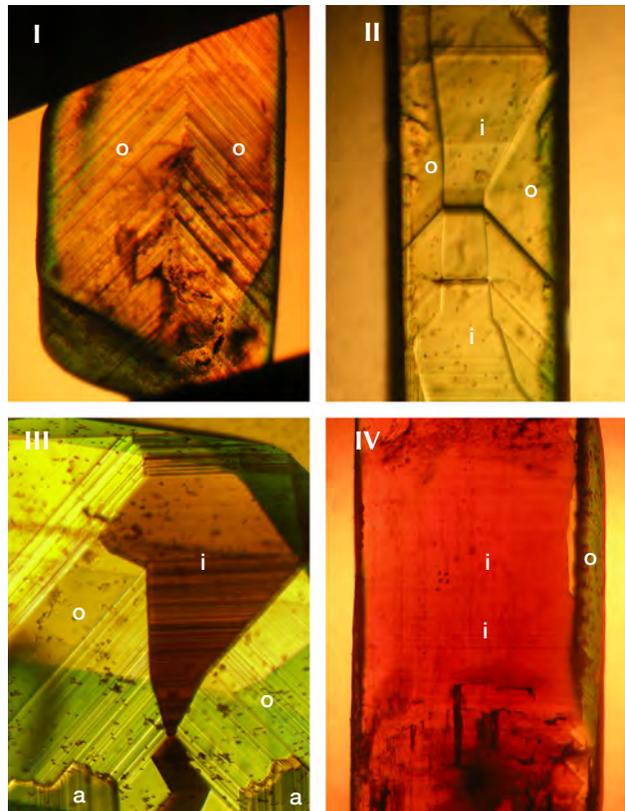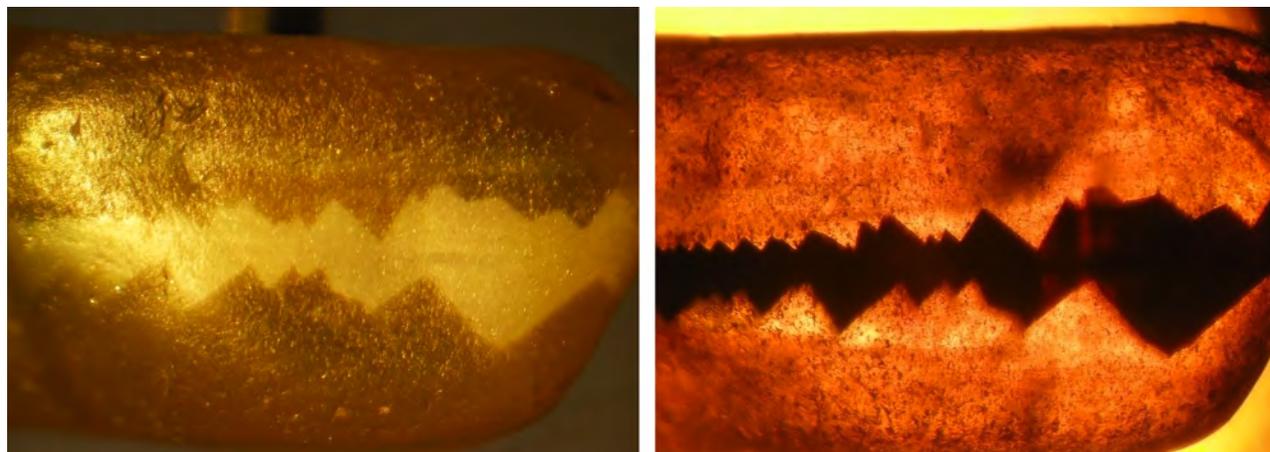
Figure 9. A view of a rough chrysoberyl crystal from group III parallel to the prism i *shows growth zoning associated with sectorial color zoning parallel to the prism* i *(core) and parallel to the dipyramid* o *(rim). The* i *growth sector appears whitish in reflected light (left) and brown in transmitted light in immersion (right). Field of view 9.5 × 7.1 mm. Photomicrographs by K. Schmetzer.*

and IV occasionally showed an additional slight greenish hue.

The second morphological feature that influenced the habit of the crystals was the relative size of the *a* and *b* pinacoids. Chrysoberyls in which the sizes of the *a* and *b* pinacoids were balanced showed prismatic habit (figure 12 A,B,D,E), while samples with larger *a* faces were platy or tabular (figure 12C) and could also be twinned (figure 12F).

In a few samples of groups II and III, subordinate *w* and *n* dipyramids were also apparent (figures 12D, 13, and 14).
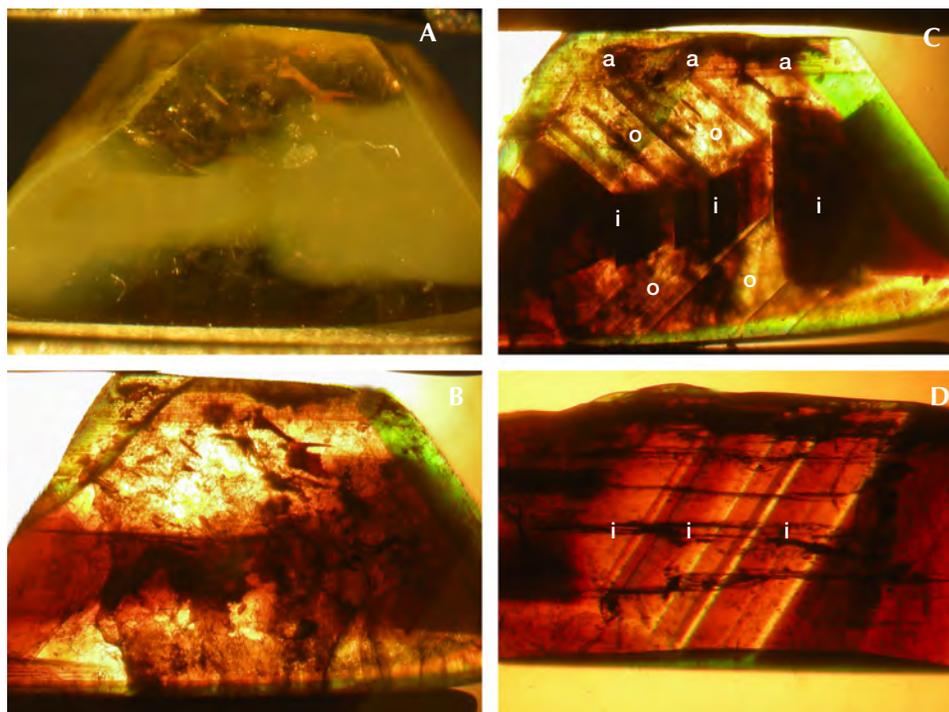
Figure 10. A view of a rough chrysoberyl crystal from group III shows sectorial zoning parallel to the faces i *(core),* o, *and* a *(rim); color zoning is observed especially within the* i *growth sectors. A and B: Views parallel to the b-axis in reflected light (A) and in transmitted light (B), with the* i *growth sector appearing whitish in reflected light and brown in immersion in transmitted light. C: View parallel to the prism* i *and the dipyramid* o *in immersion showing a sharp growth pattern associated with sectorial zoning. D: View parallel to the a-axis in immersion showing color zoning. Field of view 5.5 × 4.1 mm. Photomicrographs by K. Schmetzer.*
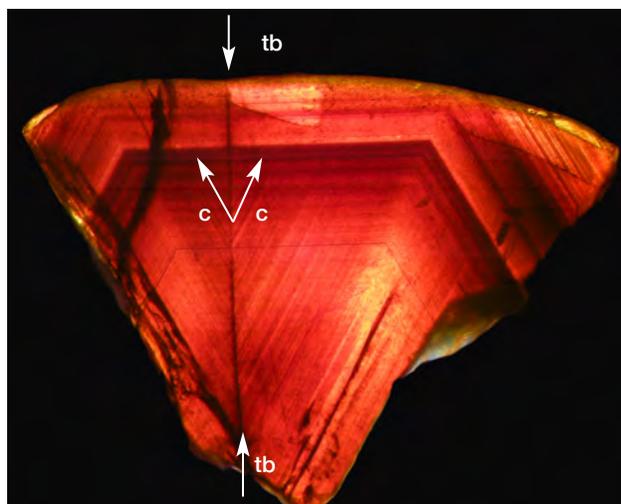
Figure 11. A view of a twinned chrysoberyl crystal parallel to the a-axis shows growth zoning parallel to the prism i *in both parts of the twin (the twin boundary* tb *is indicated by arrows). Growth striations parallel to the c-axis are also observed in both parts of the twin, forming a V-shaped pattern (the two c-axes are outlined). Compare with figure 12F. Immersion, field of view 10.8 × 8.1 mm. Photomicrograph by K. Schmetzer.*

Figure 12. Morphology of chrysoberyl crystals recovered from the basalt-related sapphire placer deposits in the New England gem fields (clinographic projections). The crystals show prismatic (A, B, D, and E) or tabular (C and F) habit, and crystal F is twinned. The crystal drawings represent chrysoberyls of group I (crystal A), II (crystals B and C), III (crystals B, C, and D), and IV (crystals E and F). Illustrations by K. Schmetzer.

In certain crystals it was possible to see an additional series of planes inconsistent with the typically observed growth pattern. An example in which such a series of parallel lines crossed the normal growth pattern of *a*, *o*, *w*, and *i* planes is depicted in figure 15. In the particular example presented here, this series of additional planes was identified according to its orientation to other common growth planes and runs parallel to the dipyramid (114), a face observed as a growth plane neither in chrysoberyls from New England nor in crystals from other locations. The system of planes was not parallel to the common twin plane of chrysoberyl (031) either.

Chemical Composition. Along with the main components of chrysoberyl (beryllium, aluminum, and oxygen), all samples contained distinct amounts of iron as well as minor amounts or traces of boron, magnesium, titanium, gallium, niobium, and tantalum. The analyses are summarized in table 3, and a graphical representation is given in figure 16. For each of the group III samples, the analyses were subdivided into the following categories: whitish-appearing growth zones, designated "core" and representing prismatic *i* growth sectors; and yellow growth zones,

designated "rim" and representing dipyramidal *o* and occasionally pinacoidal *a* growth sectors. An example of such a sample is depicted in figure 17. Augmenting the quantitative data obtained by LA-ICP-MS, X-ray fluorescence showed that all samples also contained traces of tin, but no suitable standard for quantitative determination of this trace element by laser ablation was available.

For the group III samples that showed a distinct sectorial zoning, the *i* growth sectors (core) always contained distinctly higher amounts of titanium, niobium, and tantalum, whereas moderately elevated

	Group I	Group II	Group III	Group IV
Color, visual appearance	Yellow, sometimes with a slightly greenish hue	Yellow, sometimes with a slightly greenish hue	Yellow to yellowish brown with whitish reflective growth zones	Yellowish brown with whitish reflective growth zones
No. of samples	4	4	17	9
Dominant crystal forms	a, b, o	a, b, o, i	a, b, o, i	a, b, i
Subordinate crystal forms	s	s, r, n, w	s, r, n, w	s, o
Dominant growth zoning	o	a, o, i	a, o, i	a, i
Subordinate growth zoning		n, w	s, r, n, w	o
Characteristic crystal drawings	figure 12A	figure 12B, C	figure 12B, C, D	figure 12E, F
Characteristic microscopic growth structures	figure 8I	figure 8II	figures 7, 8III, 9, 10, 13, 14, 15	figures 6, 8IV, 11
Spectroscopic properties	Iron-related absorption bands	Iron-related absorption bands	Iron-related absorption bands plus a continuously increasing absorption from the red to the violet and ultraviolet range	Iron-related absorption bands plus a continuously increasing absorption from the red to the violet and ultraviolet range

amounts of boron, magnesium, and iron were found in the rim. Only a minor zoning was observed for gallium, with slightly elevated contents in the rim (figures 16 and 17). For the group I, II, and IV chrysoberyls, traverses of several analysis points measured across the samples revealed no significant zoning.

Figure 13. A view of a rough chrysoberyl crystal from group III parallel to the prism i *and the dipyramid* o *shows growth zoning associated with sectorial color zoning parallel to the prism* i *(core) as well as parallel to the dipyramid* o *and the pinacoid* a *(rim). In this sample, growth sectors associated with the dipyramid* w *are also observed. Immersion, field of view 4.6 × 3.4 mm. Photomicrograph by K. Schmetzer.*
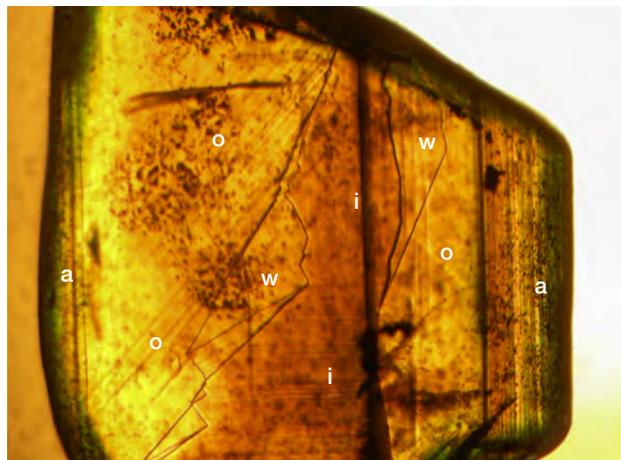
Comparing the different sample groups, boron levels in groups I and II were higher than in groups III and IV. Magnesium was highest in samples of group II, niobium was highest in group IV, and tantalum was highest in groups I and IV. Titanium was elevated in the whitish cores of group III and in samples of group IV, the latter likewise presenting a whitish appearance in reflected light. Iron and gallium showed no significant variation between the four groups.

Color, Pleochroism, and Spectroscopic Properties. In transmitted light, yellow samples from groups I and II and yellow growth zones of chrysoberyls belonging to groups III and IV showed no pleochroism. In contrast, the whitish growth zones seen in groups III and IV (yellowish brown or brown in transmitted light) exhibited a distinct pleochroism, with Y and Z showing light yellowish brown or brown and X displaying intense brown coloration.

The whitish appearance in reflected light was observed in views parallel to the b- and c-axes (or in directions of view between the two axes) but not in a view parallel to the a-axis. Microscopic examination of cabochon-cut samples at high magnification revealed a dense pattern of needle-like inclusions oriented parallel to the a-axis (figure 18). These needles were responsible for the milky appearance and for the bright cat's-eyes seen in cabochon-cut stones.

Absorption spectra were recorded for samples from all four groups. Selected samples are depicted
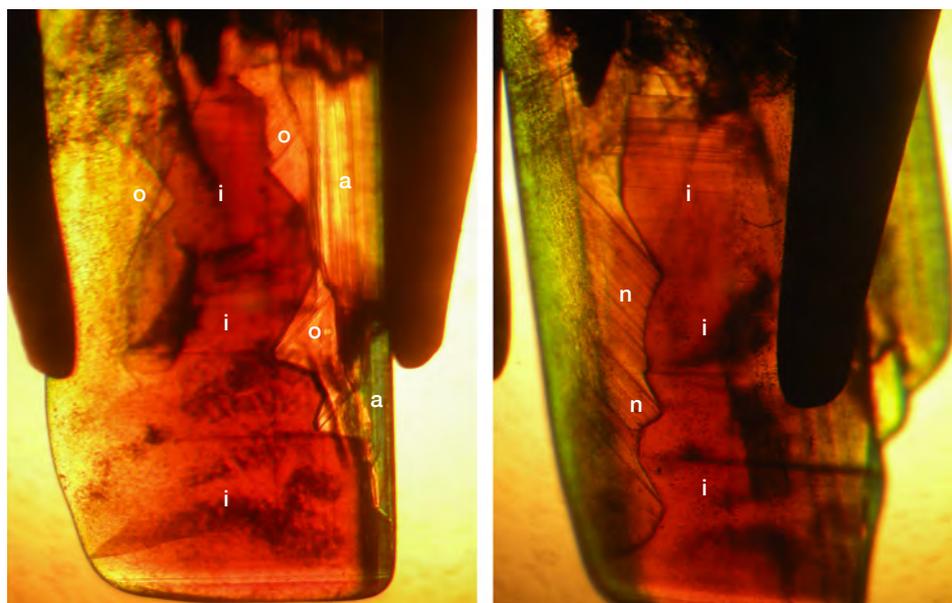
Figure 14. Left: A view of a rough chrysoberyl crystal from group III parallel to the prism i and the dipyramid o shows growth zoning associated with sectorial color zoning parallel to the prism i (core) as well as parallel to the dipyramid o and the pinacoid a (rim). Right: After rotation of the crystal, growth sectors associated with the dipyramid n are also observed. Immersion, field of view 6.0 × 4.6 mm. Photomicrograph by K. Schmetzer.

in figure 19, and the corresponding spectra are displayed in the same figure.

Spectra are presented for two yellow crystals, sample 1 (group I) and sample 3 (group II). The additional spectra provided were derived from zoned samples. Sample 6 (group III) had smaller whitish growth sectors, and sample 8 (group III) had larger whitish zones. Sample 10 (group IV) was primarily whitish with only small yellow growth sectors. As already mentioned, the growth zones appearing whitish in reflected light were yellowish brown or brown in transmitted light (again, see figures 8, 9, and 10).

The spectra of yellow samples from groups I and II (again, see figure 19) showed the commonly observed iron-related absorption spectrum for chrysoberyl, with weak absorption bands or shoulders at about 990, 650, and 500 nm, a strong band at 440 nm, and a strong doublet with maxima at 375 and 365 nm. Samples with yellowish brown to brown *i* growth sectors displayed these iron-related absorption bands, plus an additional absorption in the ultraviolet, extending into the visible range. Stated otherwise, a continuous absorption was present, starting in the red and increasing to the violet end of the visible region and into the ultraviolet range. This additional absorption was responsible for the brownish color component in transmitted light.

DISCUSSION

Chrysoberyl specimens recovered from the secondary sapphire deposits in Australia's New England mining area were characterized by distinct mineralogical and chemical properties. Commonalities and

Figure 15. A series of planes parallel to the dipyramid (114) (represented by a white line) intersects the growth pattern parallel to the faces a, o, w, and i. Color zoning is also observed within the prismatic i growth sectors. View parallel to the prism i and the dipyramid o, immersion, crossed polarizers, field of view 7.6 × 5.7 mm. Photomicrograph by K. Schmetzer.
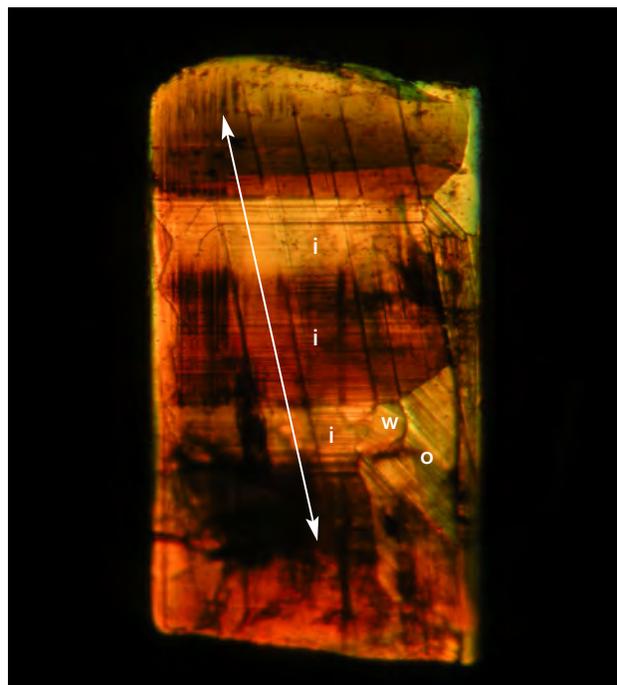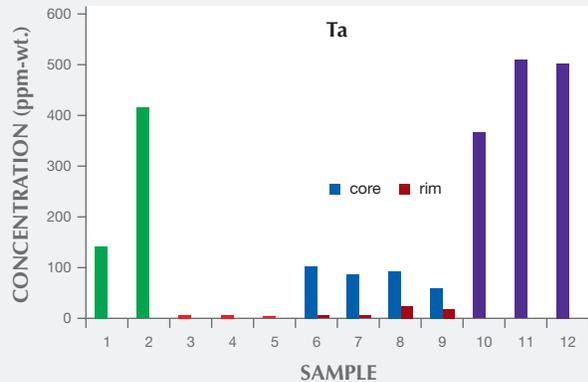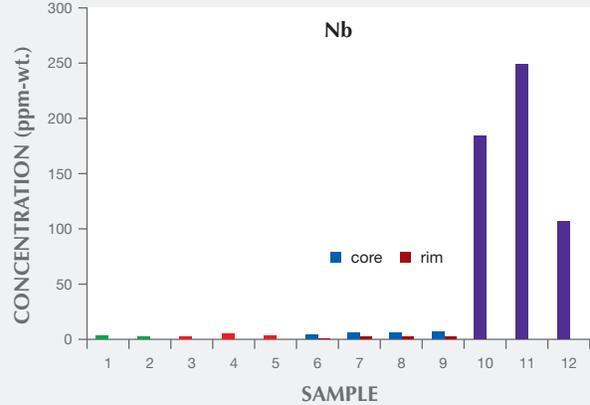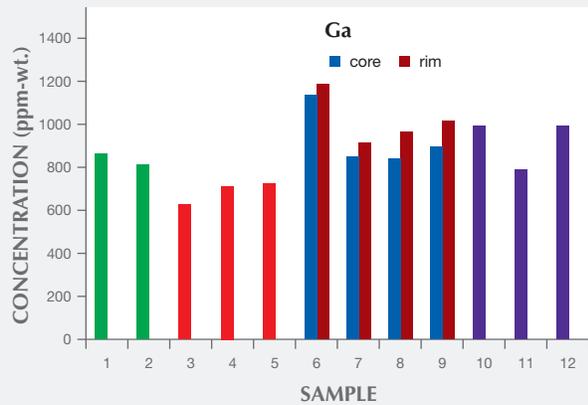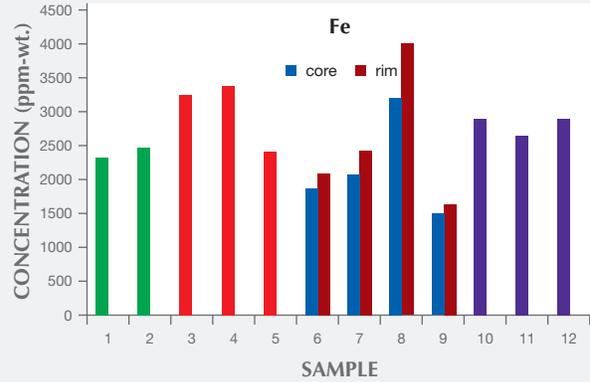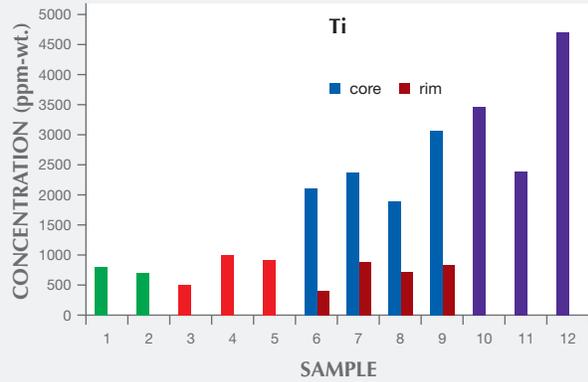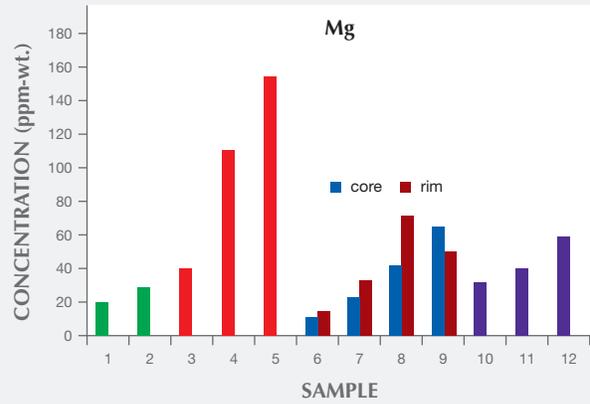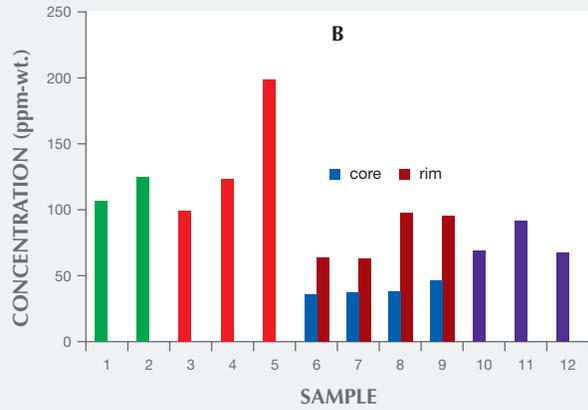
Figure 16. Graphical representation of trace-element contents of chrysoberyl samples from groups I through IV. Boron, magnesium, titanium, niobium, and tantalum show a wide variation, while iron and gallium show a smaller variability. In samples from group III, major differences are measured between core and rim for all elements except iron, with the greatest variation observed for titanium.

TABLE 3. Chemical properties of chrysoberyls from the New England sapphire fields.

Group	I		II			III[a]								IV[b]		
Samples total	4		4			17								9		
Analyzed samples	2		3			4								3		
Sample	1	2	3	4	5	6		7		8		9		10	11	12
Number of analyses, zone	5	5	5	4	4	5 core	4 rim	3 core	6 rim	5 core	5 rim	2 core	10 rim	10	3	5
Elements[c]	Average concentration, in ppmw															
B (5)	107	125	99	123	198	36	64	37	63	38	97	47	95	69	92	67
Mg (3)	20	29	40	110	154	11	15	23	33	42	71	65	50	32	40	59
Ti (15)	794	706	487	1010	909	2112	407	2379	884	1888	714	3067	825	3464	2391	4700
V (3)	bdl	bdl	7	58	51	bdl	4	83	84	17	21	31	26	25	46	44
Cr (10)	bdl	bdl	bdl	35	bdl	bdl	bdl	bdl	bdl	bdl	bdl	bdl	bdl	bdl	bdl	18
Mn (1)	6	4	5	5	4	bdl	bdl	bdl	bdl	3	3	5	bdl	4	3	5
Fe (30)	23,220	24,649	32,378	33,746	24,227	18,710	20,905	20,858	24,322	32,069	40,089	15,029	16,485	29,021	26,500	28,959
Cu (0.8)	bdl	bdl	bdl	bdl	bdl	bdl	bdl	bdl	bdl	1	2	16	26	bdl	bdl	bdl
Ga (1)	863	821	631	715	727	1135	1183	851	912	841	966	897	1015	994	789	993
Zr (0.5)	bdl	bdl	2	3	4	bdl	bdl	bdl	bdl	bdl	bdl	12	bdl	3	7	4
Nb (0.2)	4	2	2	5	4	5	1	7	2	6	3	8	3	184	249	106
In (0.05)	0.2	bdl	bdl	0.3	0.6	0.6	0.2	0.5	bdl	0.6	0.8	0.4	1.2	5	1.8	1.4
Hf (0.2)	bdl	1	bdl	bdl	0.5	bdl	bdl	0.7	bdl	bdl	bdl	bdl	bdl	3	4	2
Ta (0.2)	141	415	7	8	4	103	5	88	6	93	24	60	19	367	509	502
Pb (0.2)	bdl	bdl	0.8	bdl	bdl	bdl	bdl	0.4	3	bdl	1.2	5	bdl	bdl	0.5	bdl

Note: Analytical values for specific elements are only given if all analyses of one sample were above the detection limit. Elements analyzed: Li, Be, B, Na, Mg, Al, Si, P, K, Ca, Sc, Ti, V, Cr, Mn, Fe, Co, Ni, Cu, Zn, Ga, Ge, As, Rb, Sr, Y, Zr, Nb, Mo, Ag, Cd, In, Sb, Cs, Ba, La, Ce, Nd, Sm, Eu, Gd, Tb, Dy, Er, Yb, Lu, Hf, Ta, W, Au, Tl, Pb, Bi, Th, and U; bdl = below detection limit.
[a] Core indicates prismatic i (011) growth zones; rim indicates mainly dipyramidal o (111) and occasionally also pinacoidal a (100) growth zones.
[b] Most analyses represent prismatic i (011) growth zones.
[c] Average minimum detection limits are given in parentheses.

variations among these properties enabled the samples to be summarized and presented according to four groups. These four groups might originate from different mines within the New England placer deposits, but it is also possible that the samples were separated from the sapphires mined commercially within one single area.

The morphology of the crystals, as determined mainly through internal growth structures, was comparable to the features of many chrysoberyls and alexandrites worldwide. Also common were the prismatic or tabular habits of the Australian stones.

Conversely, the most striking feature of the New England chrysoberyls was the strong sectorial zoning observed in a substantial number of the samples. Visual appearance in reflected and transmitted light, spectroscopic properties, and trace-element contents differed for prismatic i growth sectors as compared to the adjacent dipyramidal o growth zones. A pronounced sectorial color zoning between i (core) versus o and a (rim) growth sectors was recently described for alexandrites from Hematita, Brazil (Schmetzer and Hainschwang, 2012), but a pattern similar to the Australian material described here is unknown to the present authors. The series of structural planes intersecting the commonly observed growth pattern might represent glide planes that were caused by extremely high pressure during or after crystal growth.
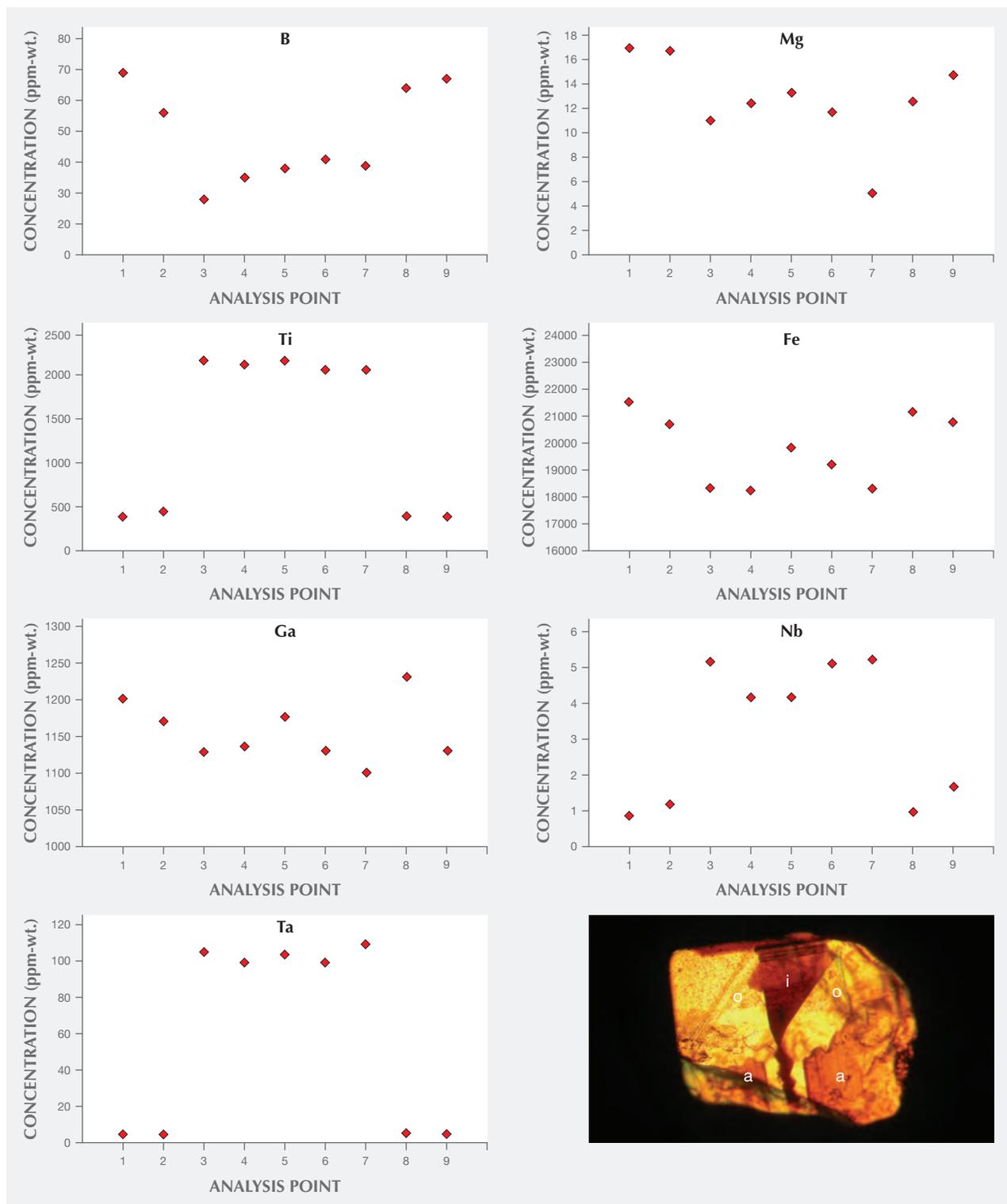
Figure 17. Graphical representation of trace-element contents in a chrysoberyl crystal from group III. Two analysis points are located left of the center within an o growth zone, two analysis points are located right of the center within another o growth zone, and the central i growth sector is represented by five analysis points. In the traverse across the two o (rim) and the i (core) growth sectors, boron, magnesium, titanium, niobium, and tantalum show a wide variation, while iron and gallium show only a smaller variability. The sample showing sectorial color zoning is depicted at the lower right.

Regarding chemical composition, the analytical technique used measured the bulk composition of the chrysoberyl host together with any minute inclusions present in specific areas with a diameter of approximately 50 µm (see figure 18). For the zoned crystals of group III, the greatest compositional contrast between the cores and the rims was the elevated titanium contents within the *i* growth sectors of the cores. Similarly high concentrations of titanium were also observed in samples of group IV, which were comprised primarily of *i* growth zones. These high titanium levels might correlate with minute needle-like inclusions. These tiny needles were responsible for the whitish appearance of the growth sectors in reflected light and caused chatoyancy in the cabochon-cut samples. The inclusions producing chatoyancy are normally described as rutile precipitates or extremely thin channels, but there exists no detailed study (e.g., by transmission electron microscopy) of this phenomenon in natural chatoyant chrysoberyl. In synthetic alexandrite, chatoyancy is produced by doping the melt with titanium oxide during crystal growth, followed by exsolution of needle-like precipitates through subsequent heat treatment of the as-grown crystals (Schmetzer et al., 2013b).

The yellow color apparent in many of the Australian samples studied here was related to minor amounts of iron, as confirmed by trace-element composition and spectroscopic data. The absorption spectra recorded were consistent with the literature

Figure 18. Extremely fine needle-like particles running parallel to the a-axis in a chrysoberyl cat's-eye are responsible for chatoyancy. Oil immersion, reflected light, field of view 75 × 56 µm. Photomicrograph by H.-J. Bernhardt.

(Farrell and Newnham, 1965; Pfenninger, 2000; Lottermoser et al., 2011). Iron is predominantly found as Fe^{3+} replacing Al^{3+} in both octahedrally coordinated sites of the chrysoberyl structure, but a small fraction of iron is also found occasionally in the bivalent state (Weber et al., 2007; Lottermoser et al., 2011).

The slightly greenish hue of some yellow samples might be due to the small traces of vanadium that were detected in various New England stones (see table 3). The influence of such small amounts of vanadium and/or chromium has been described recently for slightly greenish yellow chrysoberyls from Madagascar and Sri Lanka (Witthayarat and Thanasuthipitak, 2014).

The iron levels measured for both the cores and the rims of group III chrysoberyls as well as for the remaining samples of other groups were all in a comparable range (figures 16 and 17, table 3). Thus, different iron concentrations alone cannot be responsible for the color variation between yellow and brown samples or for the sectorial color zoning between cores and rims of group III stones. The distinct pleochroism within the brown sectors of groups III and IV suggests that an electron charge-transfer mechanism may cause the increasing absorption from red to violet in the visible range. A definitive answer, however, would require more extensive analysis, and an assignment of this particular absorption to Fe^{2+}-Fe^{3+} or Fe^{2+}-Ti^{4+} pairs is not possible at present.

Tin and gallium have long been recognized as trace elements in chrysoberyls and alexandrites from a variety of locations (Ottemann, 1965; Ottemann et al., 1978), and multiple trace elements in alexandrites have been used in recent studies to assist in origin determination (Malsy, 2010; Schmetzer and Malsy, 2011; Schmetzer et al., 2011). In these latter studies, a number of trace elements such as boron, magnesium, gallium, germanium, tin, and tantalum were considered, along with the main color-causing transition metals vanadium, chromium, and iron. The trace elements determined by LA-ICP-MS showed a wide compositional range for samples from Russia, Brazil, India, Sri Lanka, Tanzania, and Zimbabwe. Ternary diagrams prepared from the data then enabled separation between various localities.

Niobium and tantalum have been reported as trace elements in volcanic sapphires from placer deposits in Australia, including those of the New England gem fields, but also from basalt-related placer deposits in other countries such as Thailand, Laos, Cambodia, China, Nigeria, Madagascar, and Scot-

ABSORPTION SPECTRA
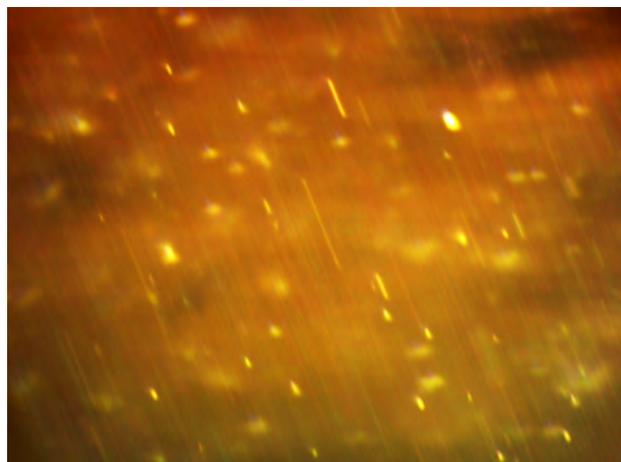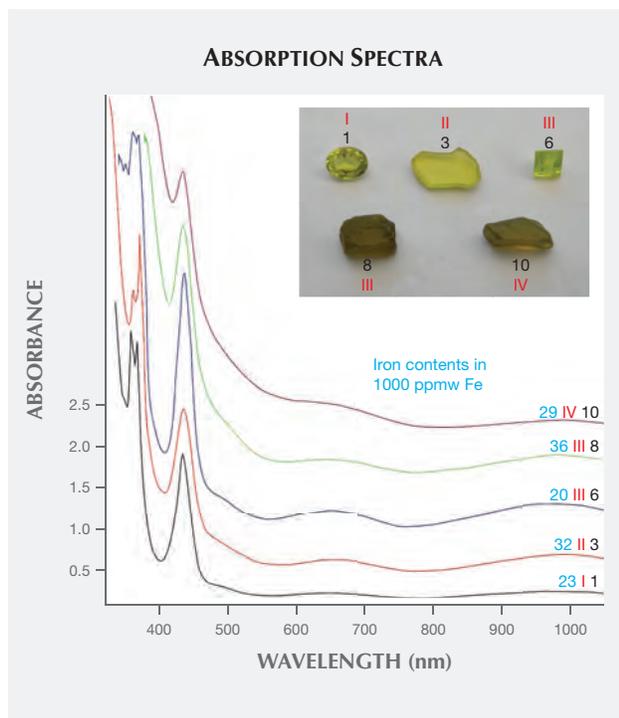
Figure 19. Absorption spectra of five chrysoberyls (samples 1, 3, 6, 8, and 10) representing samples from groups I through IV (indicated in red). The Arabic sample numbers (in black) correlate with the analyses given in table 3, and the samples are depicted in the insert. Average iron contents are given in blue (in 1000 ppmw Fe). All spectra reveal absorption bands assigned to trivalent iron; the spectra of the yellowish brown to brown samples 8 and 10 from groups III and IV present an additional absorption with a continuous increase from the red to the violet part of the visible range. The spectra of samples 3, 6, 8, and 10 were shifted vertically for clarity. The faceted yellow sample 1 measures 5.8 × 4.4 mm and weighs 0.53 ct. Inset photo by K. Schmetzer.

land. Nb or Ta contents are frequently at low levels, with ranges below 50 ppm, but concentrations of up to several hundred or several thousand ppm have been reported for sapphires from specific occurrences (e.g., the Weldborough area in Tasmania). The Nb and Ta contents measured in the corundum derive from various mineral inclusions, especially columbite, pyrochlore, ilmenorutile, and brookite. The sizes reported for such inclusions vary from the millimeter range down to the micron range, and some inclusions are even described as submicroscopic—i.e., near or below 1 μm in size (Coenraads, 1991; Guo et al., 1996; Sutherland et al., 1998, 2002, 2009; Saminpanya et al., 2003; Wathanakul et al.,

2004; McGee, 2005; Abduriyim and Kitawaki, 2006; Zaw et al., 2006; Graham et al., 2008; Sutherland and Abduriyim, 2009; Upton et al., 2009; Pardieu, 2013).

Compared to the data published for volcanic sapphires in these prior works, however, some of the present chrysoberyl samples, while recovered from placer deposits related to Tertiary volcanics and unearthed together with basaltic sapphires, showed extremely elevated levels of niobium (group IV crystals) and tantalum (group I samples, cores in group III, and group IV chrysoberyls). Similarly high tantalum contents of up to 1364 ppm Ta were reported for Russian alexandrites but were not linked to any particular mineral inclusion (Malsy, 2010).

In considering the potential relationship of such elevated niobium and tantalum levels to the inclusion scene of the Australian stones here, many of the yellow samples from groups I and II as well as the yellow growth zones for groups III and IV did not show any inclusions in the immersion microscope. At high magnification, one chrysoberyl with a whitish area showed the small needle-like particles that were responsible for chatoyancy in cabochon-cut samples, but such inclusions have typically been described as rutile. Thus, further studies would be necessary to determine the mineral species present as inclusions and from which the elevated Nb and Ta could derive.

Recently, trace-element contents of corundum, chrysoberyl, and zircon grains recovered from the Mamfe placer deposit in southwest Cameroon were described (Kanouo et al., 2016). It was concluded that most of the blue, yellow, or grayish green corundum samples found in the Mamfe gem placer deposit were of magmatic origin and that the chrysoberyls were formed in granitic pegmatites; in other words, the sapphire and chrysoberyl grains originated from different host rocks. With respect to the chrysoberyls in particular, it was assumed that they had originated from two different granitic pegmatites; this conclusion was derived from analyses of four grains, on the basis primarily of variable trace-element ranges of tin, titanium, tantalum, niobium, and zirconium.

Regarding formation of the present four groups of chrysoberyl samples recovered from placer deposits in New South Wales, together with sapphires related to Tertiary volcanics (most likely volcaniclastic rocks), it is necessary to consider that granites and pegmatites are also located in the area (see, e.g., Audétat et al., 2000; Pettke et al., 2005; Schaltegger et al., 2005; Brown, 2006). How-

ever, chrysoberyls from these large granitic bodies are—to our knowledge—not mentioned in the literature, and therefore no direct comparison with such material is possible.

Thus, one of the following scenarios could explain each of the four groups:

1. The chrysoberyls were formed in granitic pegmatites and subsequently accumulated at the placers without transport by or interaction with the volcanic rocks that carried the sapphires to the surface.

2. The chrysoberyls and sapphires were accumulated from different host rocks in the earth's crust and transported by volcanic activity together to the surface.

It is, of course, possible that the same underlying scenario does not apply to each of the groups of chrysoberyl samples described in this study. This could also be the reason for the widely ranging trace-element levels found in samples from the various groups. Conclusive data to decide between these possibilities, as worked out for corundum within the last two decades using trace-element contents, are not available for chrysoberyl.

CONCLUSIONS

The chrysoberyl crystals recovered together with sapphires related to Tertiary volcanics in the New England placer deposits were—according to highly variable chemical and mineralogical properties—subdivided into four groups. These groups might have originated, at least in part, from different host rocks. A possible transportation of the chrysoberyls together with sapphires to the surface by volcanic activity needs further study.

Samples from the largest of the four groups displayed a sectorial color zoning that is unique among chrysoberyl samples studied to date. The sectorial color zoning was seen in conjunction with variable trace-element contents between different growth sectors of the so-called core and rim, related mainly to prismatic i (011) or dipyramidal o (111) growth zones. Acicular inclusions producing chatoyancy in cabochon-cut samples were seen only in the cores. Compared to yellow samples or yellow growth sectors of zoned samples, only brown samples or brown growth sectors showed pleochroism. This latter feature, in addition to spectroscopic properties, indicated the presence of an additional cause for the brown color, beyond the trivalent iron responsible for the yellow color in the zoned chrysoberyls.

REFERENCES

Abduriyim A., Kitawaki H. (2006) Determination of the origin of blue sapphire using laser ablation inductively coupled plasma mass spectrometry (LA-ICP-MS). *Journal of Gemmology*, Vol. 30, No. 1/2, pp. 23–36.

Abduriyim A., Sutherland F.L., Belousova E.A. (2012a) U-Pb age and origin of gem zircon from the New England sapphire fields, New South Wales, Australia. *Australian Journal of Earth Sciences*, Vol. 59, pp. 1067–1081.

Abduriyim A., Sutherland F.L., Coldham T. (2012b) Past, present and future of Australian gem corundum. *Australian Gemmologist*, Vol. 24, No. 10, pp. 234–242.

Audétat A., Günther D., Heinrich C.A. (2000) Magmatic-hydrothermal evolution in a fractionating granite: A microchemical study of the Sn-W-F-mineralized mole granite (Australia). *Geochimica et Cosmochimica Acta*, Vol. 64, No. 19, pp. 3373–3393, http://dx.doi.org/10.1016/S0016-7037(00)00428-2

Barton M.D., Young S. (2002) Non-pegmatitic deposits of beryl-lium: mineralogy, geology, phase equilibria and origin. In E.S. Grew, Ed., *Beryllium: Mineralogy, Petrology, and Geochemistry*. Reviews in Mineralogy, 50, pp. 591–691.

Beurlen H., Thomas R., Melgarejo J.C., Da Silva J.M.R., Rhede D., Soares D.R., Da Silva M.R.R. (2013) Chrysoberyl-sillimanite association from the Roncadeira pegmatite, Borborema Province, Brazil: Implications for gemstone exploration. *Journal of Geosciences*, Vol. 58, No. 2, pp. 79–90, http://dx.doi.org/10.3190/jgeosci.142.

Bottrill R.S. (1996) Corundum and sapphire in Tasmania. *Tasmanian Geological Survey Record*, 1996/05, pp. 1–10.

Brightman R. (1984) Chrysoberyl from Anakie, Queensland. *Australian Gemmologist*, Vol. 15, No. 7, pp. 241–242.

Brown R.E. (2006) Inverell exploration NSW geophysics—new data for exploration and geological investigations in the northern New England area of New South Wales. *Quarterly Notes, Geological Survey of New South Wales*, No. 121, pp. 1–38.

Cassedanne J., Roditi M. (1993) The location, geology, mineralogy and gem deposits of alexandrite, cat's-eye and chrysoberyl in Brazil. *Journal of Gemmology*, Vol. 23, No. 6, pp. 333–354.

Černý P. (2002) Mineralogy of beryllium in granitic pegmatites. In E.S. Grew, Ed., *Beryllium: Mineralogy, Petrology, and Geochemistry*. Reviews in Mineralogy, 50, pp. 405–444.

Coenraads R.R. (1990) Key areas for alluvial diamond and sapphire exploration in the New England gem fields, New South Wales, Australia. *Economic Geology*, Vol. 85, No. 6, pp. 1186–1207, http://dx.doi.org/gsecongeo.85.6.1186

——— (1991) Alluvial sapphires and diamonds of the New England gem fields, New South Wales, Australia. Thesis, School of Earth Sciences, Macquarie University, 275 pp.

——— (1994) Evaluation of potential sapphire source rocks within the catchments of Kings Plains Creek and Swan Brook, near Inverell, New South Wales. *Records of the Australian Museum*, Vol. 46, pp. 5–24.

——— (1995) Gemstones of New South Wales. *Australian Gemmologist*, Vol. 19, No. 3, pp. 91–105.

Coldham T.S. (2014) Tom Nunan—sapphire miner extraordinaire 1928-2013. *Australian Gemmologist*, Vol. 25, No. 5, pp. 180–191.

Dissanayake C.B., Chandrajith R., Tobschall H.J. (2000) The geology, mineralogy and rare element geochemistry of the gem deposits of Sri Lanka. *Bulletin of the Geological Society of Finland*, Vol. 72, Parts 1–2, pp. 5–20.

Facer R., Stewart R. (1995) *Sapphires in New South Wales*. NSW Department of Mineral Resources, Sydney, p. 9.

Farrell E.F., Newnham R.E. (1965) Crystal-field spectra of chrysoberyl, alexandrite, peridot, and sinhalite. *American Mineralogist*, Vol. 50, No. 11–12, pp. 1972–1981.

Franz G., Morteani G. (2002) Be-minerals: Synthesis, stability, and occurrence in metamorphic rocks. In E.S. Grew, Ed., *Beryllium: Mineralogy, Petrology, and Geochemistry*. Reviews in Mineralogy, 50, pp. 551–589.

Graham I., Sutherland L.F., Zaw K., Nechaev V., Khanchuk A. (2008) Advances in our understanding of the gem corundum deposits of the West Pacific continental margins intraplate basaltic fields. *Ore Geology Reviews*, Vol. 34, No. 1–2, pp. 200–215, http://dx.doi.org/10.1016/j.oregeorev.2008.04.006

Gunaratne H.S., Dissanayake C.B. (1995) *Gems and Gem Deposits of Sri Lanka*. The National Gem and Jewellery Authority of Sri Lanka, Colombo, Sri Lanka, 120 pp.

Guo J., O'Reilly S.Y., Griffin W.L. (1996) Corundum from basaltic terrains: A mineral inclusion approach to the enigma. *Contributions to Mineralogy and Petrology*, Vol. 122, No. 4, pp. 368–386, http://dx.doi.org/10.1007/s004100050134

Henn U., Milisenda C.C. (1997) Neue Edelsteinvorkommen in Tansania: Die Region Tunduru-Songea. *Zeitschrift der Deutschen Gemmologischen Gesellschaft*, Vol. 46, No. 1, pp. 29–43 [in German].

Kanouo N.S., Ekomane E., Yongue R.F., Njonfang E., Zaw K., Changqian M., Ghogomu T.R., Lentz D.R., Venkatesh A.S. (2016) Trace elements in corundum, chrysoberyl, and zircon: Application to mineral exploration and provenance study of the western Mamfe gem clastic deposits (SW Cameroon, Central Africa). *Journal of African Earth Sciences*, Vol. 113, pp. 35–50, http://dx.doi.org/10.1016/j.jafrearsci.2015.09.023

Liversidge A. (1876) *The Minerals of New South Wales*. 1st ed., Sydney, Thomas Richards, Government Printer, pp. 48–50.

——— (1888) *The Minerals of New South Wales*, 3rd ed. London, Trübner and Co., pp. 196–197.

Lottermoser W., Redhammer G.J., Weber S.-U., Litterst F.J., Tippelt G., Dlugosz S., Bank H., Amthauer G., Grodzicki M. (2011) The electric field gradient in natural iron-doped chrysoberyl Al_2BeO_4 and sinhalite $MgAlBO_4$ single crystals. *Physics and Chemistry of Minerals*, Vol. 38, No. 10, pp. 787–799 http://dx.doi.org/10.1007/s00269-011-0451-2

Malsy A.-K. (2010) Trace element chemistry and locality determination. In K. Schmetzer, Ed., *Russian Alexandrites*. Schweizerbart Science Publishers, Stuttgart, Germany, pp. 121–126.

Manimaran G., Bagai D., Chacko P.T.R. (2007) Chrysoberyl from Southern Tamil Nadu of South India, with implications for Gondwana studies. In S. Rajendran, S. Aravindan, K. Srinivasamoorthy, Eds., *Mineral Exploration: Recent Strategies*. New India Publishing Agency, New Delhi, pp. 63–76.

McGee B.M. (2005) Characteristics and origin of the Weldborough sapphire, NE Tasmania. Thesis, University of Tasmania.

Menon R.D., Santosh M., Yoshida M. (1994) Gemstone mineralization in Southern Kerala, India. *Journal of the Geological Society of India*, Vol. 44, pp. 241–252.

Milisenda C.C., Henn U., Henn J. (2001) New gemstone occurrences in the south-west of Madagascar. *Journal of Gemmology*, Vol. 27, No. 7, pp. 385–394.

Okrusch M. (1971) Zur Genese der Chrysoberyll- und Alexandritlagerstätten. Eine Literaturübersicht. *Zeitschrift der Deutschen Gemmologischen Gesellschaft*, Vol. 20, No. 3, pp. 114–124 [in German].

Ottemann J. (1965) Gallium und Zinn in Alexandrit. *Neues Jahrbuch für Mineralogie Monatshefte*, Vol. 1965, No. 2, pp. 31–42 [in German].

Ottemann J., Schmetzer K., Bank H. (1978) Neue Daten zur Anreicherung des Elements Gallium in Alexandriten. *Neues Jahrbuch für Mineralogie Monatshefte*, Vol. 1978, No. 4, pp. 172–175 [in German].

Pardieu V. (2013) Blue sapphires and beryllium: 'An unfinished world quest'. *InColor*, No. 23, Summer, pp. 36–43.

Pedrosa-Soares A., Chaves M., Scholz R. (2009) Field trip guide. Eastern Brazilian pegmatite province. *PEG 2009—4th International Symposium on Granitic Pegmatites*, Recife, Brazil, 28 pp.

Pettke T., Audétat A., Schaltegger U., Heinrich C.A. (2005) Magmatic-to-hydrothermal crystallization in the W-Sn mineralized Mole granite (NSW, Australia). Part II: Evolving zircon and thorite trace element chemistry. *Chemical Geology*, Vol. 220, No. 3–4, pp. 191–213, http://dx.doi.org/10.1016/j.chemgeo.2005.02017

Pfenninger S. (2000) Mineralogische und Gemmologische Untersuchungen an Chrysoberyllen aus Tunduru (Tansania). Diplomarbeit, Universität Basel, 82 pp. (unpublished) [in German].

Proctor K. (1988) Chrysoberyl and alexandrite from the pegmatite districts of Minas Gerais, Brazil. *G&G*, Vol. 24, No. 1, pp. 16–32, http://dx.doi.org/10.5741/GEMS.24.1.16

Saminpanya S., Manning D.A.C., Droop G.T.R., Henderson C.M.B. (2003) Trace elements in Thai gem corundums. *Journal of Gemmology*, Vol. 28, No. 7, pp. 399–415.

Schaltegger U., Pettke T., Audétat A., Reusser E., Heinrich C.A. (2005) Magmatic-to-hydrothermal crystallization in the W-Sn mineralized Mole granite (NSW, Australia). Part I: Crystallization of zircon and REE-phosphates over three million years—a geochemical and U-Pb geochronological study. *Chemical*

Geology, Vol. 220, No. 3–4, pp. 215–235, http://dx.doi.org/10.1016/j.chemgeo.2005.02.018

Schmetzer K. (2011) Measurement and interpretation of growth patterns in chrysoberyl, including alexandrite. *Journal of Gemmology*, Vol. 32, No. 5–8, pp. 129–144.

Schmetzer K., Hainschwang T. (2012) Origin determination of alexandrite—a practical example. *InColor*, No. 21, Fall/Winter, pp. 36–39.

Schmetzer K., Malsy A.-K. (2011) Alexandrite and colour-change chrysoberyl from the Lake Manyara alexandrite-emerald deposit in northern Tanzania. *Journal of Gemmology*, Vol. 32, No. 5–8, pp. 179–209.

Schmetzer K., Stocklmayer S., Stocklmayer V., Malsy A.-K. (2011) Alexandrites from the Novello alexandrite-emerald deposit, Masvingo District, Zimbabwe. *Australian Gemmologist*, Vol. 24, No. 6, pp. 133–147.

Schmetzer K., Bernhardt H.-J., Balmer W.A., Hainschwang T. (2013a) Synthetic alexandrites grown by the HOC method in Russia: Internal features related to the growth technique and colorimetric investigation. *Journal of Gemmology*, Vol. 33, No. 5–6, pp. 113–129.

Schmetzer K., Bernhardt H.-J., Hainschwang T. (2013b) Titanium-bearing synthetic alexandrite and chrysoberyl. *Journal of Gemmology*, Vol. 33, No. 5–6, pp. 137–148.

Soman K., Druzhinin A.V. (1987) Petrology and geochemistry of chrysoberyl pegmatites of south Kerala, India. *Neues Jahrbuch für Mineralogie Abhandlungen*, Vol. 157, No. 2, pp. 167–183.

Sutherland F.L., Abduriyim A. (2009) Geographic typing of gem corundum: a test case from Australia. *Journal of Gemmology*, Vol. 31, No. 5–8, pp. 203–210.

Sutherland F.L., Hoskin P.W.O., Fanning C.M., Coenraads R.R. (1998) Models of corundum origin from alkali basaltic terrains: A reappraisal. *Contributions to Mineralogy and Petrology*, Vol. 133, No. 4, pp. 356–372, http://dx.doi.org/10.1007/s004100050458

Sutherland F.L., Graham I.T., Pogson R.E., Schwarz D., Webb G.B.,

Coenraads R.R., Fanning C.M., Hollis J.D., Allen T.C. (2002) The Tumbarumba basaltic gem field, New South Wales: In relation to sapphire-ruby deposits of Eastern Australia. *Records of the Australian Museum*, Vol. 54, pp. 215–248.

Sutherland F.L., Zaw K., Meffre S., Giuliani G., Fallick A.E., Graham I.T., Webb G.B. (2009) Gem-corundum megacrysts from east Australian basalt fields: Trace elements, oxygen isotopes and origins. *Australian Journal of Earth Sciences*, Vol. 56, No. 7, pp. 1003–1022, http://dx.doi.org/10.1080/08120090903112109

Sweeney B. (1995) Gemstones of Tasmania. *Australian Gemmologist*, Vol. 19, No. 3, pp. 149–154.

Upton B.G.J., Finch A.A., Slaby E. (2009) Megacrysts and salic xenoliths in Scottish alkali basalts: Derivatives of deep crustal intrusions and small-melt fractions from the upper mantle. *Mineralogical Magazine*, Vol. 73, No. 6, pp. 895–908, http://dx.doi.org/10.1180/minmag.2009.073.6.943

Wathanakul P., Atichat W., Pisutha-Arnond V., Singbamroong S. (2004) Evidence on the unusually high Be, Sn, Nb, and Ta content in some trapiche-like sapphires from basaltic origins. *Proceedings, 29th International Gemmological Conference*, Wuhan, China, pp. 114–118.

Weber S.-U., Grodzicki M., Lottermoser W., Redhammer G.J., Tippelt G., Ponahlo J., Amthauer G. (2007) [57]Fe Mössbauer spectroscopy, X-ray single-crystal diffractometry, and electronic structure calculations on natural alexandrite. *Physics and Chemistry of Minerals*, Vol. 34, No. 7, pp. 507–515, http://dx.doi.org/10.1007/s00269-007-0166-6

Witthayarat J., Thanasuthipitak P. (2014) Crystal chemistry of coloration in chrysoberyl. *Proceedings, 4th International Gem and Jewelry Conference*, Chiang Mai, Thailand, pp. 185–187.

Zaw K., Sutherland F.L., Dellapasqua F., Ryan C.G., Yui T.-F., Mernagh T.P., Duncan D. (2006) Contrasts in gem corundum characteristics, eastern Australian basaltic fields: trace elements, fluid/melt inclusions and oxygen isotopes. *Mineralogical Magazine*, Vol. 70, No. 6, pp. 669–687, http://dx.doi.org/10.1180/0026461067060356

The
Dr. Edward J. Gübelin
Most Valuable Article
AWARD

First Place

VANADIUM AND CHROMIUM-BEARING PINK PYROPE GARNET: CHARACTERIZATION AND QUANTITATIVE COLORIMETRIC ANALYSIS
WINTER 2015
Ziyin Sun, Aaron C. Palke, and Nathan Renfro

Ziyin Sun is a staff gemologist in the gem identification department at GIA in Carlsbad, California. Mr. Sun obtained a bachelor's degree in chemistry and a master's degree in analytical chemistry from Nanjing University in China. **Aaron C. Palke** is a postdoctoral research associate at GIA in Carlsbad. Dr. Palke received his PhD in geology from Stanford University. **Nathan Renfro** is the analytical manager of the gem identification department and analytical microscopist in the inclusion research department at GIA in Carlsbad. Mr. Renfro holds a bachelor's degree in geology from Appalachian State University in Boone, North Carolina.

Ziyin Sun   Aaron C. Palke   Nathan Renfro

Second Place

THE CHINESE SOUL IN CONTEMPORARY JEWELRY DESIGN
SPRING 2015
Andrew Lucas, Merilee Chapin, Moqing Lin, and Xiaodan Jia

Andrew Lucas is a field gemologist in GIA's content strategy department in Carlsbad, California. Mr. Lucas researches and documents the entire mine-to-market gem and jewelry industry for GIA education; he also presents seminars on colored stones and diamonds. **Merilee Chapin** is the managing editor in GIA's content strategy department. She is a graduate of the University of California, San Diego, and a member of the Phi Beta Kappa Society. **Moqing Lin** and **Xiaodan Jia** (not pictured) are gemologists in GIA's Hong Kong laboratory.

Andrew Lucas   Merilee Chapin

Third Place

SPLENDOR IN THE OUTBACK: A VISIT TO AUSTRALIA'S OPAL FIELDS
WINTER 2015
Tao Hsu, Andrew Lucas, and, Vincent Pardieu

Andrew Lucas was profiled in the second-place entry. **Tao Hsu** is the technical editor of *Gems & Gemology* and a contributor to the Research and News section of GIA's website. Dr. Hsu received her doctorate in geology from the University of Southern California. **Vincent Pardieu** is senior manager of field gemology at GIA in Bangkok. Mr. Pardieu has led 76 successful field expeditions to gemstone mining areas to collect samples for the GIA reference collection.

Tao Hsu   Vincent Pardieu

Thank you to all the readers who voted. In addition to our winning authors, we congratulate Nicolas Francfort of Geneva, whose name was randomly drawn from the entries to win a one-year subscription to *G&G*.

GEM-QUALITY SERPENTINE FROM VAL MALENCO, CENTRAL ALPS, ITALY

Ilaria Adamo, Valeria Diella, Rosangela Bocchio, Caterina Rinaudo, and Nicoletta Marinoni

Pizzo Tremogge in Val Malenco, Italy, is a source of gem-quality serpentine. Samples from this mountain locality were investigated by standard gemological and petrological methods, Raman spectroscopy, and electron microprobe analysis. The rough and polished specimens were massive aggregates, with a green to yellow color and white, gray, and black veins or spots. From a mineralogical standpoint, this material consists of all three phases of serpentine-group minerals (lizardite, antigorite, and chrysotile) alternating with other minerals such as carbonate (calcite and dolomite), quartz, chlorite, and brucite. The quantity of carved and polished material to date is small, but the latest geological prospecting indicates the outcrop's strong potential.

Serpentine-group minerals are common rock-forming hydrous phyllosilicates, with an ideal chemical formula of $Mg_3Si_2O_5(OH)_4$. Each of the three main serpentine polymorphs (chrysotile, lizardite, and antigorite) forms under a wide range of thermic conditions in many geologic settings (Evans et al., 2013). *Serpentinite*[1], which consists mostly of serpentine-group minerals, has been used since antiquity for ceremonial and ornamental carvings (Guillot and Hattori, 2013). Gem-quality serpentine, often referred to as "noble" serpentine, is characterized by a compact microstructure and fine colors, such as blue-green, yellowish green, gray, and white (O'Donoghue, 2006). The material is sometimes used as an imitation of jadeite and nephrite because of its similar aggregate structure and color appearance, and it is often marketed as "serpentine jade" (Kim et al., 2006; Lin et al., 2012). A rare chatoyant variety of serpentine was also reported by Choudhary (2009).

Val Malenco (or Malenco Valley) in the Central Alps of Italy, famous for gem-quality demantoid, nephrite, and rhodonite (Adamo et al., 2009; Adamo and Bocchio, 2013; Diella et al., 2014), is also a source of gem-quality serpentine (figure 1). In particular, one of Val Malenco's best-known sources for serpentine is Pizzo Tremogge (or Tremogge Peak) (figure 2, left). As seen in figure 2, right, serpentine is included in forsterite olivine-bearing marbles from the Paleozoic era (Bedognè et al., 1993).

Gem-quality serpentine from Pizzo Tremogge was discovered by mineral collector Pietro Sigismund, who reported the find in the 1930s (Gramaccioli, 1962). Production and marketing of the material started around the year 2000 (P. Nana, pers. comm., 2015). The serpentine layers (figure 3), located 2800 m above sea level, are discontinuous (up to 300–350 m in length and 40 m in thickness), and mining is limited by difficult access. Although the outlook for future production is uncertain, reserves at deeper layers may be inferred.

Serpentine from Pizzo Tremogge was traditionally identified as lizardite, although a full mineralogical investigation of this material has yet to be conducted. Recent preliminary data by Adamo et al. (2014) proved that antigorite and chrysotile also occur together with lizardite. Therefore, it seems useful to provide a further detailed characterization of the serpentine from

[1]*Serpentinite*: Rock consisting largely of serpentine-group minerals formed by "serpentinization," a process consisting of a hydration and metamorphic transformation of oceanic crustal and upper mantle material.

Figure 1. Serpentine from Pizzo Tremogge in Val Malenco, Italy. Left: A bead necklace rests on a 15 cm long ornamental polished slab. The necklace is accompanied by a cat statuette measuring about 4 cm high and two pendants approximately 3.5–4 cm in length. The necklace on the right consists of spherical beads ranging in diameter from 1.0 to 2.0 cm. Photos by Pietro Nana.

Pizzo Tremogge, focusing on its use as a gem material. We investigated a suite of rough and cut samples provided by Mr. Pietro Nana (Sondrio, Italy), using gemological characterization, electron microprobe chemical analyses, and Raman spectroscopy. The latter is a reliable and nondestructive method for identifying the three serpentine minerals (Rinaudo et al., 2003).

BACKGROUND INFORMATION

Serpentine-group minerals include lizardite, chrysotile, and antigorite, which are polymorphs of the Mg-rich hydrous phyllosilicate with the approximate chemical formula $Mg_3Si_2O_5(OH)_4$. To some extent, Fe, Al, and Ni may be substituted for antigorite, and Al for Si (Deer et al., 2009). The basic structural unit

Figure 2. Left: A view of Pizzo Tremogge in Val Malenco, Italy. Photo by Pietro Nana. Right: A sketch map of the Pizzo Tremogge area, showing (1) clinothulite outcrop (in dark brown), (2) "noble" serpentine layers (in light brown), (3) marbles with olivine (forsterite), and (4) marbles with intercalations of "noble" serpentine. Modified from Gramaccioli (1962).
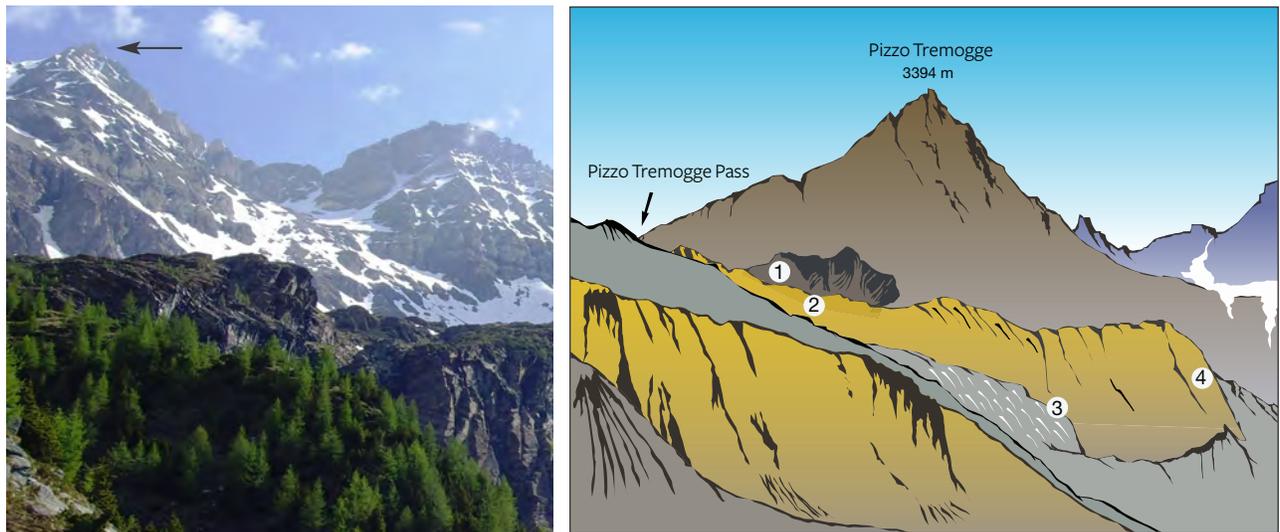
Figure 3. The serpentine layers intercalated with marble at Pizzo Tremogge. Photo by Pietro Nana.

consists of an Mg-rich sheet, linked on one side to a single tetrahedral silicate sheet, with hydrogen bonding between the layers (Evans et al., 2013). Lizardite, chrysotile, and antigorite are distinguished by their crystal microstructure, consisting of different arrangements of the layers. Lizardite and chrysotile are characterized by a flat and a curved/cylindrical crystal microstructure, respectively, while antigorite dis-

<div style="border:1px solid; padding:8px;">

In Brief

- Gem serpentine is a massive aggregate of hydrous magnesium silicate crystals.
- Serpentine from Pizzo Tremogge, in Val Malenco of the Italian Central Alps, has been known since the 1930s but was not marketed until about 2000.
- Samples from this locality consist of all three phases of serpentine-group minerals, alternating with other mineral phases.

</div>

plays wavy layers resulting in a corrugated microstructure (Evans et al., 2013). Serpentine minerals form by the hydration of olivine-rich ultramafic rocks at relatively low temperature; this is the serpentinization process. The three serpentine-group minerals have different stability fields (Deer et al.,

2009). In particular, lizardite is the first phase that commonly pseudomorphs after olivine; chrysotile occurs mainly as a filling in the fractures that cross-cut serpentinite rocks, whereas antigorite is considered the high-temperature phase, growing from lizardite and chrysotile with increasing grade of metamorphism at temperatures above about 320°C (Evans et al., 2013). Chrysotile is also the main constituent of commercial asbestos, which was used extensively for thermal and electric insulation until the discovery that its fine dust is harmful to human health (Fubini and Fenoglio, 2007).

GEOLOGICAL SETTING

Val Malenco is located at the border of southeastern Switzerland and northern Italy, between the Penninic and the Austroalpine domains of the Alps (Müntener et al., 2000). The regional geology appears complex due to extensive tectonic disruption associated with a stack of Alpine nappes (Penninic and Austroalpine nappe system). Three major structural complexes, shown in figure 4 from east to west, characterize this area:

1. the Margna unit, composed of basement rocks with a Mesozoic sedimentary cover
2. the Malenco unit, one of the largest *ultramafic*[2] masses of the Alps, dominated by variably serpentinized ultramafic rocks
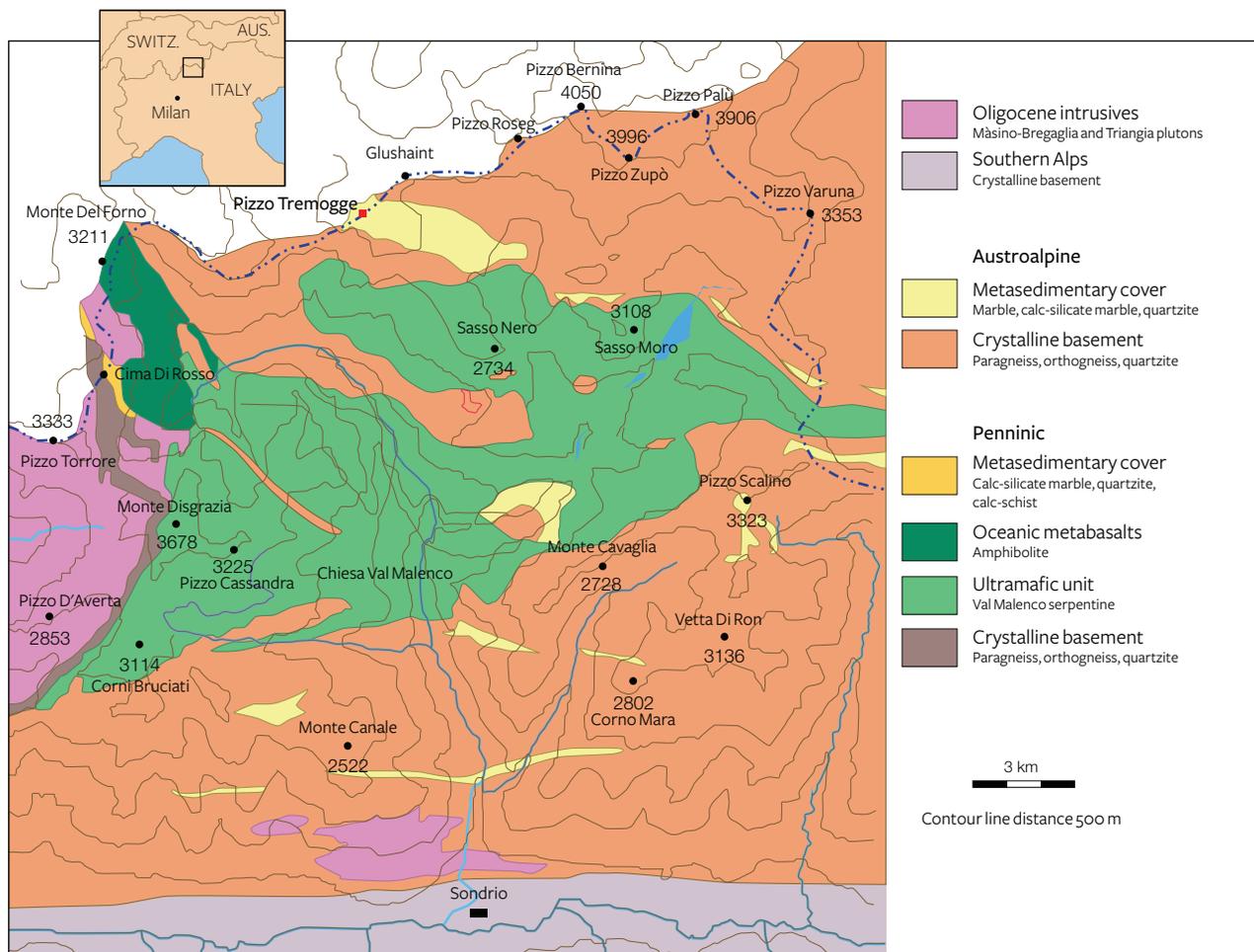
Figure 4. This geological map of Val Malenco shows the rocks constituting the Margna unit (brown and light yellow), the Malenco unit (dark green), and the Monte del Forno unit (light green). Gem-quality serpentine is found in the metasedimentary cover, consisting mainly of marbles, of the Margna unit. Modified from Adamo et al. (2009).

3. the Monte del Forno unit, an *ophiolite*[3] suite, consisting of oceanic metabasaltic rocks

In the Margna unit, the crystalline basement rocks show intercalations of carbonate rocks both of Paleozoic and Mesozoic age (Bedogné et al., 1993). The more ancient lithologies consist mainly of calcite-bearing marbles that preserve the amphibolite-facies paragenesis conditions of the enclosing rocks (gneisses and metagabbros). The composition of these marbles is not homogenous and is mainly related to the different proportions of carbonate and other associated minerals. Marbles in the area of Pizzo Tremogge (again, see figure 2), located 2800 m above sea level, are multicolored (yellow, yellow-green, and brown-orange) and show a rich mineral content, with magnesium silicates (clinohumite, olivine, serpentine, diopside, chlorite, and phlogopite), spinel, graphite, hematite, pyrite, and brucite. In most cases,

olivine (forsterite) is completely replaced by yellow-green serpentine and chlorite (Bedogné et al., 1993).

MATERIALS AND METHODS

A total of 10 samples from Pizzo Tremogge, consisting of four rough and six cut specimens (four spheres and two freeforms), were investigated in this study (see table 1 and figure 5).

Optical properties and specific gravities (SG) of

---

[2]*Ultramafic*: Igneous rock with low silica content (less than 45% SiO_2). Ultramafic rocks are usually composed of greater than 90% mafic minerals, which are typically dark and have high magnesium and iron contents.

[3]*Ophiolite*: From the Greek "ophio" (snake) and "lithos" (stone). Ophiolite sequences are brilliant green, snake-like stratified serpentine minerals that form in altered oceanic crust and mantle. While ophiolites are rare, occurrences are found in localities around the world.

the six cut samples were determined at the Italian Gemological Institute (IGI) laboratory in Milan using standard gemological methods. Refractive indices (RI) were measured by the distant vision method using a Kruss refractometer with sodium light (589 nm) from a Leitz lamp, and methylene iodide saturated with sulfur and C_2I_4 as a contact liquid (RI = 1.80). A Mettler hydrostatic balance was used to determine the SG. Ultraviolet fluorescence was investigated with a short-wave (254 nm) and long-wave (366 nm) UV lamp.

Raman spectroscopic analyses were carried out on four thin petrographic sections cut from samples S1, S2, S3, and S4) at the University of Eastern Piedmont in Alessandria, Italy, using a Jobin Yvon LabRam HR800 μ-Raman spectrometer equipped with an Olympus BX41 microscope, an HeNe 20 mW laser working at 632.8 nm, and a charge-coupled device (CCD) air-cooled detector. The instrument was calibrated by checking the position and intensity of the Si band at 520.65 ± 0.05 cm^{-1} before every run. In order to balance signal against noise, at least 50 cycles of 20 seconds each were performed. The spectral

TABLE 1. Serpentine samples investigated in this study.

Sample	Appearance	Dimensions
S1	Thin section	4 × 2 cm
S2	Thin section	4 × 2 cm
S3	Thin section	4 × 2 cm
S4	Thin section	4 × 2 cm
S5	Sphere	1.02–1.05 cm diameter
S6	Sphere	1.06–1.07 cm diameter
S7	Sphere	1.04–1.05 cm diameter
S8	Sphere	1.02–1.03 cm diameter
S9	Freeform	1.30 × 2.23 × 0.60 cm
S10	Freeform	1.50 × 1.85 × 0.70 cm

region recorded ranged from 1200 to 200 cm^{-1}, where the vibrational lattice modes of the different minerals are located. Spectra were acquired using Origin 6.0 data analysis software. The mineral phases responsible for the different Raman bands observed were identified by previously published Raman spectra (Kloprogge et al., 1999; Rinaudo et al., 2003; Groppo et al., 2006) and the RRUFF database (http://rruff.info).

Backscattered electron images and quantitative chemical analyses of major and minor elements were performed at the University of Milan on four polished thin sections (4 × 2 cm in dimension, cut from the rough samples S1, S2, S3, and S4) after a petrographic study by optical microscope. Quantitative chemical analysis was performed using a JEOL JXA-8200 electron microprobe in wavelength-dispersive mode, under operating conditions of 15 kV accelerating voltage, 5 nA beam current, and count times of 30 seconds on peaks and 10 seconds on the background. The following elements were measured: Na, Mg, Al, Si, K, Ca, Ti, V, Cr, Mn, Ni, Zn, and Fe. Natural minerals or pure metals were used as the standards, and the raw data were corrected for matrix effects using a conventional φρZ routine in the JEOL software package. Detection limits were 0.01 wt.%.

Figure 5. These cut serpentines (7.35–13.78 ct) were among the samples investigated in this study. Photo by Rosangela Bocchio.

RESULTS AND DISCUSSION

Gemological Properties. The gemological properties of the six cut samples are reported in table 2. Serpentine from Pizzo Tremogge has a massive aspect, with a green to yellowish green to yellow color, sometimes with white or gray veins and black spots. The samples' spot RI was approximately 1.55, and SG ranged from 2.50 to 2.67, with variations related to the occurrence

of other minerals. In particular, specimens with many black inclusions had a higher SG. The data were consistent with those previously measured by Adamo et al. (2014) and within the range reported by O'Donoghue (2006). Moreover, the values of RI and SG matched those reported by Kim et al. (2006) for gem-quality serpentine jade from Korea, composed of antigorite (1.56 and 2.57, respectively). The SG of our specimens also corresponded with the values (2.50–2.73) measured by Lin et al. (2012) for serpentine jade from Jilin province in China, consisting of lizardite.

The serpentine samples from Pizzo Tremogge are inert to UV radiation and have a Mohs hardness of approximately 4, which is typical of serpentine (Kim et al., 2006; Xinying et al., 2012).

Petrographic Examination and Raman Spectroscopy.
When observed with a petrographic microscope, the samples showed a coarse-grained structure. Serpentine was the dominant mineral, alternating with carbonate (calcite and dolomite), quartz, brucite, and chlorite veins (figure 6).

The identification of serpentine minerals (lizardite, antigorite, and chrysotile) through petrographic examination is difficult, owing to their similar optical properties as well as their submicroscopic intergrowths (Rinaudo et al., 2003; Groppo et al., 2006). Four samples (S1, S2, S3, and S4) were therefore examined by petrographic Raman spectroscopy to determine their mineralogical composition. The Raman spectra of the four serpentine thin sections are shown in figure 7, whereas table 3 presents the bands observed and their assignments.

Comparison of the Raman spectra of serpentine from Val Malenco (figure 7) with those reported in
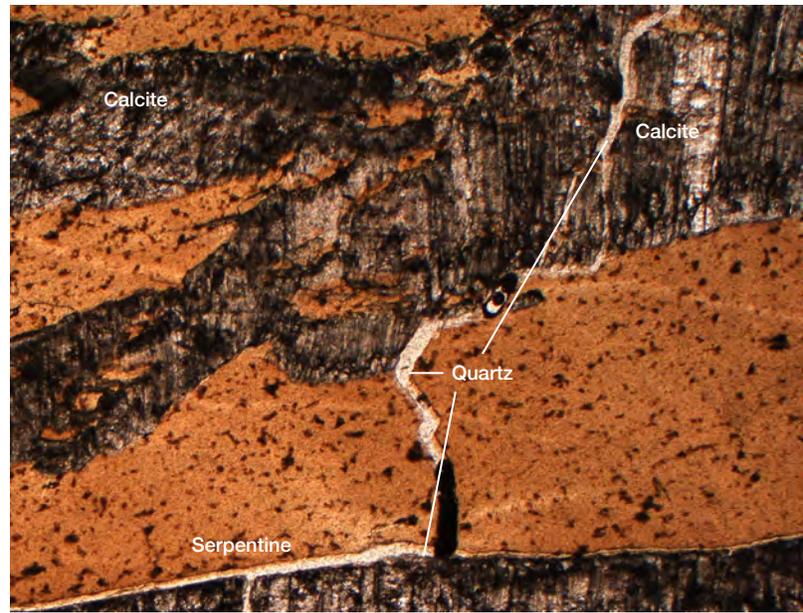
Figure 6. Observed in plane polarized light, this thin section of sample S2 shows serpentine (light brown), calcite (brown), and quartz veins (white). Photomicrograph by Rosangela Bocchio.

the literature for lizardite, chrysotile, and antigorite suggests the following:

- The spectrum of sample S1 shows an association of chlorite and lizardite. Since the thin petrographic sections are glued on the glass slide, resin is responsible for the bands at 1184, 1112, 1048, 821, 769, 736, and 639 cm^{-1} in the Raman spectrum. Repeated check analyses on the resin showed unequivocally the assignment of

TABLE 2. Gemological properties of the fashioned serpentine samples.

Samples	S5	S6	S7	S8	S9	S10
Cut	Sphere	Sphere	Sphere	Sphere	Freeform	Freeform
Weight (ct)	7.35	8.01	7.50	7.47	9.81	13.78
Color	Greenish yellow	Greenish yellow	Greenish yellow	Yellow	Yellowish green	Greenish yellow
Diaphaneity	Opaque	Opaque	Opaque	Opaque	Opaque	Opaque
RI	1.55	1.55	1.55	1.55	1.55	1.55
SG	2.61	2.62	2.61	2.63	2.50	2.67
Mohs hardness	4	4	4	4	4	4
UV fluorescence	Inert	Inert	Inert	Inert	Inert	Inert

TABLE 3. Band frequency (cm⁻¹) and assignment in four serpentine samples.

Sample 1	Sample 2	Sample 3	Sample 4	Band assignment	Reference
—	1097	—	—	Lizardite	Rinaudo et al. (2003)
—	—	1105	1103	Chrysotile	Kloprogge et al. (1999)
—	—	1088	—	Calcite	White (2009)
—	—	1044	1044	Antigorite	Kloprogge et al. (1999), Petriglieri et al. (2015)
—	—	714	—	Calcite	White (2009)
—	691	693	692	Lizardite, chrysotile	Rinaudo et al. (2003) Petriglieri et al. (2015)
	—	688	—	Mixed antigorite-chrysotile	Groppo et al. (2006)
690	—	—	—	Chlorite-lizardite	Groppo et al. (2006), Prieto et al. (1991)
—	628	629	629	Lizardite, chrysotile	Rinaudo et al. (2003)
546	—	552	—	Chlorite	Prieto et al. (1991)
—	—	—	520	Antigorite	Rinaudo et al. (2003)
	—	463–464	464	Chrysotile, antigorite	Kloprogge et al. (1999), Groppo et al. (2006)
463	—	—	—	Chlorite	Prieto et al. (1991)
—	—	432	434	Chrysotile	Kloprogge et al. (1999)
388	392	391	390	Lizardite, chrysotile	Rinaudo et al. (2003), Petriglieri et al. (2015)
—	—	380	382	Antigorite	Groppo et al. (2006)
357	—	358	—	Chlorite	Prieto et al. (1991)
349	349	346	347	Lizardite, chrysotile	Rinaudo et al. (2003), Petriglieri et al. (2015)
—	—	321	321	Chrysotile	Kloprogge et al. (1999)
—	—	284	—	Calcite	White (2009)
284				Chlorite	Prieto et al. (1991)
238	235	230–234	232	Lizardite, chrysotile, antigorite	Rinaudo et al. (2003), Petriglieri et al. (2015)

"—": Peak is not present.

these peaks. The more intense band at 690 cm⁻¹ is generated by the combination of the more intense bands of chlorite at 682–683 cm⁻¹ (Prieto et al., 1991) and lizardite at 690–693 cm⁻¹ (Rinaudo et al., 2003; Groppo et al., 2006). The presence of chlorite is confirmed by the observation of bands at 546, 463, 357, and 284 cm⁻¹; lizardite crystallization is indicated by the bands at 388 and 238 cm⁻¹. As demonstrated by Groppo et al. (2006), in lizardite the band near 390 cm⁻¹ shifts toward lower wavenumbers, with increasing amounts of Al replacing Si in the tetrahedral sites. In our case, chemical microprobe analyses show a lower SiO₂ content in sample S1 (see the "Chemical Analysis" section and table 4).

- The spectrum of sample S2 is unequivocally assigned to lizardite. The band at 1097 cm⁻¹ is unique to this variety of serpentine, whereas the bands at 691, 628, 392, 349, and 235 cm⁻¹ are in the proximity of lizardite and chrysotile (Rinaudo et al., 2003; Petriglieri et al., 2015).

- Sample S3 was analyzed in two different areas due to an evident color variation in different
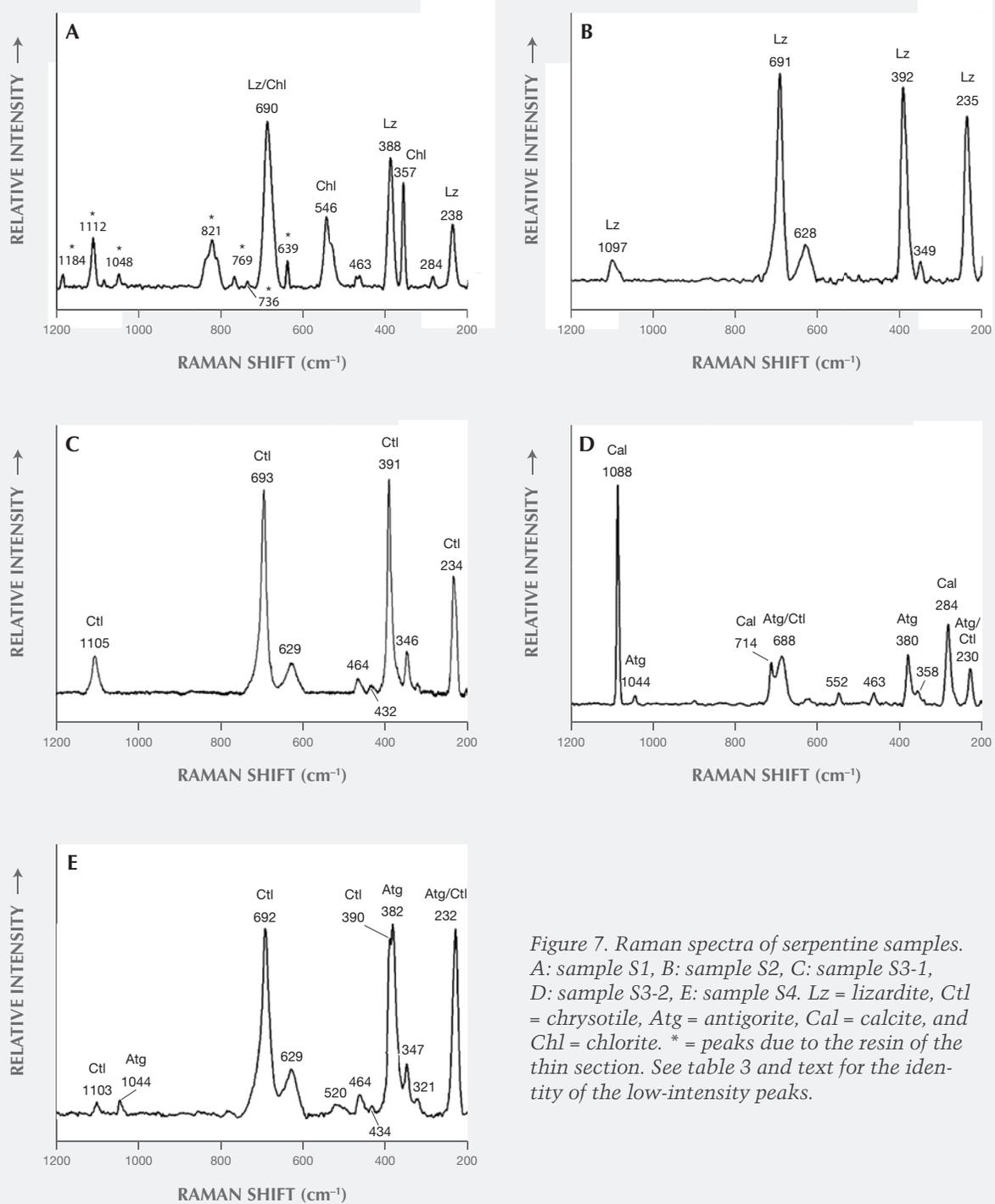
*Figure 7. Raman spectra of serpentine samples. A: sample S1, B: sample S2, C: sample S3-1, D: sample S3-2, E: sample S4. Lz = lizardite, Ctl = chrysotile, Atg = antigorite, Cal = calcite, and Chl = chlorite. * = peaks due to the resin of the thin section. See table 3 and text for the identity of the low-intensity peaks.*

areas of the stone. In the spectrum obtained from the greenish yellow area (figure 7C), the shape and the position of the single bands occur-

ring at 1105, 693, 629, 391, 346, and 234 cm⁻¹ correspond with those of pure chrysotile reported by Rinaudo et al. (2003) and Petriglieri et

TABLE 4. Microprobe analyses of four serpentine samples.

Sample wt.%	S1	S1	S2	S2	S2	S3	S3	S3	S4	S4	S4
SiO_2	40.55	40.37	39.81	40.21	40.31	42.66	42.86	42.73	41.52	43.26	43.20
TiO_2	0.12	0.17	0.21	0.14	0.16	0.12	0.15	0.15	0.11	0.14	0.07
Al_2O_3	2.16	2.23	3.13	3.08	3.13	1.19	1.21	1.23	1.01	0.66	0.72
Cr_2O_3	0.03	0.02	bdl	bdl	bdl	bdl	bdl	bdl	0.05	0.04	bdl
FeO	3.72	3.58	3.22	3.34	3.30	1.83	1.46	1.52	1.86	1.52	1.40
NiO	bdl	0.01	0.04	0.04	0.01	0.04	0.06	bdl	bdl	0.01	bdl
MnO	0.01	bdl	0.01	bdl	bdl	0.05	bdl	bdl	0.02	0.06	bdl
MgO	39.61	39.29	40.17	39.93	39.93	41.90	41.78	42.08	41.49	40.55	40.72
CaO	0.18	0.02	0.03	0.01	0.02	0.04	0.03	0.04	0.02	0.02	bdl
ZnO	bdl	bdl	0.02	bdl	0.08	0.05	0.04	bdl	0.08	0.09	0.09
Na_2O	bdl	bdl	0.01	0.01	bdl	bdl	bdl	0.02	0.01	bdl	bdl
K_2O	bdl	bdl	0.01	bdl	0.01	bdl	bdl	bdl	0.01	0.01	bdl
H_2O	12.62	12.54	12.69	12.72	12.74	13.00	13.00	13.01	12.73	12.84	12.83
Total	99.00	98.23	99.35	99.48	99.69	100.88	100.59	100.78	98.91	99.20	99.03
Tetrahedral cations											
Si^{4+}	1.925	1.929	1.881	1.897	1.897	1.969	1.978	1.969	1.957	2.022	2.020
Al^{3+}	0.075	0.071	0.119	0.103	0.103	0.031	0.022	0.031	0.043	–	–
Total	2.00	2.00	2.00	2.00	2.00	2.00	2.00	2.00	2.00	2.02	2.02
Octahedral cations											
Ti^{4+}	0.004	0.006	0.007	0.005	0.006	0.004	0.005	0.005	0.004	0.005	0.003
Al^{3+}	0.046	0.054	0.056	0.068	0.071	0.033	0.044	0.036	0.013	0.036	0.039
Cr^{3+}	0.001	0.001	–	–	–	–	–	–	0.002	0.001	–
Fe^{2+}	0.148	0.143	0.127	0.132	0.130	0.071	0.056	0.059	0.073	0.059	0.055
Ni^{2+}	–	–	0.002	0.001	0.001	0.001	0.002	–	–	0.001	–
Mn^{2+}	–	–	–	–	–	0.002	–	–	0.001	0.002	–
Mg^{2+}	2.803	2.798	2.830	2.808	2.802	2.882	2.875	2.891	2.915	2.825	2.839
Ca^+	0.009	0.001	0.002	0.001	0.001	0.002	0.001	0.002	0.001	0.001	–
Zn^{2+}	–	–	0.001	–	0.003	0.002	0.001	–	0.003	0.003	0.003
Na^+	–	–	0.001	0.001	–	–	–	0.002	0.001	–	–
K^+	–	–	0.001	–	–	–	–	–	–	0.001	–
Total	3.01	3.00	3.03	3.02	3.01	3.00	2.99	3.00	3.01	2.93	2.94
OH	4.00	4.00	4.00	4.00	4.00	4.00	4.00	4.00	4.00	4.00	4.00

bdl = below detection limit
"—": Peak is not present.

al. (2015). The bands detected at 464, 432, and 321 cm^{-1} can be assigned to chrysotile, in agreement with the spectrum obtained by Kloprogge et al. (1999). The spectrum recorded in the green area (figure 7D) shows a band at 1044 cm^{-1} that is ascribed unequivocally to antigorite because

it occurs in a frequency range where no band of chrysotile or lizardite is present (Rinaudo et al., 2003; Petriglieri et al., 2015). On the basis of the data from Groppo et al. (2006), bands at 463 and 380 cm^{-1} can also be assigned to antigorite, whereas the 688 cm^{-1} band appears at a wavenumber higher than that of pure antigorite (683 cm^{-1}) or pure chlorite (682, 683 cm^{-1}). The shift indicates the presence of small amounts of chrysotile. The first band of the spectrum detected at 1088 cm^{-1}, and the remaining bands at 714 and 284 cm^{-1}, are assigned to calcite, whereas the spectral features at 552 and 358 cm^{-1} are due to chlorite (Prieto et al., 1991).

- The Raman spectrum of sample S4 shows the occurrence of antigorite and chrysotile. The bands at 1103, 692, 629, 464, 434, 390, and 347 cm^{-1} are attributed to chrysotile, whereas the bands typical of antigorite occur at 1044, 520, and 382 cm^{-1}. The band recorded at 232 cm^{-1} may be produced by both chrysotile and antigorite, while the peak at 321 cm^{-1} is related to chrysotile (Kloprogge et al., 1999).

Chemical Analysis. Representative chemical analyses of four samples from Pizzo Tremogge are summarized in table 4, together with the structural formula calculated on the basis of five oxygen atoms (O) and four hydroxide groups (OH). The (Si + Al) cations are sufficient to completely fill the tetrahedral site. The

remaining Al is assigned, together with Ti^{4+}, Cr^{3+}, Fe^{2+}, Ni^{2+}, Mn^{2+}, Mg^{2+}, Ca^{2+}, Zn^{2+}, Na^+, and K^+, to the octahedral site.

The analyses are nearly stoichiometric, but we do observe a significant scatter in the composition, arising mainly from a variation in the aluminum and iron contents. This implies different substitutions of the cations for silicon and magnesium in the tetrahedral and octahedral sites, respectively. According to the data reported in the literature, these substitutions cause different crystal microstructures, playing a major role in stabilizing lizardite, chrysotile, or antigorite (e.g., Viti and Mellini, 1997).

The compositional patterns of Al_2O_3 and FeO observed in figure 8 show that in the four thin sections there is a general negative correlation of both oxides with silicon. In figures 8A and B, the analyses plot in two different areas. In fact, the S1 and S2 samples are enriched in Al_2O_3 and FeO and depleted in SiO_2 compared to the S3 and S4 samples. These compositional variations are related to the different serpentine species detected by Raman spectroscopy, although the occurrence of other minerals such as calcite, dolomite, and chlorite can also influence the microprobe measurement (Schwartz et al., 2013). In those four samples, the phases associated with serpentine minerals were chlorite, calcite, brucite, titanclinohumite (with a high TiO_2 content up to approximately 6 wt.%), and geikielite, the rare magnesian analogue of ilmenite. Minor amounts of titanium ($TiO_2 = 0.03$–

Figure 8. Plot of Al_2O_3 vs. SiO_2 (left), FeO vs. Al_2O_3 (center), and FeO vs. SiO_2 (right). Samples S1 and S2 are enriched in Al_2O_3 and FeO, as is common in lizardite. Samples S3 and S4 show the opposite behavior, consistent with their antigorite/chrysotile composition.
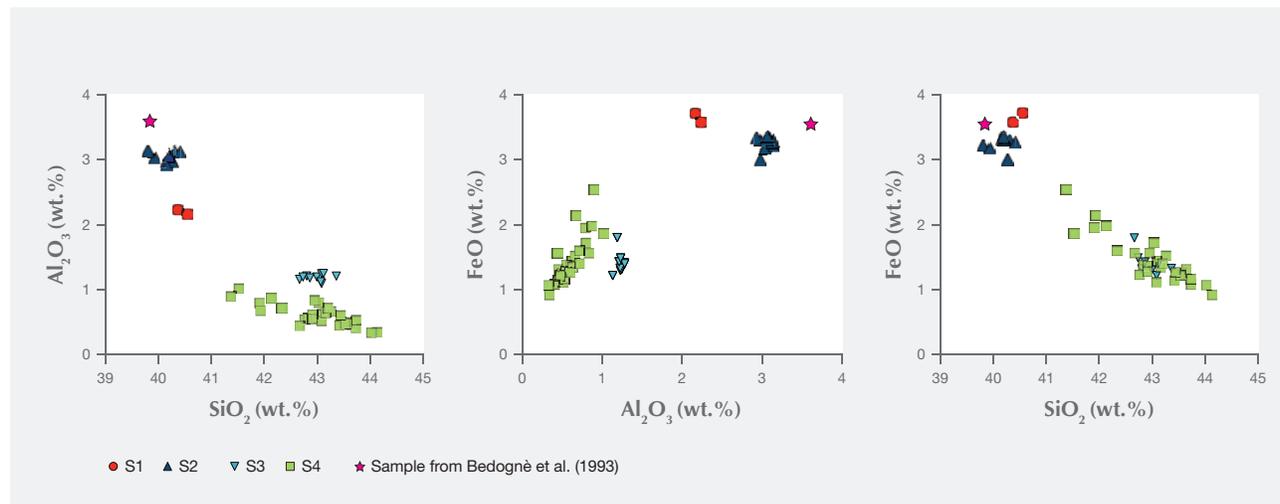
0.23 wt.%) and trace amounts of Ca, Cr, Ni, and Zn were also detected.

The chemical distinction between lizardite, chrysotile, and antigorite has been the subject of much speculation, and it remains an open question because the differences are very subtle. The grain size is also small, making it difficult to separate the various mineralogical phases for accurate analyses (Deer et al., 2009). According to the common interpretation, as well as the data from the literature (e.g., Viti and Mellini, 1997; Schwartz et al., 2013), lizardite is distinguished by its comparatively high Al content, whereas antigorite is always Al depleted, with Al_2O_3 never higher than 1 wt.% (Viti and Mellini, 1997). The SiO_2 content is generally lower in lizardite than in antigorite (Page, 1968). According to Viti and Mellini (1997), chrysotile has a wider compositional field, but its content of Al_2O_3 never exceeds 2 wt.%, regardless of SiO_2 content.

The chemical analyses of samples S1 and S2, as well as a previously reported sample of "noble" serpentine from Pizzo Tremogge (Bedogné et al., 1993), are enriched in Al and show a composition comparable to most of the lizardite analyzed by Viti and Mellini (1997). On the contrary, samples S3 and S4 showed depleted Al_2O_3 and enriched SiO_2, both typical features of antigorite. The broad variation of Al and Fe determined in these samples and the shifting of some analyses toward the compositional field of chrysotile (see the plot of FeO vs. Al_2O_3 in figure 8)

could be due to the occurrence of this mineral or to a mixture of antigorite/chrysotile, as suggested by Raman spectroscopy.

CONCLUSIONS

This paper offers the first detailed mineralogical and gemological investigation of serpentine-group minerals from Pizzo Tremogge in Val Malenco, Italy. On the basis of Raman spectroscopy and chemical analyses, we have proved that the samples are generally composed of the main phases of the serpentine group: chrysotile, lizardite, and antigorite. The occurrence of minor phases, such as carbonates, quartz, brucite, and chlorite, leads to a pleasing color variation in the cut gems, which is preferred in the Italian market over uniform colors.

It is well documented that serpentine minerals play an important role in the interpretation of many geological and petrological processes. Due to their different stability fields, which are strongly P/T dependent, their coexistence in the marbles of Pizzo Tremogge may provide a fundamental basis for understanding the complex metamorphic processes and geological setting of the Val Malenco area. In particular, the presence of antigorite suggests that the marbles at Pizzo Tremogge have experienced a high grade of metamorphism at temperature above approximately 320°C, at which antigorite crystals overprinted earlier-formed serpentine minerals such as lizardite and/or chrysotile.

ABOUT THE AUTHORS

Dr. Adamo (ilaria.adamo@igi.it) is a staff member of the Italian Gemological Institute (IGI) in Milan and a collaborator in the earth science department of the University of Milan. Dr. Bocchio is a professor of mineralogy, and Dr. Marinoni is a researcher, at the University of Milan. Dr. Diella is a senior researcher at the National Research Council, IDPA, Milan Organizational Support Unit. Dr. Rinaudo is professor of mineralogy in the department of science and technology innovation at the University of Eastern Piedmont in Alessandria, Italy.

REFERENCES

Adamo I., Bocchio R. (2013) Nephrite jade from Val Malenco, Italy: Review and update. *G&G*, Vol. 49, No. 2, pp. 98–106, http://dx.doi.org/10.5741/GEMS.49.2.98

Adamo I., Bocchio R., Diella V., Pavese A., Vignola P., Prosperi L., Palanza V. (2009) Demantoid from Val Malenco, Italy: Review and update. *G&G*, Vol. 45, No. 4, pp. 280–287, http://dx.doi.org/10.5741/GEMS.45.4.280

Adamo I., Diella V., Bocchio R., Marinoni N., Mainardi M., Fontana E., Rinaudo C. (2014) "Noble serpentine": a case study from Val Malenco, Central Alps, Italy. *Plinius*, Vol. 40, p. 329.

Bedogné F., Montrasio A., Sciesa E. (1993) *I Minerali della Provincia di Sondrio: Valmalenco*. Bettini, Sondrio, Italy.

Choudhary G. (2009) Gem News International: Serpentine cat's eye. *G&G*, Vol. 45, No. 2, pp. 151–152.

Deer W.A., Howie R.A., Zussman J. (2009) *Rock-Forming Minerals, Volume 3B: Layered Silicates Excluding Micas and Clay Minerals.* The Geological Society, London, 314 pp.

Diella V., Adamo I., Bocchio R. (2014) Gem-quality rhodonite from Val Malenco (Central Alps, Italy). *Periodico di Mineralogia*, Vol. 83, No. 2, pp. 207–221, http://dx.doi.org/10.2451/2014PM0012

Evans B.W., Hattori K., Barronet A. (2013) Serpentinite: what, why, where? *Elements*, Vol. 9, No. 2, pp. 99–106, http://dx.doi.org/10.2113/gselements.9.2.99

Fubini B., Fenoglio I. (2007) Toxic potential of mineral dust. *Elements*, Vol. 3, No. 3, pp. 407–414, http://dx.doi.org/10.2113/gselements.3.6.407

Gramaccioli C.M. (1962) *I minerali valtellinesi nella raccolta di Pietro Sigismund* [*The Minerals in the Valtellina Collection of Pietro Sigismund*]. Fusi, Pavia, Italy, 179 pp. (in Italian).

Groppo C., Rinaudo C., Cairo S., Gastaldi D., Compagnoni R. (2006) Micro-Raman spectroscopy for a quick and reliable identification of serpentine minerals from ultramafics. *European Journal of Mineralogy*, Vol. 18, No. 3, pp. 319–329, http://dx.doi.org/10.1127/0935-1221/2006/0018-0319

Guillot S., Hattori K. (2013) Serpentinites: Essential roles in geodynamics, arc volcanism, sustainable development, and the origin of life. *Elements*, Vol. 9, No. 2, pp. 95–98, http://dx.doi.org/10.2113/gselements.9.2.95

Kim W.-S., Ahn H.-J., Kim D.-H., Yoon S.-H. (2006) Mineralogy and genesis of gem-quality serpentine jade from Korea. Geological Society of America, *Abstract with Programs*, Vol. 38, p. 93, https://gsa.confex.com/gsa/2006CD/webprogram/Paper102570.html

Kloprogge J.T., Frost R.L., Rintoul L. (1999) Single crystal Raman *microscopic study of asbestos mineral chrysotile. Physical Chemistry Chemical Physics*, Vol. 1, No. 10, pp. 2559–2564, http://dx.doi.org/10.1039/A809238I

Lin Xinying, Lin Xianzhou, Shuyi Y. (2012) Research on Serpentine Jade in Jilin Province. 2012 International Conference on Solid State and Materials. *Lecture Notes in Information Technology*, Vol. 22, pp. 96–100.

Müntener O., Hermann J., Trommsdorff V. (2000) Cooling history and exhumation of lower-crustal granulite and upper mantle (Malenco, Eastern Alps). *Journal of Petrology*, Vol. 41, No. 2, pp. 175–200, http://dx.doi.org/10.1093/petrology/41.2.175

O'Donoghue M. (2006) *Gems*, 6th ed. Butterworth-Heinemann, Oxford, UK.

Page N.J. (1968) Chemical differences among the serpentine "polymorphs." *American Mineralogist*, Vol. 53, No. 1–2, pp. 201–205.

Petriglieri J.R., Salvioli-Mariani E., Mantovani L., Tribaudino M., Lottici P.P., Laporte-Magoni C., Bersani D. (2015) Micro-Raman mapping of the polymorphs of serpentine. *Journal of Raman Spectroscopy*, Vol. 46, No. 10, pp. 953–958, http://dx.doi.org/10.1002/jrs.4695

Prieto A.C., Dubessy J., Cathelineau M. (1991) Structure-composition relationships in trioctahedral chlorites: a vibrational spectroscopy study. *Clays and Clay Minerals*, Vol. 39, No. 5, pp. 531–539.

Rinaudo C., Gastaldi D., Belluso E. (2003) Characterization of chrysotile, antigorite and lizardite by FT-Raman spectroscopy. *The Canadian Mineralogist*, Vol. 41, No. 4, pp. 883–890, http://dx.doi.org/10.2113/gscanmin.41.4.883

Schwartz S., Guillot S., Reynard B., Lafay R., Debret B., Nicollet C., Lanari P., Auzende A.L. (2013) Pressure-temperature estimates of the lizardite/antigorite transition in high pressure serpentinites. *Lithos*, Vol. 178, pp. 197–210, http://dx.doi.org/10.1016/j.lithos.2012.11.023

Viti C., Mellini M. (1997) Contrasting chemical compositions in *associated lizardite and chrysotile in veins from Elba, Italy. European Journal of Mineralogy*, Vol. 9, No. 3, pp. 585–596, http://dx.doi.org/10.1127/ejm/9/3/0585

White S.N. (2009) Laser Raman spectroscopy as a technique for identification of seafloor hydrothermal and cold seep minerals. *Chemical Geology*, Vol. 259, No. 3–4, pp. 240–252, http://dx.doi.org/10.1016/j.chemgeo.2008.11.008

For online access to all issues of GEMS & GEMOLOGY from 1934 to the present, visit:

gia.edu/gems-gemology

IDENTIFICATION OF "PISTACHIO" COLORED PEARLS TREATED BY BALLERINA PEARL CO.

Chunhui Zhou, Joyce Wing Yan Ho, Sally Chan, Jessie Yixin Zhou, Surjit Dillon Wong, and Kyaw Soe Moe

Cultured pearls from *Pinctada margaritifera* can exhibit a broad range of natural bodycolors, including various pistachio-like colors ranging from greenish yellow to yellowish green. Bead-cultured pearls from *P. margaritifera*, treated by Ballerina Pearl Co. and possessing intense pistachio colors, have entered the market. Similar to Ballerina's "chocolate pearls," these pistachio colors are usually modified from natural gray to dark gray colors by a series of chemical and physical processes. No foreign coloring agent was detected in this study, and the treatment was generally stable. Cultured pearls treated by Ballerina's method can be identified by their appearance, UV-Vis-NIR reflectance spectra, Raman photoluminescence, and different UV fluorescence intensities under DiamondView imaging. Other experiments indicated that bleaching may not play a significant role in changing the color of these pearls. The processes may involve sophisticated chemical and physical techniques that can turn natural gray colors into stable pistachio colors.

Most Tahitian cultured pearls from *Pinctada margaritifera* exhibit neutral and near-neutral colors, with a large percentage showing black, dark gray, and silvery gray bodycolors; less frequently encountered natural hues include yellow and green. Some white specimens may also be produced from the mollusk (Strack, 2001). In addition to these bodycolors, various overtones such as pink, green, and blue often result from the reflection and interference of incident white light (Elen, 2002; Goebel and Dirlam, 1989; Cartier et al., 2012; Karampelas et al., 2011a). Fancy

color descriptions such as *pistachio* (yellowish green to greenish yellow) and *peacock* (dark green-gray to blue-gray with pink to purple overtone) have also been widely used to describe certain color ranges in cultured pearls from *P. margaritifera*.

Tahitian cultured pearls are often only washed and lightly tumbled after harvest and then sorted into broad categories: size, shape, color, and luster (Gemological Institute of America, 2011). GIA's laboratory has previously reported on "chocolate pearls," Tahitian cultured pearls grown in *P. margaritifera* and treated by Ballerina Pearl Co. (Wang et al., 2006; Du Toit et al., 2008). Ballerina subsequently produced pistachio-colored pearls using similar starting materials: naturally colored gray to dark gray Tahitian cultured pearls with various modifying hues and overtones (figure 1). These pearls show more intense and saturated hues than those usually seen in natural-color pistachio pearls grown within this species.

The present study focuses on the identification of treated pistachio cultured pearls using both standard gemological testing methods and advanced instrumental techniques. Ballerina was asked to treat 12 Tahitian cultured pearls specifically for this study. Naturally colored pistachio cultured pearls were also examined, and the results were compared with their treated counterparts. Lastly, several simple experiments were conducted to confirm whether a bleaching process was the mechanism that produced this unusual pearl coloration.

MATERIALS AND METHODS

A total of 12 Tahitian bead-cultured pearls with dark gray to dark greenish gray colors, ranging from 8.80 to 12.25 mm, were treated by Ballerina Pearl Co. using its proprietary processes. Eight of these pearls were supplied by Ballerina, and four additional samples were obtained from various sources. Eight naturally colored pistachio pearls from *P. margaritifera* were also tested in this study (figure 2). These naturally colored pearls exhibited a yellowish green hue similar to that of the treated cultured pearls. They

Figure 1. A graduated strand containing 43 yellowish green ("pistachio") bead-cultured pearls produced by black-lipped Pinctada margaritifera *and treated by Ballerina Pearl Co. The cultured pearls range from 9.13 to 10.80 mm. Photo by Sood Oil (Judy) Chia.*

were selected by experienced gemologists from multiple reliable sources, including two in Fiji. Finally, nine additional Tahitian cultured pearls were used in chemical treatment experiments conducted at GIA.

The pearls were examined with a standard gemological microscope; the microscopic images were obtained using a Nikon SMZ 1500 stereomicroscope. The fluorescence reaction was observed in a darkened room using a conventional 4-watt long-wave (365 nm) and short-wave (254 nm) lamp. UV-Vis-NIR reflectance spectra were obtained with an Ocean Optics USB 2000+ UV-Vis-NIR spectrophotometer. Fluorescence images were recorded using a DTC

Figure 2. Eight natural-color pistachio pearls ranging from 9.70 × 9.40 mm to 15.00 × 12.30 mm, produced by black-lipped pearl oysters, were examined in this study. Photo by Sood Oil (Judy) Chia.

DiamondView instrument (<225 nm excitation). The 12 samples were also tested with a Thermo Scientific Nicolet Nexus 6700 FTIR spectrometer equipped with a KBr beam splitter, a Thermo Scientific ARL Quant'x EDXRF spectrometer, and a Renishaw inVia Raman microscope under 514 nm laser excitation (1800 l/mm grating, 15 s, and 100–1800 cm^{-1} spectral range for Raman analysis; 1800 l/mm grating, 12 s,

In Brief

- Cultured pearls from *P. margaritifera* treated by Ballerina Pearl Co. to create a unique "pistachio" color have recently entered the market.

- These pearls are generally stable and are identifiable by their general appearance, as well as through the use of UV-Vis-NIR reflectance spectroscopy, Raman photoluminescence, and ultra short-wave UV fluorescence imaging.

- Bleaching experiments suggest that this method may not play a significant role in the treatment process.

and 518–850 nm spectral range for Raman photoluminescence analysis).

Chemical stability tests were carried out by immersing three treated pearls in ethanol, acetone, and isopropanol, respectively, for six hours at room temperature. Bleaching experiments were conducted on all studied pearls using various chemical solutions and household products. Stabilized 3% hydrogen peroxide, a common antiseptic solution, was used for mild
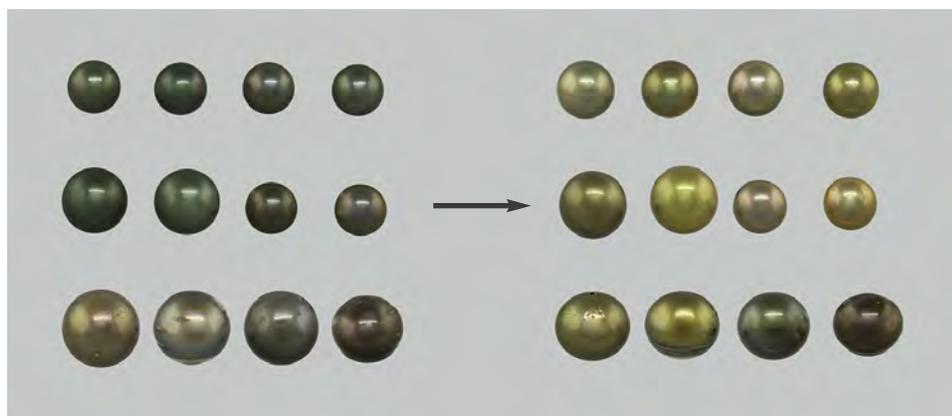
Figure 3. The bodycolors of the 12 samples modified by Ballerina Pearl Co. before and after treatment show the changes produced by the processes. Top row: BA 01–BA 04; middle row: BA 05–BA 08; bottom row: GIA 01–GIA 04. Photos by Sood Oil (Judy) Chia.

bleaching tests. A more concentrated hydrogen peroxide (up to 15%) was prepared by diluting a 30% stabilized H_2O_2 purchased from Sigma-Aldrich. Adding ammonium hydroxide to activate the hydrogen peroxide's bleaching capability ensured a basic pH environment of 8–9. Occasional heating up to approximately 65°C for four to six hours during the treatment period of one to four days was conducted to facilitate any possible reaction. Schwarzkopf Premium Lift 9+ hair bleach powder and Premium Care Developer (6% hydrogen peroxide) were used for all bleaching experiments; directions on the product packaging were followed (mixing approximately 35 g of powder with 50–90 g of developer to create a rich bleaching cream).

RESULTS

General Observations and UV Fluorescence. Prior to treatment, the 12 Tahitian cultured pearls exhibited dark gray to dark greenish gray colors with fair to good luster (figure 3, left). Post-treatment color changes varied, with most of the pearls showing a decrease in tone and an increase in yellow and green hues (figure 3, right). The most prominent color changes were observed on three samples provided by Ballerina (BA 02, 04, and 06), where the dominant hue changed from dark gray to yellowish green or greenish yellow. Three pearls turned from dark gray to brown with various modifying hues (BA 08 and GIA 01 and 02). Two pearls remained gray but were slightly modified by a green hue (BA 01 and 05). The remaining four pearls did not show a significant enough color change to move to another range in GIA's Pearl Color Grading Reference Chart. Slight changes within the same color range were still noted on some specimens; both the bodycolors and the apparent overtones of these pearls changed. Changes in overtone varied from sample to sample—for in-

stance, from pink and green to strong pink in BA 02, but from pink and green to none in BA 04. In many cases, the green overtone became the dominant color or modifier. Luster generally remained unaltered, although three samples showed slight improvement after treatment. No obvious UV fluorescence was observed under either long-wave or short-wave UV. A summary of these observations is listed in table 1.

In contrast, naturally colored pistachio pearls showed subtle yellowish green to greenish yellow bodycolors. They had lower saturation and lighter tone than the treated samples. They were mostly inert under both long-wave and short-wave UV, except for one with lighter tone that showed weak yellow fluorescence. A summary of these observations is listed in table 2.

Microscopic Observation and DiamondView Imaging. Microscopic observation of natural-color Tahitian cultured pearls revealed overlapping nacre platelets formed by aragonite crystals, with organic conchiolin materials between each layer. The conchiolin materials were a mixture of beta-chitin and an assemblage of acidic glycoproteins (Levi-Kalisman et al., 2001). No dye concentration was observed on the surfaces after treatment (figure 4). Pearls with numerous white blemishes were specifically chosen for this treatment, and the blemish areas were not altered even though the nacre around them changed color. Overall, the treatment produced an even surface color, as opposed to the spotty and patchy coloration found in many dyed pearls. Polishing lines were also observed on some samples, and Ballerina later confirmed that polishing was part of the treatment process (A. Auerbach, pers. comm., 2014).

Although observation under UV light is not very helpful in identifying treated pistachio pearls, fluo-
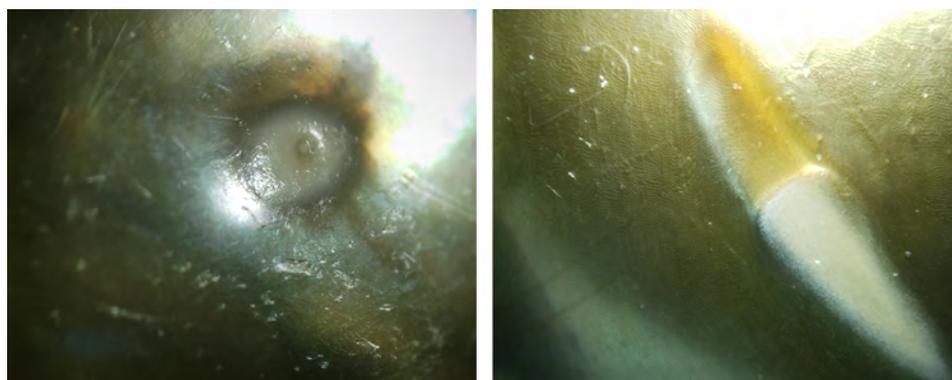
Figure 4. Microscopic images on the white blemish areas of treated pistachio pearls GIA 01 (left, field of view 2.0 mm) and GIA 02 (right, field of view 2.7 mm) did not reveal any dye concentrations. Photomicrographs by Sally Chan.

rescence images captured using the DiamondView with its ultra-short-wave UV source (<225 nm excitation) proved useful. Under the same testing conditions, both untreated dark gray and pistachio pearls showed moderate to strong bluish fluorescence, while treated pistachio pearls were consistently inert (figure 5). The strong bluish fluorescence in natural-color Tahitian cultured pearls and the inert reaction in treated samples were consistently observed under the same experimental conditions. Only sample GIA 03 still showed a strong bluish fluorescence after treatment. It was also the pearl that showed almost no color change, so we suspected that this pearl was not effectively treated by Ballerina. The results suggested that DiamondView imaging might be useful for identification of other color treatments in pearls, although this was beyond the scope of the study.

UV-Vis-NIR Reflectance Spectra. The naturally colored dark gray to dark greenish gray *P. margaritifera* pearls generally showed a distinct reflectance feature at 700 nm, with a relatively flat spectral pattern in the 400–600 nm region. Small features were observed at around 405 and 495 nm, consistent with previous studies (Karampelas et al., 2011a,b). Treated pearls with obvious color changes showed a reduced reflectance toward the lower visible region, with broader, more prominent reflectance troughs around the 405 nm region than before treatment. Unlike treated chocolate pearls, where the 700 nm absorption feature becomes weaker and less distinct after treatment (Wang et al., 2006), the feature was generally unaffected in pistachio pearls (figures 6 and 7). Three of the 12 samples (BA 07, GIA 03, and GIA 04) showed little UV-Vis-NIR spectral difference before

TABLE 1. Properties of pistachio cultured pearls before and after treatment by Ballerina Pearl Co.

	Bodycolor		Overtone		Luster		UV fluorescence	
	Before	After	Before	After	Before	After	Before	After
BA 01	Dark gray	Dark greenish gray	Weak pink	Pink	Good	Good	None	None
BA 02	Dark gray	Yellowish green	Pink and green	Strong pink	Good	Good	None	None
BA 03	Dark gray	Dark gray	Pink and weak green	Pink and green	Good	Good	None	None
BA 04	Dark gray	Yellowish green	Pink and green	None	Good	Very good	None	None
BA 05	Dark gray	Green-gray	None	None	Fair	Fair	None	None
BA 06	Dark gray	Greenish yellow	None	None	Fair	Fair	None	None
BA 07	Dark gray	Dark gray	Pink and weak green	Pink and green	Good	Good	None	None
BA 08	Dark gray	Green-brown	Strong pink	Pink and green	Good	Good	None	None
GIA 01	Dark gray	Yellow-brown	Weak green	None	Fair	Good	None	None
GIA 02	Dark gray	Greenish brown	Strong green	Weak pink	Good	Good	None	None
GIA 03	Dark greenish gray	Dark greenish gray	Weak pink and green	None	Good	Good	None	None
GIA 04	Dark gray	Dark gray	Pink and green	Pink and green	Fair	Good	None	None
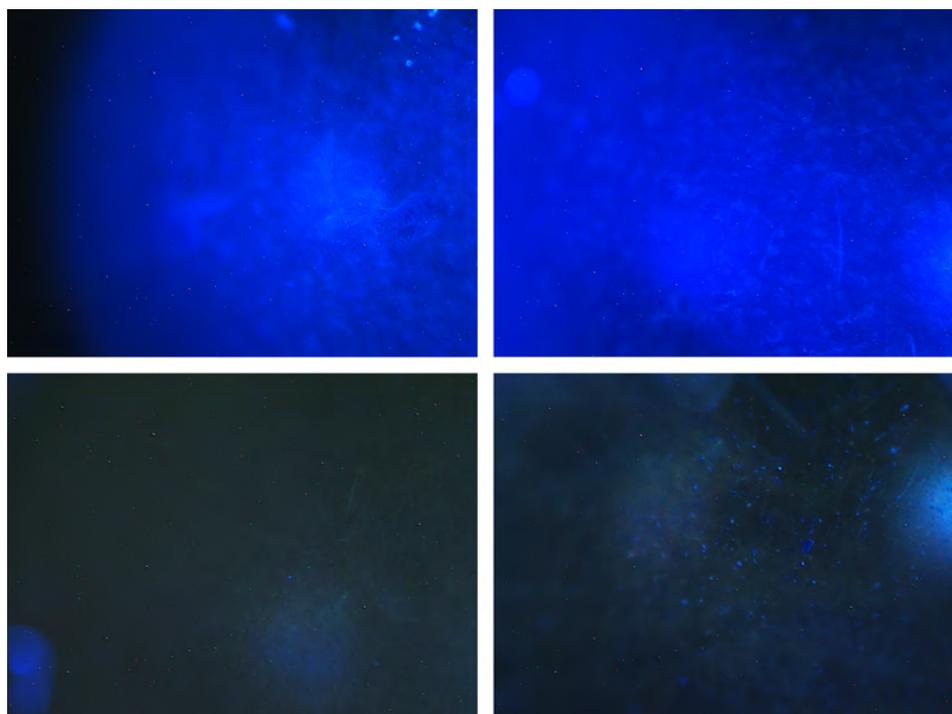
Figure 5. DiamondView fluorescence images of a naturally colored pistachio pearl (top left), a naturally colored dark gray pearl (top right), and treated Tahitian cultured pearls BA 06 (bottom left) and GIA 02 (bottom right) showed distinct differences in fluorescence intensity under identical experimental conditions. Images by Kyaw Soe Moe.

and after treatment, as their colors were generally unchanged and treatment was not very successful. Finally, the spectra of natural-color pistachio pearls showed subtle reflectance features in the 400 nm region, compared to the deep troughs found in many treated pearls (figure 8). The characteristic 495 nm feature seen in many naturally colored gray, black, and brownish pearls was also observed in our naturally colored pistachio samples, consistent with an earlier study on light to medium yellow and greenish yellow pearls from *P. margaritifera* (Elen, 2002). The 495 nm feature was significantly diminished, and in some cases removed, in the treated pearls.

Raman and Photoluminescence (PL) Spectroscopy. Raman spectra (not shown) of both untreated and treated pearls generally showed various vibrational modes of aragonite, the main component of pearls. Previous studies have demonstrated that Raman spectroscopy can pinpoint natural pigments in freshwater pearls (Karampelas et al., 2007), and may even detect tiny pigment peaks related to porphyrin in both *Pinctada margaritifera* and *Pteria sterna* cultured pearls (Kiefert et al., 2004). This technique was not very useful for detecting natural pigments in our samples due to overall high fluorescence background. To better visualize the fluorescence characteristics of

TABLE 2. Gemological properties of natural-color pistachio cultured pearls.

	Bodycolor	Overtone	Luster	UV fluorescence
N 01	Greenish yellow	Green and pink	Very good	None
N 02	Yellowish green	Green and pink	Very good	None
N 03	Green-gray	Green and pink	Good	None (LW); very weak yellow (SW)
N 04	Yellowish gray	None	Fair	None
N 05	Green-gray	None	Fair	None
N 06	Light green-gray	None	Fair	None
N 07	Yellowish green	Green and pink	Good	None
N 08	Yellowish green	Green and pink	Good	None
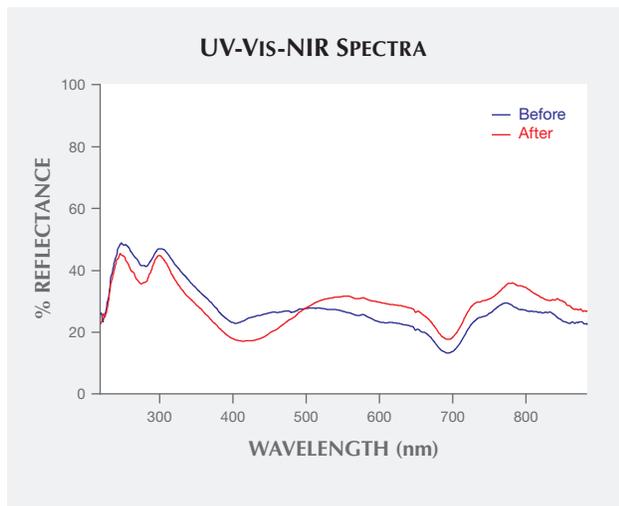
Figure 6. UV-Vis-NIR reflectance spectra of BA 02 before (blue) and after (red) treatment showed major spectral differences in the 405 nm region.

Figure 8. UV-Vis-NIR reflectance spectra are shown for a natural-color pistachio pearl (N 02, blue) and a treated pistachio pearl (BA 06, red). The treatment removed the 495 and 405 nm features.

these pearls upon laser excitation, we collected Raman photoluminescence (PL) data. We found that shells of various mollusk species can show the same distinct triple-peak PL spectra pattern at around 620, 650, and 680 nm under 514 nm laser excitation (figure 9). Similar observations have been noted previously (Karampelas et al., 2011b). These features are most prominent in *Pteria* species such as *P. sterna* and *P. penguin*, and to a lesser degree in *Pinctada margaritifera*. Both untreated dark gray Tahitian samples and naturally colored pistachio pearls showed a similar triple-peak pattern to the shell samples we studied

earlier, while the treated pearls exhibited a flattened (or less defined) area at around 650 nm and also showed stronger fluorescence.

A more useful way to look at the fluorescence is to compare the ratio between the highest fluorescence intensity (in the 600–700 nm region of the spectra) and the main aragonite Raman peak at 545 nm (which correlates with the Raman shift band at 1085 cm^{-1}), as previously used in identifying treated golden pearls (Zhou et al., 2012). Comparing fluores-

Figure 7. UV-Vis-NIR reflectance spectra of GIA 02 before (blue) and after (red) treatment showed major spectral differences in the 405 nm region.

Figure 9. PL spectra of shells from Pteria sterna (red), Pteria penguin (green), Pinctada margaritifera (blue), and Pinctada mazatlanica (purple), using 514 nm laser excitation, display the characteristic triple-peak pigment-related pattern found in the shells of these species. This pattern, also found in pearls produced by these mollusks, serves as an identification criterion.
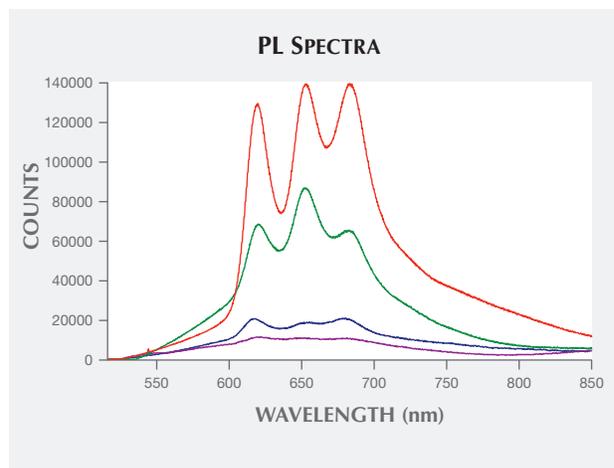
cence to the aragonite Raman peak ratio gives a more consistent relation between the peak signal and background fluorescence intensity of the pearl; this is more useful than looking at the absolute counts of the fluorescence or aragonite Raman peak alone. Our results indicated that naturally colored pistachio pearls generally showed a lower fluorescence-to-aragonite (F/A) ratio than treated pistachio pearls (figure 10). But one of the naturally colored pistachio pearls (N 04) also had a relatively high F/A ratio (table 3), and the F/A ratio ranges were much wider for these naturally colored Tahitian cultured pearls than we found in naturally colored golden South Sea cultured pearls. Further study on more naturally colored Tahitian specimens is needed to better distinguish treated and untreated samples.

FTIR and EDXRF Spectra. Like the Raman spectra, the FTIR spectra showed vibrational modes in the mid-IR region related to the mineral aragonite in both untreated and treated Tahitian samples. No further diagnostic features were observed that would help separate the treated and untreated samples. Energy-dispersive X-ray fluorescence (EDXRF) qualitative analysis revealed no foreign trace elements after treatment. Whereas inorganic dyes containing Ag or I may be detected in some dyed black or golden pearls (Elen, 2001), only the major element Ca and the trace element Sr were detected in these samples. Traces of Ni were also reported in some treated pistachio Tahitian cultured pearls previously examined by EDXRF (Lee

Figure 10. PL spectra were obtained for two treated samples (BA 06, purple; BA 04, blue) and two naturally colored specimens (N 03, green; N 05, red) using 514 nm laser excitation. The characteristic feature at around 650 nm became less defined in the treated cultured pearls; these samples generally showed a higher overall fluorescence intensity and F/A ratio than their natural counterparts.

et al., 2012), but no detectable traces were found in this study.

Stability Tests. The surfaces and colors of the treated samples were largely unchanged after immersing them in various common chemical solvents (acetone, ethanol, and isopropanol) for six hours at room temperature (figure 11), indicating that the treatment applied by Ballerina is generally stable. Further tests and observations are needed to check the long-term stability of these pearls, under both normal and harsh conditions. No color residue or foreign material was observed in the solution, ruling out the possibility

Figure 11. Immersing BA 04 (left), BA 05 (middle), and GIA 01 (right) in acetone, ethanol, and isopropanol, respectively, for six hours did not result in any major color change. Photo by Sood Oil (Judy) Chia.

TABLE 3. F/A peak ratio of natural-color pistachio pearls and four treated samples.	
Sample	F/A ratio
N 01	36
N 02	15
N 03	20
N 04	78
N 05	5
N 06	7
N 07	26
N 08	37
BA 04 (after treatment)	65
BA 05 (after treatment)	112
BA 06 (after treatment)	69
GIA 01 (after treatment)	70
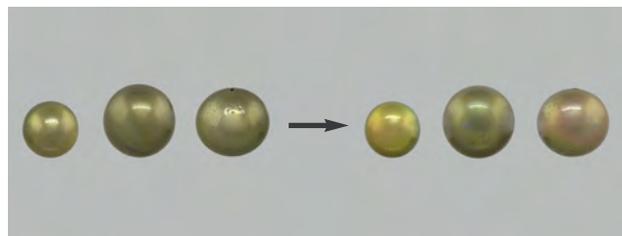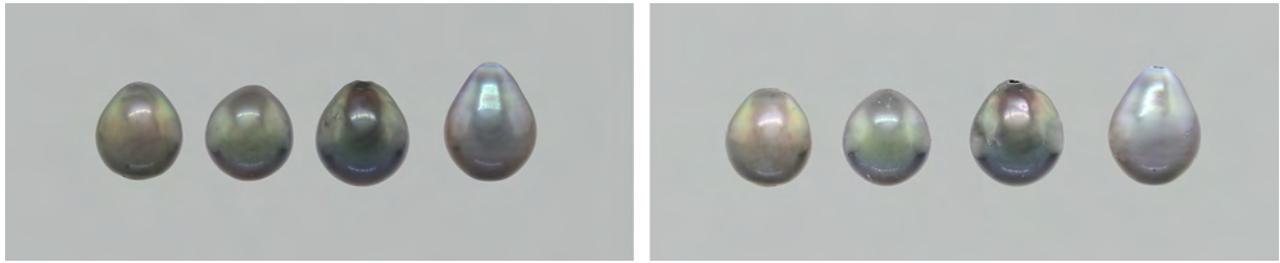
Figure 12. Four Tahitian cultured pearls, shown before (left) and after (right) identical bleach treatments using both solution and cream methods, exhibited minimal bodycolor changes. Photos by Sood Oil (Judy) Chia.

that coating materials dissolved from the surface of these treated pearls.

Bleaching Tests. Bleaching tests conducted on the natural-color Tahitian cultured pearls by both solution and cream methods resulted in no obvious color changes (figure 12). The samples generally lost their luster, but their overtones were enhanced after bleaching. This could indicate a change in nacre platelet structure that altered their interference with light (Liu et al., 1999; Snow et al., 2004), or a change to the organic components in between the nacre platelets. Some pearls had a slightly lighter tone after treatment, but the overall effect was subtle and ultimately insignificant. The UV-Vis spectra were virtually identical before and after the bleach test, except for slight differences in the overall reflectance level (possibly due to instrumental variations or changes in luster). Different experimental conditions may be needed for a stronger visual change, but it is more likely that bleaching alone cannot produce the desired pistachio color. A variety of other chemical agents may be involved in the treatment process, which remains proprietary. Additional bleaching

tests were conducted on two thin pieces of *P. margaritifera* shell. These samples displayed a greater degree of color lightening, especially at the edges of the shells, where light brown areas turned silver-white, confirming that hydrogen peroxide is capable of oxidizing the pigment compounds (figure 13). Parts of the shells broke away during the treatment, causing slight changes in their shape and appearance.

DISCUSSION

Pistachio pearls treated by Ballerina Pearl Co. usually exhibit saturated yellowish green to greenish yellow colors, modified from the natural dark gray colors of Tahitian cultured pearls. Other modified brownish or grayish colors of various saturations may also be produced. Many factors could affect the appearance of the final products, including the presence of various pigments in the starting materials and differences in experimental conditions and durations. According to Ballerina, the pearls were treated for different durations, and some were treated more "aggressively" than others, although the exact experimental conditions were not disclosed. The nature of the pigments responsible for the gray to black color of *P. margaritifera*

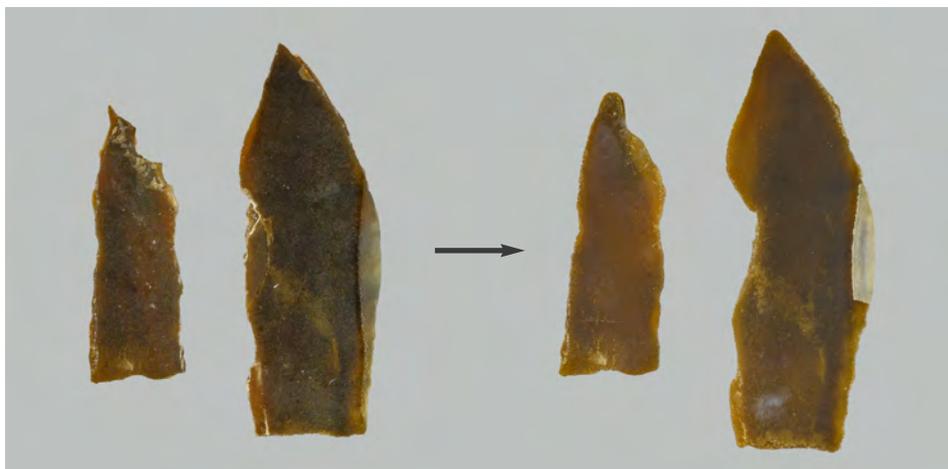*Figure 13. Two pieces of* P. margaritifera *shell before (left) and after (right) bleach treatment using both solution and cream methods, which lightened the samples' color, especially toward the edge of the larger shell. Photos by Sood Oil (Judy) Chia.*

shells and pearls can be attributed to melanin-like material (Jabbour-Zahab et al., 1992).

Microscopic examination of treated pistachio pearls did not reveal any dye concentration within or around surface blemishes, indicating that the processes involved differ from "simple" dye treatment. The largely unchanged 700 nm absorption peak, present in Tahitian cultured pearls and found in treated pistachio pearls, supports this conclusion, as the dye would be expected to infiltrate the nacre platelets and affect the absorption at the 700 nm region. Treated pistachio pearls did show a decrease in reflectance toward shorter wavelengths, with deep and broad reflectance troughs at around 405 nm, while both naturally colored dark gray pearls and pistachio pearls often displayed distinct absorption peaks at 405 nm (and sometimes also at 495 nm). This deep and broad absorption feature of treated pearls correlates with their more yellowish appearance and therefore represents an important tool to separate treated pistachio pearls.

Other useful techniques that aid in the identification of Ballerina's treated pistachio pearls are DiamondView fluorescence imaging and PL acquired with a Raman spectrometer. Both techniques examine the reactions of the pearls' surfaces and micron-deep surface layers to light excitation using different energy sources. Subtle differences in the PL properties of treated pistachio pearls have been found with the 650 nm feature. Other significant differences were found using the DiamondView, which was originally designed to observe the fluorescence images of diamonds and separate synthetic from natural diamonds. Natural-color Tahitian cultured pearls displayed strong fluorescence, regardless of bodycolor, while treated pistachio pearls showed little or no reaction. The results of the study demonstrated that Raman spectroscopy, EDXRF spectrometry, and FTIR spectrometry were not particularly helpful in separating treated and untreated pistachio pearls.

Bleaching was originally thought to be the main cause of the color change in Tahitian cultured pearls, similar to previously examined chocolate pearls (Wang et al., 2006). The possible presence of melanin pigments in Tahitian cultured pearls led us to hypothesize that the underlying mechanism could be similar to that seen in the bleaching of human hair. It has long been known that the principal pigments of human hair are the brown-black melanins (eumelanins) and the less prevalent red pigments (pheomelanins) (Robbins, 2002). In several studies on the bleaching of melanin compounds (Edman and Sulli-

van, 1965; Wolfram et al., 1970; Korytowski and Sarna, 1990), hydrogen peroxide has been used to oxidize the melanin compounds under alkaline conditions. The results of this study show that simple bleaching experiments cannot effectively modify the bodycolors of Tahitian cultured pearls, possibly due to the inability of the bleaching liquid and cream to penetrate and disperse into each layer of nacre. Only small changes in body tone and overtone were observed. The effect was more obvious on a thin piece of *P. margaritifera* shell, where the light brown coloration was whitened in one area, indicating the destruction and removal of pigments by hydrogen peroxide. Contrary to our expectations, bleaching alone did not cause the desired saturated greenish yellow or yellowish green color.

Pearls from *P. margaritifera* may contain more complex mixtures of pigments than just melanin. Porphyrin or uroporphyrin compounds may also be present, and these are responsible for the 405 nm absorption peak observed using UV-Vis-NIR reflectance spectroscopy (e.g., Miyoshi et al., 1987; Iwahashi and Akamatsu, 1994; Karampelas et al., 2011a,b). Porphyrin molecules are remarkably stable and have been found in fossilized shells. Some traces of porphyrins can combine with metals, while others are found in free form in mollusks. Previous studies have found that green pearls contain greater proportions of metalloporphyrins than pink pearls (Fox, 1979). Our UV-Vis spectra of treated pistachio pearls showed a more significant change in the 405 nm region, which suggests that the treatment had a stronger effect on porphyrin pigments than melanin pigments. The overall appearance of the finished products depends on the total concentrations and proportions of various pigments and the interference of light by nacre platelets, and the treatment may achieve this by modifying or removing certain pigments from the pearls.

CONCLUSIONS

This study has demonstrated that pistachio-colored pearls grown within *P. margaritifera* and treated by Ballerina Pearl Co. may be identified by their unique appearance, as well as by nondestructive advanced instrumental techniques such as UV-Vis-NIR reflectance spectroscopy, Raman photoluminescence, and DiamondView imaging. Indications of treatment may include significant and broad absorption features around 405 nm, a less-defined 650 nm PL feature under 514 nm wavelength laser excitation and relatively high F/A ratio, and weak or inert fluorescence reactions under the DiamondView. Pistachio

pearls treated by other companies may or may not show the same results, depending on the processes involved (Lee et al., 2012).

This study has also indicated that bleaching is not likely to be the main color-change mechanism in this treatment. The processes may involve more sophisticated chemical and physical techniques that can turn the dark gray color to a stable pistachio color, but no indications of dyeing were detected. These pistachio colors are generally stable when exposed to common household chemicals such as ethanol, acetone, and isopropanol. Continuing studies on the effects of different chemical agents or other techniques such as heating and irradiation on the color of *Pinctada margaritifera* pearls are needed to further understand the mechanism of this color change.

ABOUT THE AUTHORS
Dr. Zhou is a research scientist and supervisor of pearl identification at GIA in New York. Ms. Ho, Ms. Chan, and Ms. Zhou are staff gemologists, Ms. Wong is a production coordinator, and Mr. Moe is a research associate, also at GIA in New York.

REFERENCES

Cartier L.E., Krzemnicki M.S., Ito M. (2012) Cultured pearl farming and production in the Federated States of Micronesia. *G&G*, Vol. 48, No. 2, pp. 108–122, http://dx.doi.org/10.5741/GEMS.48.2.108

Du Toit G., Shen A.H., Breeding C.M. (2008) The color durability of "chocolate pearls" by Ballerina Pearl Co. *G&G*, Vol. 44, No. 3, pp. 234–241, http://dx.doi.org/10.5741/GEMS.44.3.234

Edman W.W., Sullivan A.T. (1965) Hydrogen peroxide hair bleaching composition and method. US Patent No. 3193464 A.

Elen S. (2001) Spectral reflectance and fluorescence characteristics of natural-color and heat-treated "golden" South Sea cultured pearls. *G&G*, Vol. 37, No. 2, pp. 114–123, http://dx.doi.org/10.5741/GEMS.37.2.114

——— (2002) Identification of yellow cultured pearls from the black-lipped oyster *Pinctada margaritifera*. *G&G*, Vol. 38, No. 1, pp. 66–72, http://dx.doi.org/10.5741/GEMS.38.1.66

Fox D.L. (1979) *Biochromy: Natural Coloration of Living Things*. University of California Press, Berkeley and Los Angeles.

Gemological Institute of America (2011) Cultured pearls–treatments and processes. *Solitaire International*, October, pp. 72–74, http://www.solitaireinternational.com/images/2110112304pearl_update_oct11.pdf.

Goebel M., Dirlam D.M. (1989) Polynesian black pearls. *G&G*, Vol. 25, No. 3, pp. 130–148, http://dx.doi.org/10.5741/GEMS.25.3.130

Iwahashi Y., Akamatsu S. (1994) Porphyrin pigment in black-lip pearls and its application to pearl identification. *Fisheries Science*, Vol. 60, No. 1, pp. 69–71, http://doi.org/10.2331/fishsci.60.69

Jabbour-Zahab R., Chagot D., Blanc F., Grizel H. (1992) Mantle histology, histochemistry and ultrastructure of the pearl oyster *Pinctada margaritifera* (L.). *Aquatic Living Resources*, Vol. 5, pp. 287–298. http://dx.doi.org/10.1051/alr:1992027

Karampelas S., Fritsch E., Mevellec J-Y., Gauthier J-P., Sklavounos S., Soldatos T. (2007) Determination by Raman scattering of the nature of pigments in cultured freshwater pearls from the mollusk *Hyriopsis cumingi*. *Journal of Raman Spectroscopy*, Vol. 38, pp. 217–230, http://dx.doi.org/10.1002/jrs.1626

Karampelas S., Fritsch E., Gauthier J-P., Hainschwang T. (2011a) UV-VIS-NIR reflectance spectroscopy of natural-color saltwater cultured pearls from *Pinctada margaritifera*. *G&G*, Vol. 47, No. 1, pp. 31–35, http://dx.doi.org/10.5741/GEMS.47.1.31

Karampelas S., Fritsch E., Hainschwang T., Gauthier J-P. (2011b) Spectral differentiation of natural-color saltwater cultured pearls from *Pinctada margaritifera* and *Pteria sterna*. *G&G*, Vol. 47, No. 2, p. 117.

Kiefert L., Moreno D.M., Arizmendi E., Hänni H.A., Elen S. (2004) Cultured pearls from the Gulf of California, Mexico. *G&G*, Vol. 40, No. 1, pp. 26–38, http://dx.doi.org/10.5741/GEMS.40.1.26

Korytowski W., Sarna T. (1990) Bleaching of melanin pigments. Role of copper ions and hydrogen peroxide in autooxidation and photooxidation of synthetic dopa-melanin. *Journal of Biological Chemistry*, Vol. 265, No. 21, pp. 12410–12416.

Lee B-H., Choi H-M., Kim Y-C., Miyazaki T. (2012) New treated yellow-green Tahitian pearl. Presentation at Korean Association of Crystal Growth (KACG).

Levi-Kalisman Y., Falini G., Addadi L., Weiner S. (2001) Structure of the nacreous organic matrix of a bivalve mollusk shell examined in the hydrated state using cryo-TEM. *Journal of Structural Biology*, Vol. 135, No. 1, pp. 8–17, http://dx.doi.org/10.1006/jsbi.2001.4372

Liu Y., Shigley J.E., Hurwit K.N. (1999) Iridescence color of a shell of the mollusk *Pinctada margaritifera* caused by diffraction. *Optics Express*, Vol. 4, No. 5, pp. 177–182, http://dx.doi.org/10.1364/OE.4.000177

Miyoshi T., Matsuda Y., Komatsu H. (1987) Fluorescence from pearls and shells of black lip oyster, *Pinctada margaritifera*, and its contribution to the distinction of mother oysters used in pearl culture. *Japanese Journal of Applied Physics*, Vol. 26, No. 7, pp. 1069–1072, http://dx.doi.org/10.1143/JJAP.26.1069

Robbins C.R. (2002) *Chemical and Physical Behavior of Human Hair*, 4th ed., Springer-Verlag, Berlin.

Snow M.R., Pring A., Self P., Losic D., Shapter J. (2004) The origin of the color of pearls in iridescence from nano-composite structures of the nacre. *American Mineralogist*, Vol. 89, No. 10, pp. 1353–1358, http://dx.doi.org/10.2138/am-2004-1001

Strack E. (2001) *Pearls*. Ruhle-Diebener-Verlag, Stuttgart, Germany.

Wang W., Scarratt K., Hyatt A., Shen A.H-T., Hall M. (2006) Identification of "chocolate pearls" treated by Ballerina Pearl Co. *G&G*, Vol. 42, No. 4, pp. 222–235, http://dx.doi.org/10.5741/GEMS.42.4.222

Wolfram L.J., Hall K., Hui I. (1970) The mechanism of hair bleaching. *Journal of the Society of Cosmetic Chemists*, Vol. 21, pp. 875–900.

Zhou C., Homkrajae A., Ho J.W.Y., Hyatt A., Sturman N. (2012) Update on the identification of dye treatment in yellow or "golden" cultured pearls. *G&G*, Vol. 48, No. 4, pp. 284–291, http://dx.doi.org/10.5741/GEMS.48.4.284

VARISCITE FROM CENTRAL TAJIKISTAN: PRELIMINARY RESULTS

Andrey K. Litvinenko, Elena S. Sorokina, Stefanos Karampelas, Nikolay N. Krivoschekov, and Roman Serov

An occurrence of variscite containing strengite, as well as other minerals from both the variscite and metavariscite groups, was discovered in the late 1970s in central Tajikistan. The material, ranging from light blue to light green to green, is suitable for cabochon cutting. The samples presented in this study showed traces of sulfur and arsenic, with higher iron and generally lower vanadium and chromium concentrations than variscites reported from other localities. These differences may result from the intergrowth of variscite with other minerals from the variscite and metavariscite groups.

Variscite (figure 1), a relatively common cave mineral that forms as a result of phosphate-bearing surface solutions reacting with aluminum-rich rocks (Calas et al., 2005), where the phosphate is provided by guano decomposition (Onac et al., 2004). First described in 1837 from a source close to Variscia, the former name of the Vogtland region in northeastern Germany, its chemical formula was determined in 1896 (Willing et al., 2008). Yet variscite was used in Neolithic jewelry and is found in many archaeological sites (e.g., Ervedosa, Portugal; Pannecé, France; and Sardinia, Italy; see Calas et al., 2005; Middleton et al., 2007; Querré et al., 2007; Willing et al., 2008).

Variscite is a member of the hydrous aluminum phosphate group, $Al(PO_4)\cdot 2H_2O$, while strengite is part of the iron phosphate group, $Fe^{3+}(PO_4)\cdot 2H_2O$. Both are orthorhombic phosphate members of the variscite mineral group, while mansfieldite, scorodite, and yanomamite are the arsenate isostructural members of this group. The general chemical formula of variscite group minerals is $A(XO_4)\cdot 2H_2O$, where A = Al, Fe^{3+}, In and X = P, As. Phosphate members of the variscite group (variscite and strengite) are isodimorphous with the metavariscite monoclinic phosphate mineral group members metavariscite and phosphosiderite, respectively.

Most of the variscite in the market today comes from the state of Utah, close to the cities of Lucin and Fairfield, though some of these mines are practically exhausted (Larsen, 1942; Solodova et al., 1985; Willing et al., 2008). The occurrences at Woodlands, Western Australia, and Yauli, Peru were discovered in 2004 and 2011, respectively (Willing et al., 2008; Hyršl, 2011).

Among the minerals of the variscite and metavariscite groups, variscite is most often used for carvings and ornaments (see Koivula, 1986; Fritz and Rockwell, 2006; Willing et al., 2008; and Hyršl, 2011). Variscite has a waxy luster and is transparent to translucent with a color range from white to brown and blue to green to yellow, which can cause misidentification as turquoise and chrysoprase (Willing et al., 2008). The Mohs hardness of the mineral is 3.5 to 4.5, as opposed to turquoise and chrysoprase, which both range above 5 (again, see Palache et al., 1951).

In 1979, variscite-bearing veins were found by one of the authors (AKL) in the headwaters of the Shing River, southwest of Marguzor Lake (39°09′ N, 67°50′ E; figure 2) in central Tajikistan. The occurrence is situated within the jaspers of the Akbasayskaya suite in the Shing-Magian antimony-mercury ore district, 1

Figure 1. These two variscite cabochons from central Tajikistan (1.8 × 0.7 × 0.3 cm and 1.2 × 0.5 × 0.6 cm) were cut from the samples used in the study. Photo by N.N. Krivoschekov.

Figure 2. Top: A map of Central Asia and Tajikistan. The red star shows the occurrence of variscite with other minerals of the variscite and metavariscite groups. Bottom: Marguzor Lake, surrounded by carbonate rocks (Argskaya suite). The occurrence is located on the right, in the background behind the massif of carbonate rocks. Photo by A.K. Litvinenko.

km east of the Chorroha antimony deposits (currently not in operation). The region forms the western part of the Zeravshan-Hissar structural-formational zone, which belongs to the Southern Tien Shan part of the Ural-Mongolian belt in the Hercynian mountain-folding region (Baratov, 1976). The collected samples, like those shown in figure 1, were visually identified at the mining site as chrysoprase, but X-ray powder diffraction (XRD) later determined that the material consists mainly of variscite and strengite, along with minor amounts of scorodite, metavariscite, phosphosiderite, jarosite, and quartz (Litvinenko et al., 2013). No mining activities have taken place in the area.

In this article, the gemological properties of variscite samples from central Tajikistan are presented along with spectroscopic and chemical data.

The results obtained are also compared with the existing data found in the literature on variscite samples from other occurrences.

MATERIALS AND METHODS
For this study, we investigated six variscites from different parts of the veins (figure 3). The microscopic characteristics of the samples and their reaction under a 5-watt short-wave (254 nm) and long-wave (365 nm) UV lamp were examined. Microhardness was measured by a PMT-3 tester with a load weight of 100 g for 10 seconds. Hydrostatic specific gravity (SG) was measured with a digital balance. Reflectance spectra from 380 to 1080 nm were acquired with an Ocean Optics QE65000 spectrometer using an HL-2000-HP 20 W light source and an R600-7 Vis-NIR reflection
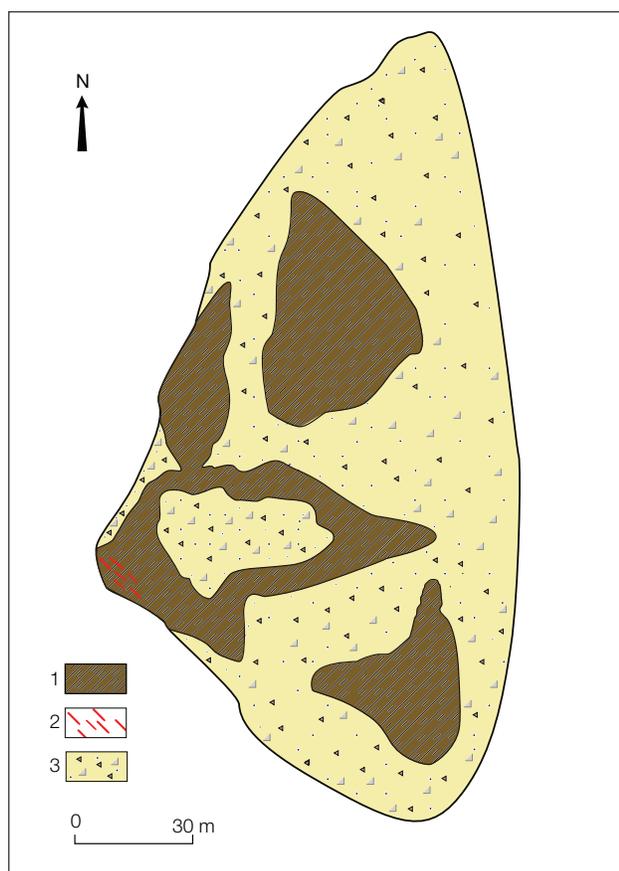
Figure 3. Geological scheme of the variscite occurrence: 1—jaspers of the Akbasayskaya suite, 2—veins of variscite and other minerals of the variscite and metavariscite groups, 3—quaternary sediments (after Litvinenko et al., 2013).

grooves/mm grating with slits set at 50 μm intervals, and the spectrometer was calibrated at 1332 cm⁻¹ using a natural diamond as a reference standard.

RESULTS AND DISCUSSION

The samples were aggregates ranging from light blue to light green to green (sometimes very similar to chrysoprase) and suitable for cabochon cuts of about 2 cm in length (again, see figure 1 and table 1). They had cryptocrystalline (rarely microgranular) structure, waxy luster, and conchoidal fractures. The measured microhardness was 231.5–386.7 kg/mm²

> ## In Brief
> - An occurrence of light blue to green variscite and other minerals of the variscite and metavariscite groups was discovered in central Tajikistan in the late 1970s.
> - The samples' color is principally due to relative concentrations of iron and chromium.
> - Compared to other localities, variscite from central Tajikistan shows generally high Fe and low Cr and V contents, as well as traces of sulfur and arsenic.
> - No variscite mining has taken place in the area.

probe, with a resolution of 1 nm, 20 scans, and an integration time of 500 ms. Chemical analysis was conducted with a Link ISIS energy-dispersive spectrometer (EDS) attached to a CAMSCAN-D4 electron scanning microscope. The following standards were used for quantitative measurements of elements within studied samples: synthetic Al_2O_3 (for Al), apatite USNM 104021 (for P), synthetic V_2O_5 (for V), synthetic Cr_2O_3 (for Cr), ilmenite USNM 96189 (for Fe and Ti), wollastonite STD 097 (for Ca), albite (for Na), synthetic microcline (for K), quartz (for Si), $PtAs_2$ (for As), barite (for S), and $PbTiO_3$ (for Pb). Raman spectra were acquired on a Renishaw Raman 1000 spectrometer coupled to a Leica DM LM microscope, using an Ar⁺ laser (514 nm) and 50× magnification. Laser power was 10 mW, with a 60-second acquisition time (three cycles), at a resolution of about 1.5 cm⁻¹, in the range from 200 to 1200 cm⁻¹. Rayleigh scattering was blocked using a holographic notch filter. Backscattered light was dispersed on an 1800

(between 4 and 5 on the Mohs scale), and SG ranged from 2.32 to 2.36. All samples were inert to long- and short-wave UV. These properties are consistent with those previously reported for variscite and slightly different from those of the other minerals from the variscite and metavariscite groups (Palache et al., 1951).

Figure 4 presents a Raman spectrum of one sample, studied previously by XRD (see Litvinenko et al., 2013). The most intense apparent maxima is at approximately 1020 cm⁻¹, with two less intense peaks at around 990 and 1060 cm⁻¹, all due to PO_4 symmetric stretching vibrations of the minerals from the variscite and metavariscite groups (Frost et al., 2004; Onac et al., 2004). The most intense bands are due to variscite-stretching vibrations, but their exact position and shape are likely due to the presence of other minerals of the variscite and metavariscite groups, such as strengite and phosphosiderite. A series of less intense bands, the result of PO_4 bending modes, are observed at about 580, 430, and 220 cm⁻¹ (again, see Frost et al., 2004; Onac et al., 2004). Higher luminescence is observed in the green portion of the spectrum (figure 4). Quartz was also occasionally identified.
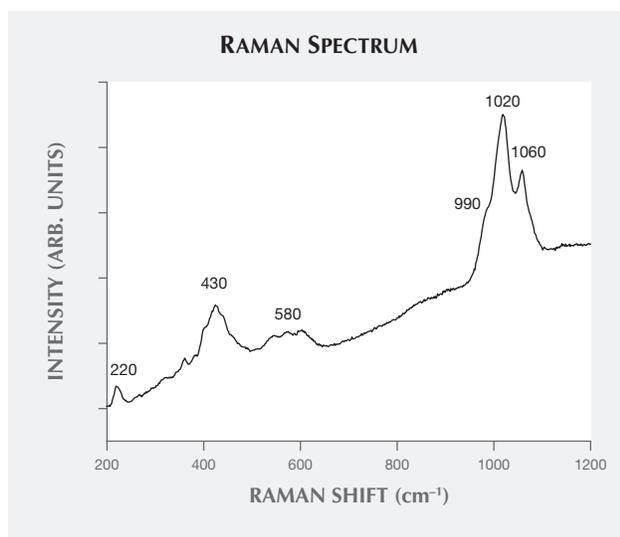
RAMAN SPECTRUM

Figure 4. The Raman spectrum of sample 5 is in the 200–1200 cm⁻¹ range. The most intense apparent maxima is at about 1020 cm⁻¹. The less intense peaks at around 990 and 1060 cm⁻¹ are due to PO_4 stretching vibrations in variscite and other minerals of the variscite and metavariscite groups. The bands at around 580, 430, and 220 cm⁻¹ are the result of PO_4 bending modes.

REFLECTANCE SPECTRA

Figure 5. Reflectance spectra of the green and bluish green areas of sample 5 in the 380–1080 nm range. The strong decrease in reflectance at around 425 nm is probably related to iron. Bands at 445 and 630 nm, along with the weak but sharp decreases at about 645 and 690 nm, are related to chromium. The peak at 750 nm is most likely due to vanadyl groups, while the one at 975 nm is related to overtone vibrations of OH in the structural water. The relative intensity of the iron- and chromium-related bands is higher on the bluish green part than on the green area.

Chemical analysis using EDS on areas with various colors is presented in table 2. The chromophores Cr, V, and Fe were identified, along with small amounts of CaO, Na_2O, K_2O, TiO_2, SO_3, and As_2O_5. The atypical presence of SO_3 and As_2O_5 is likely due to the site's proximity to the Chorroha antimony deposit, with stibnite (Sb_2S_3) and arsenopyrite (FeAsS) as main minerals. A variscite occurrence that cut through antimony rocks was found in 1905 in the north-central

TABLE 1. Gemological features of variscite samples from central Tajikistan.

Sample no.	1	2	3	4	5	6
Photo						
Color	White to light blue to green	Bluish green with green areas	Light green to green	White to light blue to green	White to light blue to green	White to light blue to green
Size (cm)	1.5 × 1.0 × 0.4	2.3 × 1.5 × 1.2	1.6 × 1.0 × 0.5	1.5 × 1.2 × 1.0	1.3 × 1.2 × 0.5	1.0 × 0.9 × 0.5
Transparency	Opaque in hand samples, translucent in thin sections					
Luster	Waxy					
Fracturing	Conchoidal					
Microhardness	231.5–386.7 kg/mm² (4–5 Mohs hardness), with bright green areas the hardest and bluish white areas the softest					
Specific gravity	2.32–2.36					
Fluorescence	Inert to both long- and short-wave UV					

Oxides (wt.%)	Central Tajikistan (points from samples 2, 4, and 6)							Woodlands, Australia (Willing et al., 2008)	Ervedosa, Portugal	Pannecé, France (Calas et al., 2005)	Sardinia, Italy	Utah, U.S.A.
	Slightly green		White with green hue	Bluish green		Bright green						
	4 points	σ	1 point	3 points	σ	2 points	σ					
Al_2O_3	21.17–28.58 (25.68)	3.38	27.05	24.99–27.05 (25.91)	1.05	24.46–26.97 (25.72)	1.77	30.6–32.1 (31.45)	29.4	29.1	28.2	29.3
P_2O_5	41.95–45.59 (43.61)	1.64	44.47	42.64–44.29 (43.63)	0.87	42.43–43.08 (42.76)	0.45	44.4–45.9 (45.3)	45.3	44.7	44.3	44.4
Fe_2O_3	4.98–15.29 (9.06)	4.25	5.99	6.81–10.47 (8.30)	1.92	7.42–11.37 (9.40)	2.79	1.08–1.86 (1.4)	1.50	0.15	2.00	0.05
CaO	bdl–0.50 (0.16)		bdl	bdl		bdl		bdl–0.19 (0.06)	–	–	–	–
Na_2O	bdl–0.11 (0.11)		0.18	bdl–0.12 (0.12)		bdl		0.08–0.19 (0.12)	–	–	–	–
K_2O	bdl		0.13	bdl		bdl–0.14		0.02–0.13 (0.06)	–	–	–	–
SiO_2	bdl		bdl	bdl		bdl		0.47–1.46 (0.87)	0.04	0.03	1.40	0.06
TiO_2	bdl–0.15 (0.15)		bdl	bdl		bdl		0.14–0.40 (0.29)	0.02	0.03	0.02	0.08
V_2O_3	bdl–0.15 (0.15)		0.16	0.10–0.19 (0.14)		bdl–0.19 (0.13)		0.32–0.50 (0.41)	0.11	0.40	0.40	0.64
Cr_2O_3	bdl–0.15 (0.11)		0.10	bdl–0.16 (0.16)		bdl–0.16 (0.16)		0.09–0.21 (0.16)	0.40	0.2	0.30	0.14
As_2O_5	0.34–0.56 (0.46)		0.29	0.19–0.42 (0.28)		0.38–0.71 (0.55)		–	–	–	–	–
PbO	bdl		bdl	bdl		bdl		bdl–0.08 (0.02)	–	–	–	–
MnO	–		–	–		–		–	0.03	0.05	0.02	0.03
SO_3	0.30–1.46 (0.76)	0.50	0.68	0.25–0.37 (0.32)	0.06	0.35–0.38 (0.36)	0.02	0.09–0.43 (0.23)	–	–	–	–
F	–		–	–		–		0.05–0.11 (0.08)	–	–	–	–
-O=2F	–	–	–	–	–	–	–	-0.02– -0.05 (-0.04)	–	–	–	–
H_2O[b]	22.8							17.2–21.9 (19.9)		22.8		
Total	102.1–103.67 (102.93)	0.64	101.85	99.61–103.83 (101.59)	2.12	101.3–102.65 (101.97)	0.96	98.42–101.89 (100.31)	99.6	97.46	99.45	97.5

[a] For Tajik and Australian variscite, minimum and maximum values are given, along with the average in parentheses.
[b] Water content for Tajik samples is calculated by stoichiometry of the structural formula for variscite H_2O = 22.81 wt.%.
Note: bdl = values below the detection limit by EDS. The detection limits for all measured oxides vary; approximate detection limits are 0.1 wt%.

part of Mexico's Querétaro state, though not directly associated with antimony minerals (White, 1947). Compared to variscite from other localities (Australia and the United States) and archaeological sites (Portugal, France, and Italy), the samples contained higher Fe_2O_3 (up to 15.29 wt.%) and generally lower V_2O_3 and Cr_2O_3 (again, see table 2). Higher amounts of iron could be caused by the presence of iron phosphates such as strengite ($FePO_4 \cdot 2H_2O$, orthorhombic) and minor amounts of phosphosiderite ($FePO_4 \cdot 2H_2O$, monoclinic). For some areas with greenish color, where the color is mostly due to ferrous iron content, Cr and V were below the EDS detection limit.
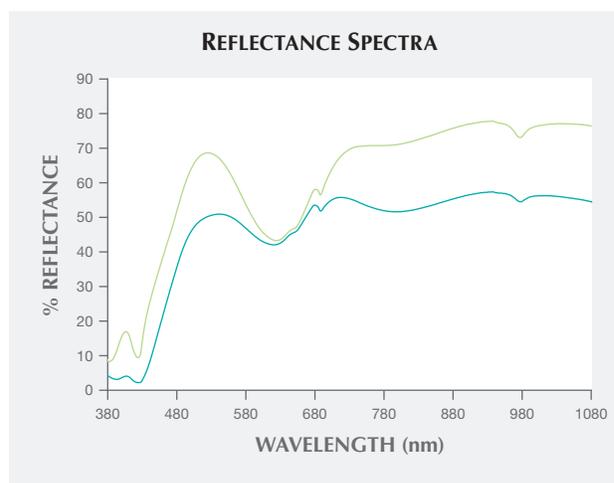
Figure 5 presents reflectance spectra of the green and bluish green areas from 380 to 1080 nm. The strong decrease in reflectance at around 425 nm is probably related to Fe^{3+}; the large weak band above 750 nm is likely due to vanadyl groups rather than Fe^{2+} (Calas et al., 2005). The decrease in reflectance centered at around 630 nm (and an associated, barely visible decrease in the blue part around 445 nm), as well as the additional weak sharp reflectance decreases at about 645 and 690 nm, are assigned to spin-forbidden transitions of Cr^{3+} (Calas et al., 2005). A gradual decrease of reflectance from the near-infrared through the visible region is also ob-

served in both spectra, though it is more pronounced in the bluish green samples. The relative intensity of the iron- and chromium-related bands is higher on the bluish green part than on the green (again, see figure 5). The sharp band at around 975 nm in the near-infrared region is related to overtone vibrations of OH in the structural water (again, see Calas et al., 2005).

CONCLUSIONS

Samples of variscite intergrown with strengite and minor amounts of other minerals of the variscite and metavariscite groups were found in central Tajikistan; these samples range from light blue to green and are suitable for cabochon cuts about 2 cm in length. Their gemological properties were similar to those of variscite from other occurrences. Raman spectroscopy confirmed the presence of variscite as well as other minerals of the variscite and metavariscite groups. Vis-NIR reflectance spectra showed that the color is principally due to relative concentrations of iron and chromium and that the vanadium plays a minor role. Chemical analysis shows generally high iron concentrations, probably due to the presence of strengite, as well as lower chromium and vanadium than variscite samples from other localities. Additionally, the relatively high arsenic and sulfur contents of the samples may be linked to the Chorroha antimony deposit. Further structural and spectroscopic studies as well as detailed geological mapping of this occurrence are needed in order to fully understand its production potential.

ABOUT THE AUTHORS
Dr. Litvinenko (litvinenko54@yandex.ru) is head of the gemology department at the Institute of Geology of Mineral Resources at the Russian State Geological Prospecting University in Moscow (MSGPU-RSGPU). Dr. Sorokina (elena.sorokina@gia.edu) is a postdoctoral research associate at GIA in Carlsbad, California, and a research fellow at the Fersman Mineralogical Museum, Russian Academy of Sciences (RAS) in Moscow. Dr. Karampelas is senior research gemologist at GRS (Gem Research Swisslab AG) in Adligenswil, Switzerland. At the time of the study, he was a research scientist at the Gübelin Gemmological Laboratory in Lucerne. Mr. Krivoschekov is a senior specialist at the Fe-dorovsky All-Russian Research Institute of Mineral Resources (FGUP VIMS) in Moscow. Mr. Serov is a researcher at the Gemmological Centre at Lomonosov State University, Moscow.

REFERENCES

Baratov R.B. (1976) *The Division of Stratified and Intrusive Formations in Tajikistan*. Donish Publishers, Dushanbe, Tajikistan, 268 pp. (in Russian).

Calas G., Galoisy L., Kiratisin A. (2005) The origin of the green color of variscite. *American Mineralogist*, Vol. 90, Nos. 5–6, pp. 984–990, http://dx.doi.org/10.2138/am.2005.1668

Fritz E., Rockwell K. (2006) Lab Notes: Variscite, resembling turquoise. *G&G*, Vol. 42, No. 1, p. 61.

Frost R.L., Weier M.L., Erickson K.L., Carmody O., Mills S.J. (2004) Raman spectroscopy of phosphates of the variscite mineral group. *Journal of Raman Spectroscopy*, Vol. 35, No. 12, pp. 1047–1055, http://dx.doi.org/10.1002/jrs.1251

Hyršl J. (2011) Gem News International: Variscite from Peru. *G&G*, Vol. 47, No. 3, p. 251.

Koivula J.I. (1986) Gem News: Metavariscite. *G&G*, Vol. 22, No. 4, pp. 247–248.

Larsen E.S. (1942) The mineralogy and paragenesis of the variscite nodules from near Fairfield, Utah. Part 3. *American Mineralogist*, Vol. 27, No. 6, pp. 441–451.

Litvinenko A.K., Sorokina E.S., Karampelas S., Iospa A.V., Krivoschekov N.N. (2013) Variscite and strengite of central Tajikistan – first finding. *Izvestiya Vysshikh Uchebnykh Zavedeniy, Geologiya i Razvedka (Proceedings of Higher Education Institutions, Geology and Prospecting)*, No. 3, pp. 73–76 [in Russian].

Middleton A., La Niece S., Ambers J., Hook D., Hobbs R., Seddon G. (2007). An elusive stone: the use of variscite as a semi-precious stone. *British Museum Technical Research Bulletin*, Vol. 1, pp. 29–34.

Onac B.P., Kearns J., Breban R., Panzaru S.C. (2004) Variscite (AlPO$_4$:2H$_2$O) from Cioclovina cave (Sureanu Mountains, Romania): A tale of a missing phosphate. *Studia Universitatis Babes-Bolyai Geologia*, Vol. 49, No. 1, pp. 3–14.

Palache C., Berman H., Frondel C. (1951) *Dana's System of Mineralogy*, Vol. II, 7th ed. John Wiley and Sons, Hoboken, New Jersey, pp. 756–761.

Querré G., Herbault F., Calligaro Th. (2007) Long distance transport of Neolithic variscite ornaments along the European Atlantic arc demonstrated by PIXE analysis. The XI International Conference on PIXE and Its Analytical Applications, Puebla, Mexico, pp. 38-1–38-4.

Solodova Yu.P., Andreenko E.D., Granadtchikova B.G. (1985) *The Determinant of Gem and Ornamental Stones*. Nedra Publishing, Moscow, 223 pp. [in Russian].

White D.E. (1947) Antimony deposits of the Soyatal district state of Queretaro, Mexico. *Geologic Investigation in the American Republics*, pp. 35–88, http://pubs.usgs.gov/bul/0960b/report.pdf.

Willing M., Stöcklmayer S., Wells M. (2008) Ornamental variscite: a new gemstone resource from Western Australia. *Journal of Gemmology*, Vol. 31, Nos. 3–4, pp. 111–124.

TAKE THE 2016 GEMS & GEMOLOGY CHALLENGE

The following 25 questions are from the Spring, Summer, Fall, and Winter 2015 issues of *Gems & Gemology*. Refer to the articles in those issues to find the single best answer for each question.

Mark your choice on the response card provided in this issue or visit gia.edu/gems-gemology to take the Challenge online. Entries must be received no later than **Friday, August 5, 2016**. All entries will be acknowledged with an e-mail, so please remember to include your name and e-mail address (and write clearly).

Score 75% or better, and you will receive a certificate of completion (PDF file). Earn a perfect score, and your name also will be listed in the Fall 2016 issue of *Gems & Gemology*.

1. The inclusion of iron preferentially along rhombohedral faces produces what effect in amethyst from the Boudi mine?
   A. Exclusively facet-grade material
   B. A deep purple color
   C. Double termination
   D. Hourglass zoning

2. When a gemstone has two transmission windows in the visible absorption spectrum, which of the following is true?
   A. It potentially exhibits both alexandrite and Usambara effects
   B. It is pleochroic
   C. It is idiochromatic
   D. It must contain more than one color-causing chromophore

3. Which is true of trapiche emeralds?
   A. They are examples of crystal twinning
   B. They are composite crystals
   C. They are single crystals
   D. They form when three crystals intersect

4. In origin determination employing IB-LDA, if one origin group has the highest cross-validation (CV) accuracy rate of all origin groups in a particular round, what is this called?
   A. Chosen group
   B. Optimal chosen group
   C. Omitted group
   D. Unseparated group

5. A corundum or quartz that displays dual-color double stars
   A. exhibits both a white dome star and a body-colored second star.
   B. has two sets of three series of needle inclusions in planes parallel to the basal face.
   C. has twinning in which each part of the twin has a set of needle inclusions, producing a single six-rayed star.
   D. contains abundant needle inclusions, resulting in an opaque stone with extremely sharp and strong stars.

6. Gold jewelry that is 99.9% pure
   A. is extremely rare, as it is too soft to stand up to regular use.
   B. can never tarnish, as gold is a noble metal that is highly stable in air.
   C. may show red, black, or brown spots if contaminated by silver.
   D. None of the above.

7. Compared to Kashmir sapphires, alluvial Montana sapphires are
   A. more saturated in color.
   B. more likely to display strong habit features.
   C. less transparent and more velvety.
   D. lower in Ti and higher in Fe.

8. Cobalt (Co^{2+}) in spinel produces a
   A. strong blue luminescence with 674 nm excitation.
   B. vivid blue color.
   C. blue color whose saturation is enhanced with the presence of Fe^{2+}.
   D. grayish color.

9. Of the following, the most prized attribute of black opal is
   A. white and crystal regions.
   B. dark gray potch.
   C. a red component in the play-of-color.
   D. shades of blue and green.

10. Today, the deposit that supplies the largest amount of ruby rough worldwide is
    A. Mogok, Myanmar
    B. Snezhnoe, Tajikistan
    C. Luc Yen, Vietnam
    D. Montepuez, Mozambique

11. The purpose of a cone crushing system in the diamond recovery process is to
   A. increase speed
   B. preserve larger stones
   C. reduce the need for pumps and conveyers
   D. reduce environmental impact

12. To capture all features in focus in an inclusion scene, a photomicrographer may employ
   A. increased exposure time
   B. oblique fiber-optic illumination
   C. extended depth-of-field imaging
   D. darkfield illumination

13. What type of jewelry represents a happy marriage in Chinese culture?
   A. Gold and jade
   B. Platinum
   C. 24K gold
   D. Chrysanthemum-themed jewelry

14. Which of the following statements about HPHT synthetic diamonds is true?
   A. Faceted samples over a carat, with IF clarity and D color, have been achieved.
   B. They are all type IIb.
   C. They have not yet matched CVD synthetic diamonds in color and carat size.
   D. Growth rates for colorless samples are higher than for fancy-color blue and yellow samples.

15. Which is not true about nitrogen in diamonds?
   A. In combination with a GR1 defect, it generates a green color.
   B. It only results in broad spectral absorption features.
   C. Its presence results in absorption at the blue end of the visible spectrum.
   D. It is the most common impurity element.

16. While photographing an internal feature, contrast can be optimized to capture maximum detail by
   A. high dynamic range imaging.
   B. placing a black strip between the gem and the light source to create a shadowing environment.
   C. using brightfield illumination.
   D. A and B

17. The Grand Sapphire's distinctive lozenge shape can be attributed to
   A. the cut it received prior to acquisition by Louis XIV.
   B. its natural habit.
   C. a cushion cut it received while owned by a Ruspoli prince.
   D. recutting from a Mogul cut.

18. If repolishing the dome of a dual-color double star sapphire results in a star disappearing, what must be true?
   A. Three series of acicular needles can be found throughout the stone.
   B. The base is highly polished.
   C. The body-colored star disappeared.
   D. The stone is diffusion treated.

19. The following statements about all sources of sapphire from Montana are true except
   A. Rutile is a common inclusion.
   B. All possible sapphire colors are found.
   C. Color enhancement with heat treatment is common for all deposits.
   D. They are found in the western half of the state.

20. What distinguishes color change from color variation in a gemstone?
   A. Color change occurs when the hue angle difference in two different lighting sources exceeds 10°.
   B. An absolute classification scheme does not exist.
   C. Color change can be distinguished from color variation based on the size of the stone.
   D. Color change occurs when the color difference in two different light sources exceeds a value of nine.

21. Most blue spinel produced in the Luc Yen district comes from
   A. primary pargasite deposits containing fractured, irregularly shaped crystals
   B. primary marble deposits containing well-formed octahedral crystals
   C. primary aggregates of small octahedral crystals
   D. secondary deposits as a by-product

22. Why is it easier to eliminate blue color than yellow color during HPHT synthetic diamond growth?
   A. Nitrogen is present to some degree in any process gases and therefore finds its way into the growth capsule.
   B. Boron is heavier than nitrogen.
   C. It is impossible to incorporate boron into the diamond lattice.
   D. Nitrogen must exceed 100 ppm in diamond to generate visible color.

23. Which feature is unique to ruby from the Snezhnoe deposit?
   A. Lower than normal SG
   B. Unusually high RI
   C. Inclusions consisting of flakes of blue mica
   D. A complete lack of twinning with regular morphology and sharp faces

24. Lattice windows are an example of
   A. a faceting design element.
   B. a traditional Chinese design element.
   C. outlines of crystalline lattice features.
   D. transparent faces of rough diamonds.

25. How does the formation of the overgrowth zone of trapiche emeralds differ from the growth of non-trapiche emeralds?
   A. There is no difference.
   B. It forms much faster.
   C. It forms much slower.
   D. It necessarily incorporates organic material.

G&G Lab Notes

Editors
Thomas M. Moses | Shane F. McClure

Unusual COLORED STONES

Recently, a parcel of approximately 40 rare gemstones was submitted to GIA's Carlsbad laboratory for identification. Six of these stones (figure 1) represented gem types that had never been examined at this location. They were identified using standard gemological testing, Raman spectroscopy, and energy-dispersive X-ray fluorescence (EDXRF).

A 0.87 ct translucent green hexagonal step cut was identified as adamite, $Zn_2(AsO_4)(OH)$. It had a specific gravity (SG) of 4.40 and a refractive index (RI) of 1.721–1.750. The stone fluoresced weak green under long-wave UV light but was inert to short-wave UV, which is atypical of adamite. Clouds and fractures were observed with 30× magnification.

A translucent brown trapezoidal step cut with an SG of 5.18 proved to be bahianite, $Al_5SbO_{14}(OH)_2$, which is especially rare as a facet-grade gemstone. The 0.73 ct bahianite had a refractive index over the limit (OTL) of the RI liquid. It was inert under long-wave UV light but displayed very weak blue under short-wave UV light. Large fractures, along with numerous whitish fibrous, radial, and granular inclusions and some surface-breaking opaque metallic inclusions,

Figure 1. These rare gemstones were recently examined at GIA's Carlsbad laboratory. From left to right: a 0.87 ct green adamite, a 0.73 ct brown bahianite, a 42.08 ct light brownish yellow cerussite, a 0.33 ct purple chambersite, a 2.45 ct orange olmiite, and a 1.30 ct color-change remondite.

were visible using 30× magnification. It also displayed vitreous to subadamantine luster.

A 42.08 ct transparent light brownish yellow octagonal mixed-cut specimen with an SG of 6.54 displayed an OTL refractive index and a biaxial optic figure, indicating its doubly refractive nature. It was inert to long-wave UV light but fluoresced very weak yellow under short-wave UV light. Magnification revealed strong doubling, strong fire, and numerous growth tubes and needles. Its heft was high due to its lead content. These properties, along with advanced testing, led to its identification as cerussite, $PbCO_3$. Although cerussite is a common weathering product of lead ore minerals, its softness, brittleness, and heat sensitivity

make it a very rare faceted gem, particularly in this large size.

Another stone from the collection, a 0.33 ct transparent to semitransparent purple triangle step cut with an SG of 3.49 and an RI of 1.728–1.734, was determined to be chambersite, $Mn_3B_7O_{13}Cl$. The gem was inert to both long- and short-wave UV light and showed numerous clouds with 30× magnification. Chambersite is an extremely rare mineral, found as deep as 70 feet in salt brines (J.E. Arem, "Chambersite," *The Color Encyclopedia of Gemstones*, 1987, 2nd ed., p. 65). Because it is so small and dark, this material is almost never faceted.

A 2.45 ct semitransparent orange cushion modified brilliant was identified as olmiite, $CaMn[SiO_3(OH)](OH)$, which was first discovered in 2006 in

South Africa (http://www.mindat.org/min-30762.html). Its SG was 2.95. The stone was doubly refractive, displayed an RI of 1.648–1.671, and fluoresced very weak orangy red under both long- and short-wave UV light. Magnification revealed wavy graining, fibrous dislocations and inclusions, and a slightly oxidized stone surface. Most olmiite crystals are not suitable for faceting.

The final stone of the six, a transparent pear-shaped modified brilliant that changed from greenish yellow under fluorescent light to yellowish orange under incandescent light, was identified as color-change remondite, $Na_3(Ce,La,Ca,Na,Sr)_3(CO_3)_5$. The 1.30 ct stone had an SG of 3.40 and showed an RI of 1.628–1.631, yielding a birefringence of only 0.003. It was inert to both long- and short-wave UV light. Handheld prism spectroscopy revealed a strong rare earth element spectrum. Large growth tubes, scattered particles, and etch channels were observed with 30× magnification. The stone's rounded facet junctions indicated a low hardness. Remondite was previously reported as a color-change burbankite-related mineral from Quebec (Winter 1992 GNI, pp. 270–271).

Such a suite of gemstones, prized among avid gem collectors, is not often submitted to the laboratory. Without the help of advanced analytical equipment such as Raman spectroscopy and EDXRF to complement standard gemological testing, it would be challenging to conclude the identity of these rare gemstones.

Rebecca Tsang

DIAMOND
Inclusion with Radiation Halo

Radiation is known to impart green or brown coloration to diamond. This effect most commonly appears as colored spots, presumably where radioactive mineral grains settled against the diamond for an extended period. Circulation of radioactive groundwater may contribute to a "skin" with more evenly distributed color. In either case, the radiation
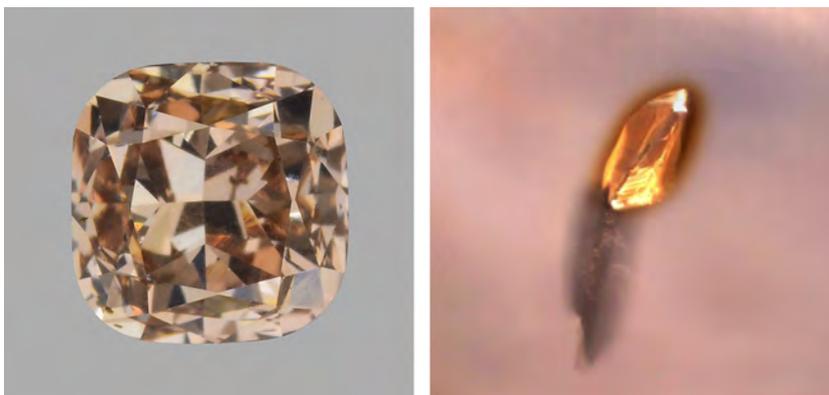
Figure 2. Left: This 0.49 ct Fancy pink brown diamond, measuring 4.11 mm wide, contains a monazite inclusion with a brown radiation halo. Right: A photomicrograph of the monazite inclusion shows the halo thickness of about 10–20 μm. The inclusion's color is masked by the brown radiation stain, but it appears to be yellow or colorless. The dark feature extending from the bottom of the inclusion is a graphitized crack. Field of view 0.36 mm.

comes from an external source. GIA's New York lab recently examined a 0.49 ct Fancy pink brown diamond containing an inclusion with a brown radiation stain in the form of a halo (figure 2). In this case, the radiation originated from the inclusion itself.

Because the inclusion is completely enclosed within the diamond, the material must have been trapped during diamond growth in the mantle. Raman spectroscopy (figure 3) revealed the inclusion to be monazite, $(Ce,La,Nd,Th)PO_4$, a mineral capable of carrying significant amounts of radioactive thorium. Xenotime, YPO_4, a similar rare earth phosphate, has also been reported as an inclusion in diamond with a radiation stain (Fall 2014 Lab Notes, pp. 237–238), but that in-

Figure 3. A Raman spectrum of the inclusion with a radiation halo shows a strong peak at 972 cm^{-1} and smaller peaks at 575 and 415 cm^{-1}, all of which correspond to monazite.
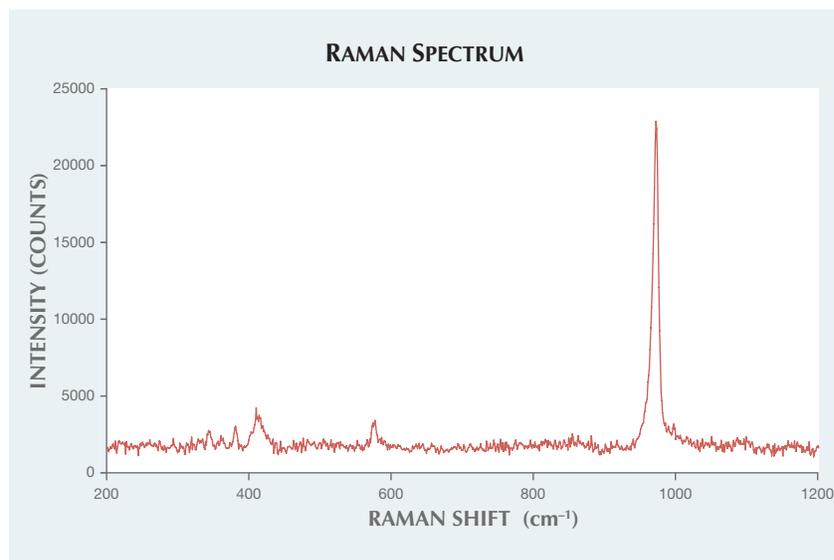
clusion was interpreted as epigenetic.

Monazite is very rarely reported as an inclusion in diamond. It is not part of the common mineral assemblage of peridotitic or eclogitic mantle host rocks. Instead, a rare earth element–enriched phosphate like monazite could be attributed to carbonatitic fluid or melt that infiltrated the host rocks and contributed to diamond growth. Monazite found within peridotite mantle xenoliths has also been ascribed to carbonatitic metasomatism (R.L. Rudnick et al., "Carbonatite metasomatism in the northern Tanzanian mantle: Petrographic and geochemical characteristics," *Earth and Planetary Science Letters*, Vol. 114, No. 4, 1993, pp. 463–475). Other phosphate minerals, chiefly apatite, can be found as a component of the fluid microinclusions that characterize so-called fibrous diamond. Diamond-forming fluids or melts are believed to be an important source of incompatible elements that may reenrich the otherwise depleted refractory lithospheric mantle.

Evan M. Smith and
Surjit Dillon Wong

Analysis of Yellow Diamond Melee for Color Treatment and Synthetics
Due to the size and quantity of diamond melee in a parcel, gemological analysis is usually not performed on each specimen. As a result, treated and synthetic diamonds are sometimes mixed with natural diamond melee in parcels (Winter 2014 Lab Notes, pp. 293–294).

Some gemological laboratories are able to properly identify treated and synthetic diamond melee with a combination of infrared absorption spectroscopy, photoluminescence (PL) spectroscopy, and DiamondView fluorescence imaging. GIA's New York laboratory recently tested two parcels of yellow diamond melee submitted for this screening. The results of their examination highlight the importance of laboratory analysis to correctly establishing the nature and color origin of diamond melee.

A parcel of six yellow melee (figure 4), each weighing approximately 0.12 ct, was submitted to GIA for testing. Examination confirmed that all six were natural diamonds treated by HPHT (high-pressure, high-temperature) processing. A combination of mid-infrared absorption spectroscopy (4000–400 cm^{-1}) and PL spectroscopy with 633 nm laser excitation was used to detect this HPHT treatment. Spectroscopic analysis in the mid-IR range revealed the presence of isolated single nitrogen impurities. Four stones contained both A- and B-aggregated nitrogen where the B-aggregate was dominant, while the remaining two contained B-aggregated nitrogen; all six contained isolated single nitrogen. PL spectroscopy revealed features that confirmed these were HPHT-treated diamonds.

Another parcel of 20 yellow diamond melee (figure 5), each weighing

Figure 4. These six melee were revealed to be HPHT-treated natural diamonds.

between 0.01 and 0.02 ct, was submitted for testing. Mid-IR absorption spectroscopy and DiamondView imaging revealed that three were untreated natural diamonds and one was an HPHT-treated natural diamond; the rest were HPHT synthetics (figure 6). Mid-IR spectroscopy also revealed that 17 of the melee were dominated by A-aggregated nitrogen, three contained both A- and B-aggregated nitrogen, and all 20 contained isolated single nitrogen. The DiamondView images revealed characteristic growth features that helped separate the HPHT synthetic and HPHT-treated material from the natural stones. The HPHT synthetics contained typical cuboctahedral growth patterns, while growth patterns associated with natural diamond formation were observed in the natural diamonds, both untreated and HPHT-treated.

Figure 5. Of this group of 20 diamond melee, 16 were HPHT synthetics (left). Three were untreated natural diamonds (center), and one was an HPHT-treated natural diamond (right).
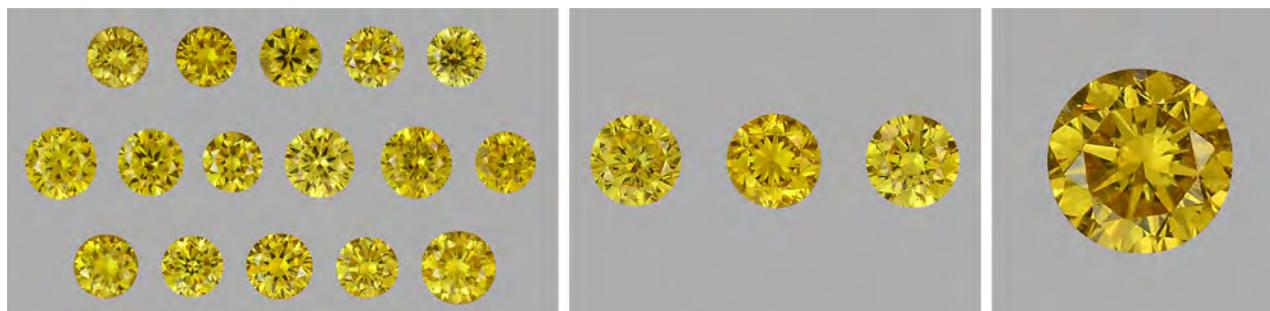
Figure 6. These DiamondView images show characteristic growth features typical of (A) untreated natural, (B) HPHT-treated natural, and (C–F) HPHT synthetic diamond.

Figure 7. This 1.81 ct specimen was a natural emerald/emerald doublet. Field of view 10.5 mm.

This analysis highlights the importance of laboratory testing to correctly identifying the nature and color origin of diamond melee, and to minimizing the risk of mixing treated and synthetic diamonds with natural melee in the marketplace.
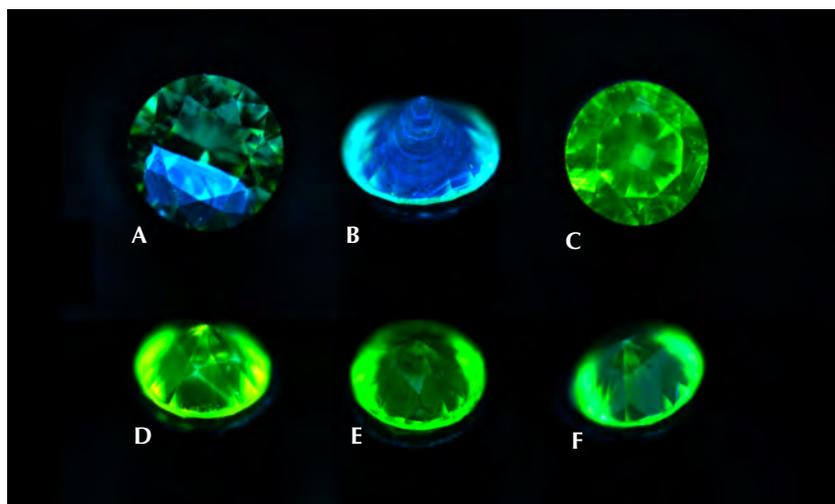
Caitlin Dieck, Manisha Bhoir, and Paul Johnson

EMERALD/Emerald Doublet

While various combinations of materials are used to form doublet gems, we seldom see doublets consisting of the same materials. Ruby/ruby doublets (Spring 1987 Lab Notes, pp. 47–48; Spring 1996 Lab Notes, p. 49) as well as a tourmaline/tourmaline doublet (Summer 1990 GNI, pp. 165–166) have been reported, but a doublet consisting of two sections of natural emerald has not been previously documented.

GIA's Tokyo laboratory recently examined a 1.81 ct transparent green octagonal step cut that measured approximately 7.22 × 6.71 × 5.55 mm (figure 7). Standard gemological testing indicated an SG of 2.71, with an RI of 1.572–1.580 on the crown and 1.570–1.578 on the pavilion. A chromium spectrum consistent with emerald was visible with a handheld spectroscope. Upon first glance, this stone appeared to be a natural Colombian emerald, but careful examination easily revealed its doublet nature, while Raman spectroscopy confirmed that both the top and bottom portions were indeed beryl.

Microscopic observation revealed a very flat separation plane below the girdle, crossing the pavilion diagonally. Flattened gas bubbles were visible along the plane (figure 8, left), and a blue and orange flash effect was also apparent. Jagged three-phase inclusions typical of Colombian emeralds were visible in both parts, while fine growth tubes and fingerprints in helix patterns were seen only in the top portion. Inclusions did not cross the boundary between the two sections. Under long-wave UV light, the top showed a stronger red fluorescence than the bottom, with a distinct boundary between the two (figure 8, right). A whitish fluorescence was also observed along the plane. Illumination using crossed polarizers revealed that the top and bottom portions had different optical orientations, with two optic axes visible (figure 9). Typical of most emeralds, enhanced fractures showing a flash effect were found in both parts.

Immersion with methylene iodide revealed green angular zoning in the bottom, whereas the top had even, saturated green color. Both sections appeared to have enough green color to be considered emerald. The glue along the separation plane was color-

Figure 8. Left: Flattened gas bubbles are visible along the separation plane of the doublet. Field of view approximately 3 mm. Right: Viewed under long-wave UV light, the doublet displayed strong red fluorescence in the top portion but not the bottom. A distinct boundary between the two parts is clearly visible.
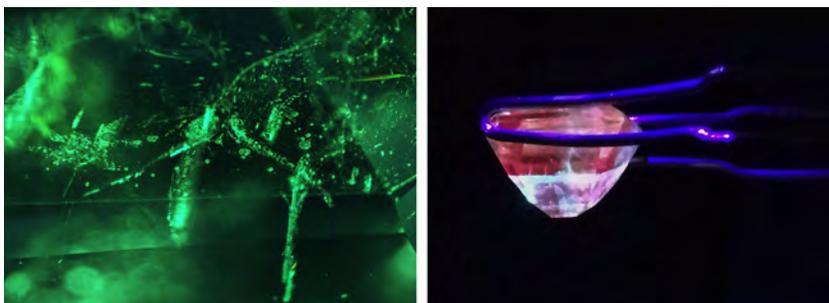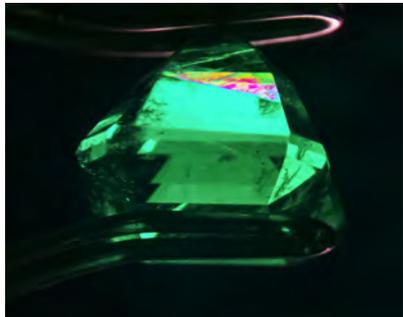
Figure 9. When the doublet was viewed under crossed polarizers, different optical orientations were apparent. At this angle, interference colors along the optic axis are clearly visible in the bottom portion but not the top. Field of view 11.60 mm.

Figure 10. Top: These five opal slices of comparable thickness were cut from the same rough. They were semitransparent to translucent when viewed in daylight on a black background. Play-of-color was displayed with oblique lighting at certain angles. Bottom: The slices' transparency improved after immersion in distilled water for approximately 20–30 minutes. Each slice absorbed water differently depending on its porosity.

less. This is unusual, as assembled imitations of emerald are often composed of pale beryl or other colorless materials with a green cement layer. We could only speculate on the circumstances leading to the creation of this unusual doublet.

Yusuke Katsurada and Claire Ito

Hydrophane OPAL Treatments
Recently in GIA's Bangkok lab, an approximately 4 cm piece of rough hydrophane opal was fabricated into five slices for various treatment ex-periments. Each slice was approximately 0.5 cm thick. Only clean tap water was used in the cutting process, and no other materials besides opal were involved. The opal slices showed a whitish, cloudy appearance in daylight and appeared light brown to brown in calibrated diffused light.

After the cutting step, all five slices underwent specific gravity testing, which gave SG values of approximately 1.93 ±0.03. While immersed in water, the slices displayed obvious weight gain and improved transparency, which indicated that the material was hydrophane opal (figure 10).

TABLE 1. Appearance of hydrophane opal slices before and after treatment.

	Oil treatment		Opticon treatment	
	Before	After	Before	After
Daylight				
Calibrated transmitted light				
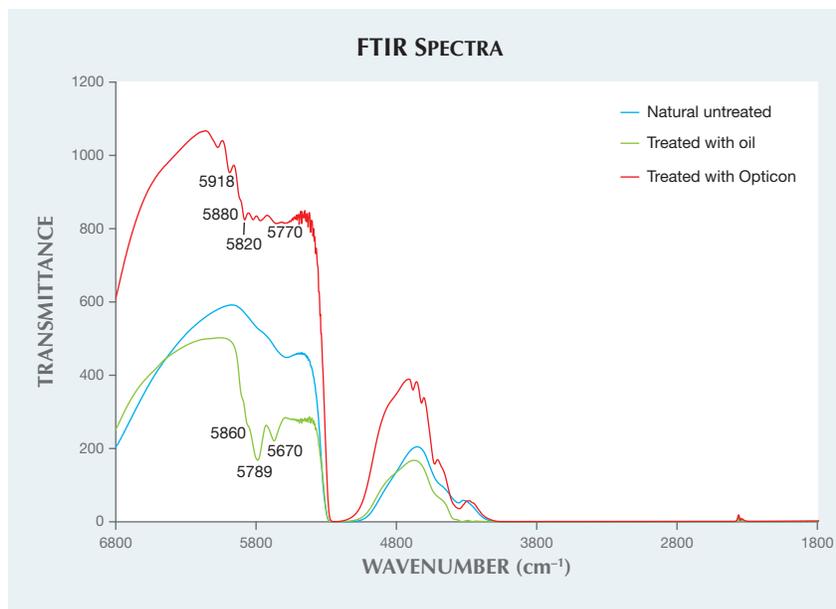
FTIR Spectra

Figure 11. FTIR spectra of untreated, oil-treated, and Opticon-treated opal. The two treated opals show characteristic FTIR peaks in the 5600–5900 cm⁻¹ range, while untreated opal does not show any peaks in this range.

The water-absorbing ability of the opal was found to vary through the whole piece, resulting from its non-uniform porosity, and could be calcu-

Figure 12. Raman spectra of untreated, oil-treated, and Opticon-treated opal. The oil-treated opal shows characteristic Raman peaks at 2929, 2897, 2873, 2851, and 2724 cm⁻¹. The Opticon-treated opal displays characteristic Raman peaks at 3071, 2931, and 2873 cm⁻¹, with a series of smaller peaks in the 600–1600 cm⁻¹ range.
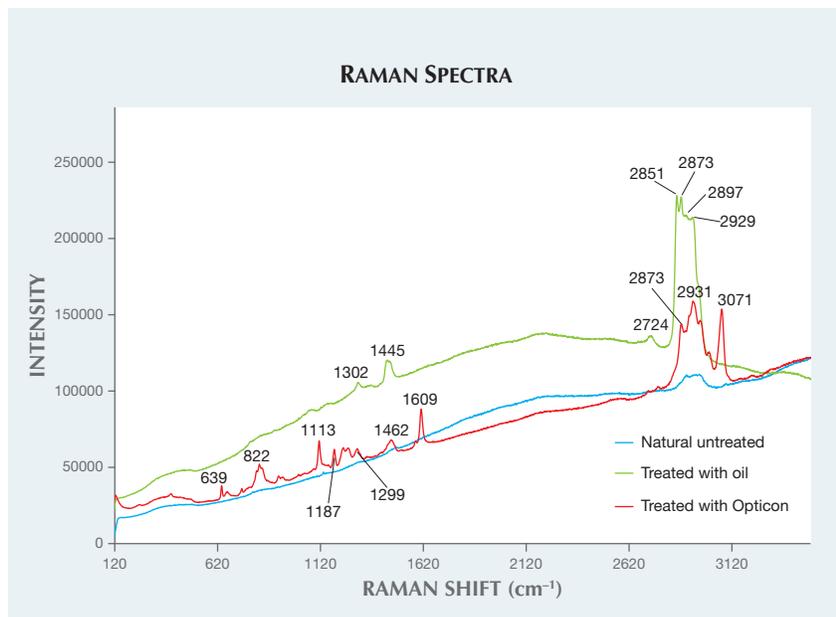
Raman Spectra

lated as percentage weight changes in water, ranging from 5% to 13%. It took approximately one week to restore the opal's original weight and appearance.

Two slices were then selected for oil and Opticon treatment experiments. The treatment procedures were identical. The pieces of opal were heated to approximately 80°C and then placed in warm oil or Opticon of the same temperature under vacuum conditions. They were heated continuously for 15 to 20 minutes, which was indicated by the presence of gas bubbles on the opal. Once the slices had fully absorbed the oil or Opticon, there were few, if any, gas bubbles. Afterward, the slices were removed, cleaned with a dry cloth, and left to air-dry overnight at room temperature.

Both treated opal slices were analyzed using a gemological microscope and advanced instruments. Oil treatment improved transparency but destroyed play-of-color (table 1, left). Opticon treatment enhanced transparency while preserving play-of-color (table 1, right). The FTIR spectrum of the oil-treated slice showed oil-related peaks at 5670, 5789, and 5860 cm⁻¹, whereas the FTIR spectrum of the Opticon-treated slice displayed a series of related peaks in the 5600–5900 cm⁻¹ range (figure 11). Raman spectra also demonstrated the presence of treatments. The oil-treated sample displayed peaks at 2929, 2897, 2873, 2851, and 2724 cm⁻¹, while the Opticon-treated slice showed dominant peaks at 3071, 2931, and 2873 cm⁻¹, and a series of smaller peaks in the 600–1600 cm⁻¹ range (figure 12).

While oil and Opticon are not easily observed with the unaided eye or even with a microscope, they are readily detected by advanced instruments. Using Opticon, the process could be combined with other treatments, such as dyeing or sugar-acid treatment, to improve the durability and transparency of opal.

*Ratima Suthiyuth and
Vararut Weeramonkhonlert*

Figure 13. A 5.03 ct Fancy Deep blue HPHT synthetic diamond was examined by GIA (left). Faint but sharp color zoning was observed (middle, field of view 4.77 mm), along with small metallic inclusions and a cavity at the girdle (right, field of view 2.19 mm).

SYNTHETIC DIAMOND
Largest Blue HPHT Synthetic

Recently, large colorless and near-colorless HPHT-grown diamonds by the Russian company NDT have been investigated, with sizes up to 5.11 ct (U. D'Haenens-Johansson et al., "Large colorless HPHT-grown synthetic gem diamonds from New Diamond Technology, Russia," Fall 2015 *G&G*, pp. 260–279; Spring 2015 *G&G* Lab Notes, pp. 65–66). The largest faceted colorless HPHT-grown synthetic diamond reported to date is a 10.02 ct E-color, VS$_1$-clarity specimen, reported by IGI Hong Kong in 2015. In January 2016, GIA's New York laboratory examined a 5.03 ct fancy-color HPHT-grown type IIb synthetic diamond (figure 13, left) produced by NDT, the largest faceted blue laboratory-grown diamond studied so far.

This emerald-cut synthetic diamond was color graded as Fancy Deep blue. This is a very attractive color with no other color component, a prized rarity among natural type IIb diamonds (the Blue Moon, for instance, was graded as Fancy Vivid blue). When viewed using a microscope, faint but sharp color zoning could be seen (figure 13, center), indicative of the uneven impurity incorporation of HPHT synthetic diamonds. No strain was observed under crossed polarizers, indicating a very low dislocation density, which is also characteristic of HPHT-grown diamonds. It had VS$_1$ clarity, with only very small metallic inclusions and a cavity observed at the girdle (figure 13, right). Fluorescence and phosphorescence images collected using a DiamondView instrument revealed the sample's cuboctahedral growth pattern (figure 14, left), another feature of HPHT synthetics. The long-lasting chalky blue phosphorescence was further analyzed using spectroscopy, and the emission was found to originate from two broad bands centered at approximately 500 and 575 nm (figure 14, right). These bands have previously been reported in NDT's type IIa and IIb HPHT synthetic diamonds (D'Haenens-Johansson et al., 2015).

Absorption spectroscopy for the mid-infrared region confirmed the sample was type IIb, with strong boron-related features at 1290, 2458, and 2800 cm^{-1}. The average bulk boron concentration was 0.82 to 1.12 ppm, calculated according to the equation $N_A - N_D = (1.00 \pm 0.15) \times H_{1290}$ ppm cm^{-3}, where N_A is acceptor concentration, N_D is donor concentration, and H_{1290} is peak height at 1290 cm^{-1} (A.T. Collins, "Determination of the boron concentration in diamond using optical spectroscopy," *Proceedings of the*

Figure 14. DiamondView images of fluorescence (top left), and phosphorescence (bottom left) revealed a cuboctahedral growth pattern, which is typical for HPHT-grown synthetic diamond. Phosphorescence spectra (right) show two peaks at approximately 500 and 575 nm, contributing a chalky blue color.

PHOSPHORESCENCE SPECTRA
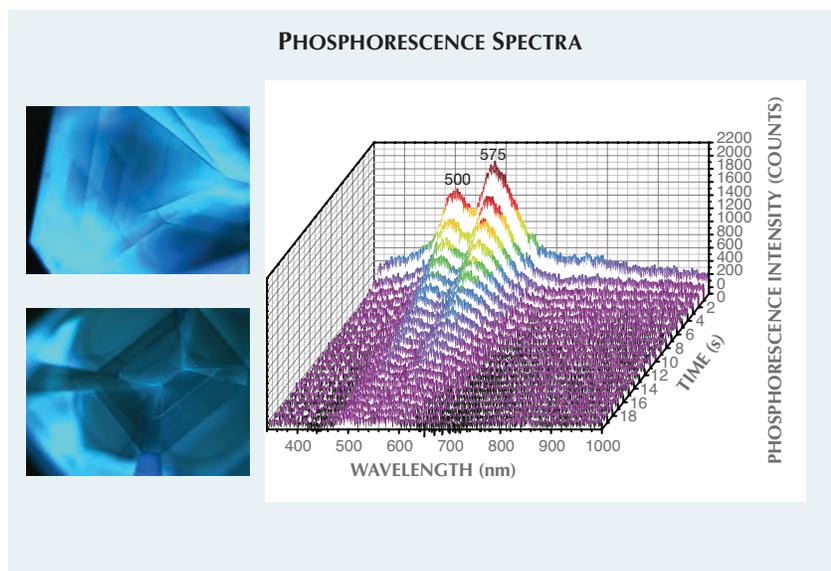
61st Diamond Conference, Warwick, UK, 2010). Otherwise, this large synthetic diamond exhibited an extremely low concentration of optical defects. PL spectroscopy was conducted at liquid nitrogen temperatures using a range of laser excitations covering the UV-visible-IR range. The PL spectra only revealed emission from a single defect species, a Ni-related emission multiplet with peaks at 483.6/483.8/484.1/484.4 nm (484 nm center) detected using 324.8 nm laser excitation (A.T. Collins, "The characterisation of point defects in diamond by luminescence spectroscopy," *Diamond and Related Materials*, Vol. 1, 1992, pp. 457–469). As with previous type IIb synthetic diamonds, its visible-NIR spectrum showed a transmission window in the blue region and an absorption in the red, caused by the presence of boron, resulting in the observed blue bodycolor.

This 5.03 ct sample is the largest HPHT-grown blue synthetic diamond examined at a GIA laboratory. As the size and quality of synthetic diamonds improve, careful identification is essential. Representative HPHT synthetic diamond characteristics seen in this specimen, such as the lack of tatami strain patterns (which are typically observed in natural type IIb diamonds), faint but sharp color zoning, and small metallic inclusions from the metal-catalyst flux, can be detected using a gemological microscope, emphasizing its continued importance in gem identification. Examination of this large IIb synthetic diamond, combined with those previously reported from NDT, illustrates the rapid progress in HPHT growth technologies. This is a development that will eventually impact the jewelry industry.

Kyaw Soe Moe, Paul Johnson, Ulrika D'Haenens-Johansson, and Wuyi Wang

Ring with a CVD Synthetic Melee
The separation of synthetic diamond melee from natural diamond melee is a significant concern. Some specimens

Figure 15. One of the round-cut melee mounted in this ring was identified as a CVD synthetic diamond.

have been identified by GIA and other laboratories as synthetic, but those products were predominantly HPHT grown. GIA's Hong Kong lab recently identified a CVD synthetic melee mounted in a ring (figure 15).

The round-cut synthetic measured approximately 2.8 mm in diameter and weighed about 0.08 ct. Color could not be graded due to the mounting, but it was estimated to be in the F-H range. The material showed no

notable visual features using the microscope other than a small surface scratch at the table. Infrared absorption spectroscopy indicated the typical features of a type IIa diamond; no defect-related absorption feature was detected. A PL spectrum was collected at liquid nitrogen temperature with a very wide range of laser excitation wavelengths. Major features included emissions from [N-V] and [Si-V]⁻ centers (figure 16). The emission at 575.0 nm from $[N-V]^0$ is much stronger than the peak at 637.1 nm from [N-V]⁻, similar to many natural type IIa diamonds. Most notably, this specimen showed very strong emissions at 736.6 and 736.9 nm from the [Si-V]⁻ defect. Using 514 nm laser excitation, the intensity of the [Si-V]⁻ defect was about eight times that of the diamond Raman line. DiamondView imaging revealed strong orange color with small irregular areas of blue fluorescence (figure 17). All these observations confirmed that this melee is an as-grown CVD synthetic.

This was the first mounted CVD synthetic melee diamond identified by GIA. While synthetics of this size

Figure 16. The photoluminescence spectrum collected at liquid nitrogen temperature with 514 nm laser excitation shows moderate emissions from [N-V] centers and a very strong emission from [Si-V]⁻.

PL SPECTRUM

Diamond Raman

736.6/736.9 [Si-V]⁻

575.0 $[N-V]^0$

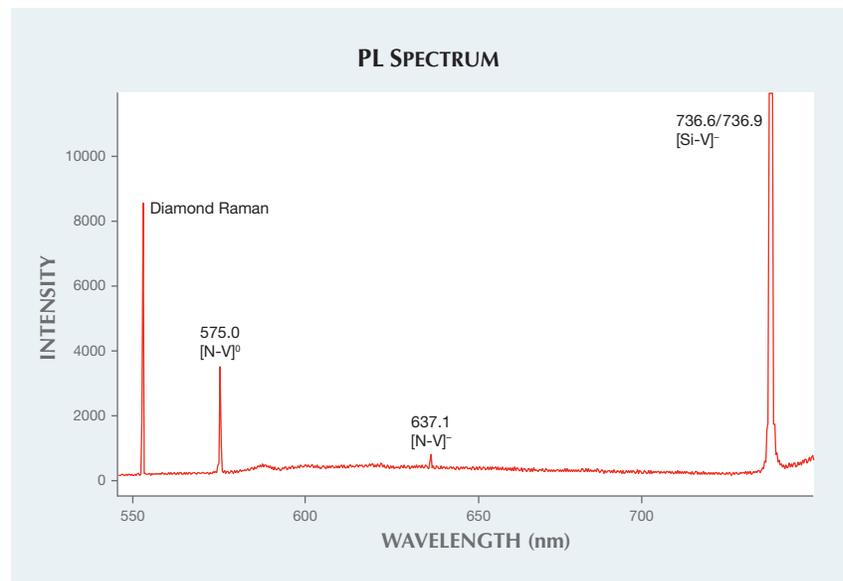637.1 [N-V]⁻

INTENSITY

WAVELENGTH (nm)

Figure 17. DiamondView imaging showed strong orange fluorescence with small irregular areas of blue fluorescence, a typical feature of as-grown CVD synthetic diamond.

Figure 18. A 9.75 ct synthetic spinel, seen in GIA's Bangkok lab, was proven to be treated by the quench-crackling method.

Figure 20. DiamondView imaging of the synthetic spinel showed fractures typical of quench-crackled material.

are overwhelmingly HPHT grown, we do expect to see more CVD synthetic diamond melee in the future.

Terry Poon, Carmen Lo, and Billie Law

Quench-Crackled Blue SYNTHETIC SPINEL

Recently, GIA's Bangkok laboratory examined an interesting 9.75 ct blue oval mixed cut (figure 18). Standard gemological properties included an RI of 1.728, with strong anomalous double refraction using the polariscope. The sample's Chelsea filter reaction exhibited a strong red transmission, and absorption bands at 540, 580, and 635 nm were seen in the handheld spectroscope. The specimen fluoresced strong red under long-wave UV radiation and strong bluish white under short-wave UV. These properties are diagnostic features of cobalt blue synthetic spinel grown by the Verneuil (flame-fusion) process.

Microscopic observation revealed tiny strings of gas bubbles and strong irregular graining, with many reflective fractures on one side of the sample (figure 19). The specimen appeared

to have been heated and thermally shocked. This method, known as quench-crackling, typically involves the use of a dye to create a preferable color, but not in this specimen. While DiamondView imaging showed clear fractures similar to those found in quench-crackled treated material (figure 20), a PL spectrum of Cr^{3+} shifted from 685 to 689 nm was consistent with synthetic spinel (S. Saeseaw et al., "Distinguishing heated spinels from unheated natural spinels and from synthetic spinels," GIA Research News, April 2009).

Laser ablation–inductively coupled

Figure 19. These reflective fractures were seen in the blue synthetic spinel. Field of view 2.5 mm.

plasma–mass spectrometry (LA-ICP-MS) was utilized for a trace element analysis. The results displayed high amounts of Co (up to 167 ppma), along with 1137 ppma Ti and 337 ppma Cr. Zn was found with a maximum of 6 ppma, and Ga was below the detection limit. This specimen contained higher amounts of Ti and Co than those previously reported in S. Saeseaw et al. ("Cobalt diffusion of natural spinel: A report describing a new treatment on the gem market," GIA Research News, June 2015). We concluded that a quench-crackling technique was used to make the synthetic spinel appear more like a natural spinel. In such cases, standard gemological properties are useful for accurate identification.

Sudarat Saeseaw and Charuwan Khowpong

Dolomite with Unusual Inclusions

Dolomite is not often encountered as a gem material, and it is generally known as an inclusion in gems such as emerald, garnet, quartz, and ruby. In view of this, any inclusions found within gem-quality dolomite may be justifiably considered as rare inclusion/host combinations.

One particular area known to produce gemmy dolomite suitable for lapidary work is the Mount Brussilof mine in Radium Hot Springs, British Columbia, Canada. Also found at this mine in direct association with the dolomite are crystals of the relatively rare mineral svanbergite.

Crystallizing in the trigonal crystal system in a rhombohedral to pseudocubic habit, svanbergite is not a widely known mineral associate of dolomite or any of the other common carbonates. It is a member of the beudantite mineral group and is composed of basic phosphate and sulfate of strontium and aluminum phosphates and sulfates. Svanbergite colors range from reddish brown to orange; there is also colorless material.
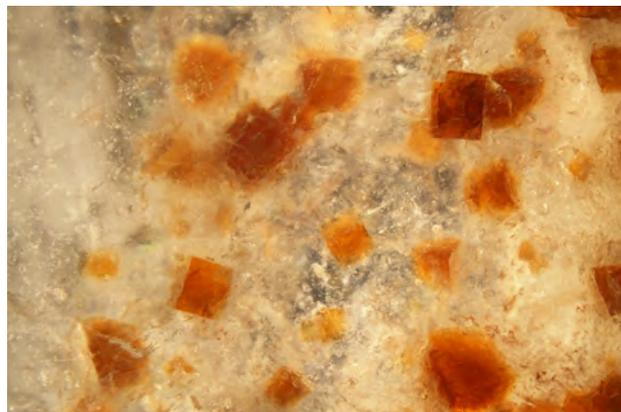
Figure 1. These brownish orange cubic to rhomb-shaped inclusions were identified by Raman analysis as svanbergite in dolomite. Photomicrograph by Jonathan Muyal; field of view 14.52 mm.

Recently we had the opportunity to examine a cluster of inclusions surrounded by numerous tiny fluid inclusions within a colorless gem-quality dolomite (figure 1). It came as a delightful surprise when laser Raman microspectrometry revealed these crystals to be svanbergite, an inclusion-to-host pairing we've never previously encountered.

John I. Koivula
GIA, Carlsbad

Olivine in Oregon Labradorite

Gem-quality labradorite from Oregon is typically prized for its red, orange, and green colors, as well as the tiny exsolution platelets of copper that create the phenomenon of aventurescence. Other notable inclusions can also be found in this gemstone from time to time, such as the olivine inclusion in the stone provided by Ken Lack of Gem Net LLC in Grants Pass, Oregon (figure 2). These rare inclusions typically display a greenish yellow bodycolor and compression cracks, indicating a significant amount of strain between the feldspar host and the olivine guest (figure 3; see E.J. Gübelin and J.I. Koivula, *Photoatlas of Inclusions in Gemstones*, Vol. 2, Opinio Verlag, Basel, Switzerland, 2005, pp. 419, 422). In this example, the stone was reported to have cracked during cutting, presumably due to the strain. This labradorite was cut to showcase the inclusion, making it easy to view from multiple angles.

Figure 2. This octagonal step-cut labradorite (left) was faceted with an extra-large girdle and a simple faceting pattern to showcase the olivine inclusion trapped inside (right). Photos by Kevin Schumacher.

Olivine inclusions in labradorite feldspar typically indicate an Oregon origin—if one is lucky enough to find such a rare internal feature.

Nathan Renfro
GIA, Carlsbad

Shrinkage "Footprint" in Rose Quartz

Rose quartz is a widely distributed gem material. The specimen shown in figure 4 was mined from pegmatites near the village of Tsaramanga, located in the Antananarivo province of Madagascar, and fashioned into a 34.11 ct rectangular step cut. It featured decorative epigenetic iron-colored debris that had been deposited in an extensive surface-reaching fracture. One of these debris patterns vividly calls to mind a dinosaur footprint left behind in soft mud.

It appears that the fine particulate debris was suspended in water and subsequently deposited in the crack as a wet solution. As the water dried, the resulting shrinkage pattern formed as only the particles were left behind, a mechanism very similar to the formation of water spots when raindrops dry on a smooth glassy surface. So now "footprints" joins "fingerprints" in our inclusion lexicon.

John I. Koivula

A Fantastic Display of Phase Changes in a Sapphire's Fluid Inclusion

In corundum of metamorphic origin, the presence of carbon dioxide (CO_2) fluid inclusions is a useful diagnostic indicator that no heat treatment has occurred; a gemologist simply has to cool the stone to below approximately 31.5°C to observe these inclusions (J.I. Koivula, "Carbon dioxide fluid inclusions as proof of natural-colored corundum," Fall 1986 *G&G*, pp. 152–155). Even though this type of inclusion is considered commonplace in sapphires that

Figure 3. The olivine inclusion was photographed in an immersion liquid, which wicked along surface-reaching cracks and partially eliminated the reflective interface, allowing better observation inside the olivine. Photomicrograph by Nathan Renfro; field of view 3.83 mm.
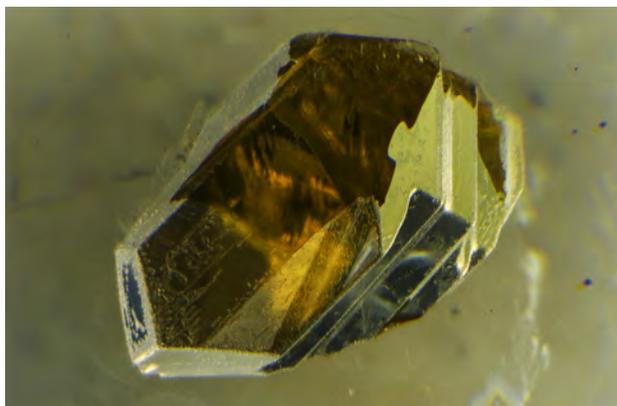

Figure 4. This 0.98 mm yellowish brown footprint-shaped epigenetic deposit of iron hydroxide was discovered in a pale pink rose quartz from Madagascar. Photomicrograph by Nathan Renfro; field of view 2.38 mm.
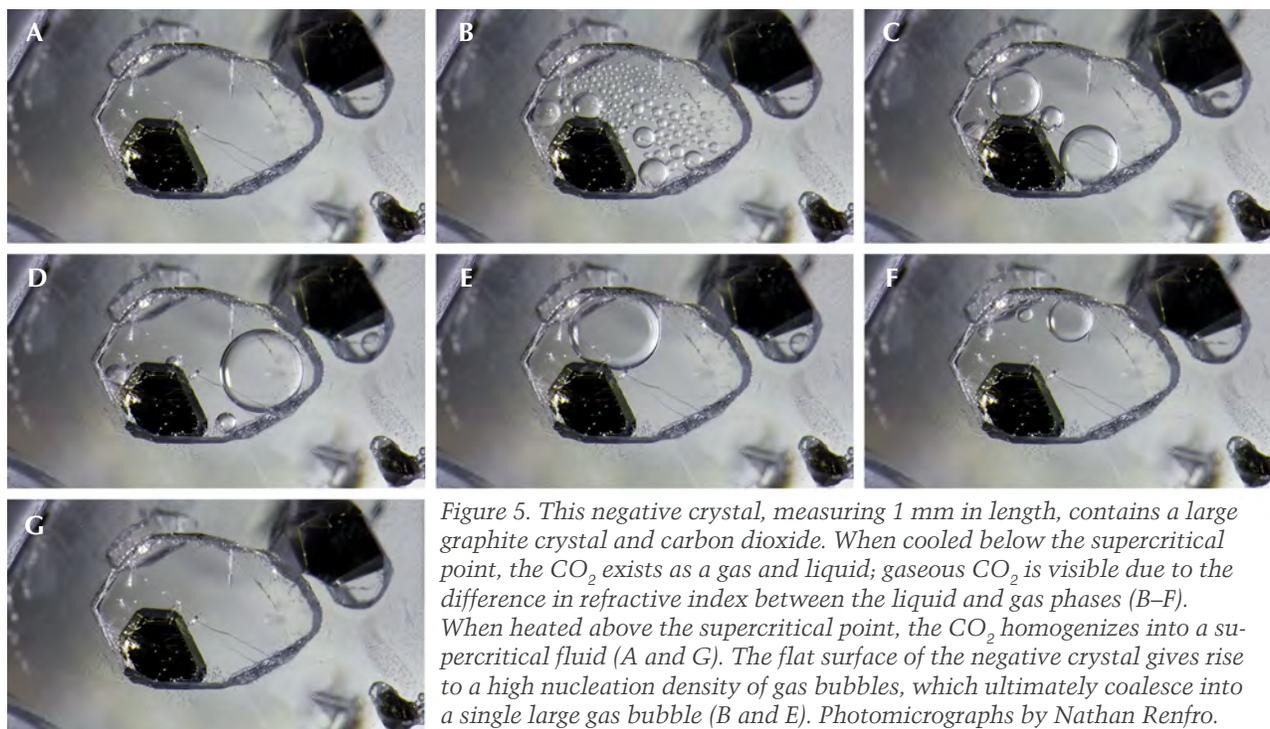
Figure 5. This negative crystal, measuring 1 mm in length, contains a large graphite crystal and carbon dioxide. When cooled below the supercritical point, the CO_2 exists as a gas and liquid; gaseous CO_2 is visible due to the difference in refractive index between the liquid and gas phases (B–F). When heated above the supercritical point, the CO_2 homogenizes into a supercritical fluid (A and G). The flat surface of the negative crystal gives rise to a high nucleation density of gas bubbles, which ultimately coalesce into a single large gas bubble (B and E). Photomicrographs by Nathan Renfro.

form in a metamorphic environment, a spectacular example was recently witnessed in a Sri Lankan sapphire.

When viewed correctly, the inclusion is revealed to be a negative crystal with a very tabular morphology (figure 5); for more on distinguishing negative crystals, see Fall 2009 Lab Notes, pp. 212–213. The negative crystal also contains a rather large graphite crystal. As the specimen's temperature is lowered, the CO_2 trapped in the negative crystal remains homogenized with no bubbles present until reaching approximately 31.5°C, whereupon both liquid and gas phases become clearly observable. The homogenized state represents a *supercritical* fluid, one that behaves like a liquid and a gas under certain conditions. Under these circumstances, the CO_2 assumes the shape of its "container" (the negative crystal) and can be compressed much like a gas phase while retaining the density of a liquid. This supercritical phase of CO_2 has some unique properties, such as the ability to dissolve certain substances, which is otherwise impossible in its gas or liquid phase. The observation of the phase change elegantly illustrates the temperature and pressure conditions of this fluid inclusion system (see video at gia.edu/gemsgemology/phase-changes-sapphire-fluid-inclusion). Such inclusions generate pressure 75 times that of sea level (>1000 psi), and this extreme pressure accounts for their tendency to rupture during heat treatment (see E. Roedder, *Fluid Inclusions*, Reviews in Mineralogy, Vol. 12, Mineralogical Society of America, Washington, DC, 1984).

When CO_2 is cooled below 31.5°C, the liquid and gas phases have very different densities and thus very different refractive indices, making them clearly distinguishable. Above that temperature, while in the supercritical state,

the homogenized liquid has a uniform density, and the two phases are impossible to differentiate. As one raises and lowers the temperature, the changing internal scene repeatedly follows this fascinating course.

In this example of a CO_2-filled negative crystal, numerous bubbles spontaneously nucleate as the temperature drops below the supercritical point. This proliferation is largely due to the flat, smooth surfaces of the tabular void. The highest-energy areas for the bubbles to nucleate exist on minute imperfections along these flat surfaces, creating an extraordinarily high nucleation density of gas bubbles. This is one of the most fantastic examples of a carbon dioxide fluid inclusion phenomenon the authors have encountered in sapphire.

Nathan Renfro and John Koivula

Elise A. Skalwold
Ithaca, New York

Iridescent Inclusions in Scapolite

A 2.21 ct phenomenal scapolite (figure 6), reportedly from Tanzania, was recently examined by this author. Of particular interest was its striking resemblance to Oregon labradorite feldspar, which displays aventurescence and is known in the trade as sunstone. Raman microspectrometry confirmed the stone's identity as scapolite. Vibrant thin-film iridescence created by brownish orange exsolution platelets (figure 7) was revealed by microscopic examination; these platelets are responsible for the stone's orange bodycolor. The exsolution platelets are presumed to be hematite based on their color, morphology, and high levels of iron detected
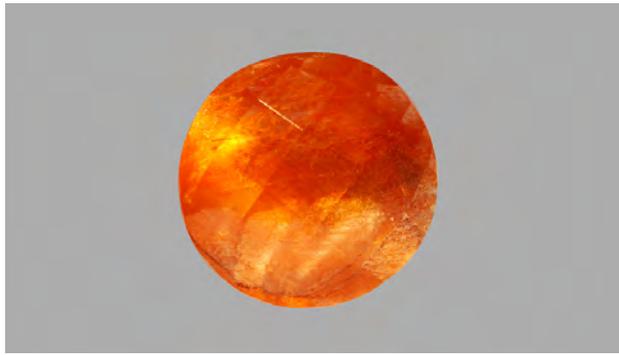
Figure 6. Orange platelet inclusions give this 2.21 ct scapolite an orange color and aventurescence similar to that of Oregon sunstone. Photo by Jonathan Muyal.

Figure 8. This 0.57 ct taaffeite from Sri Lanka measures 5.63 × 4.00 × 3.21 mm. Photo by Elise A. Skalwold.

by energy-dispersive X-ray fluorescence (EDXRF), although it was not possible to confirm this identity through Raman analysis. This scapolite's aventurescence and pleasing orange bodycolor make it an interesting collector's gemstone.

Jonathan Muyal
GIA, Carlsbad

A Halo in a Sri Lankan Taaffeite

The lovely chromium-bearing purplish red taaffeite from Sri Lanka seen in figure 8 is home to a swarm of included crystals, but one is particularly intriguing. Due to this crystal's depth and minute size, it cannot be conclusively identified without destructive testing. But its opaque black appearance leads us to believe it is either thorianite or uraninite. The latter is a uranium-rich mineral formerly known as pitchblende and reported to exist in taaffeites from this locality (see E.J. Gübelin and J.I. Koivula, *Photoatlas of Inclusions in Gemstones*, Volume 3, Opinio Verlag, Basel, Switzerland, 2008, pp. 649–650).

The strong alpha emissions from such mineral inclusions may lead to stress fractures in the host mineral. Unlike gamma and beta particles, alpha particles are massive and can cause considerable destruction in their path. In this case, it appears the gem has escaped fracturing: the effect is manifested as a concentric two-tiered halo surrounding the black crystal (figure 9). Its three-dimensional bulge-like appearance may be interpreted as radiation-induced distortions in the taaffeite's crystal structure. These distortions also locally changed the taaffeite's color, transparency, and refractive index and resulted in other strain features.

While the colorless inclusions display reflective surfaces in oblique light from the right, the haloed black inclusion does not. Instead there is a reflection-like scattering of light from the halo surrounding it. We suggest that this is due to a gradational difference in the taaffeite host's refractive index

Figure 9. In the taaffeite, a radiation-induced two-tiered halo surrounds a minute black crystal; the outer tier is subtle. The haloed crystal is most likely thorianite or uraninite, while numerous colorless zircon and apatite crystals are also present. Photomicrograph by John Koivula; field of view 0.75 mm.

Figure 7. Under magnification with oblique illumination, the platelet inclusions reveal vivid multicolor iridescence. Photomicrograph by Jonathan Muyal; field of view 1.42 mm.

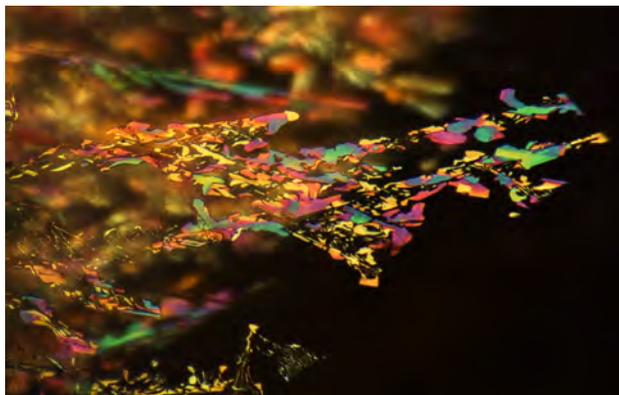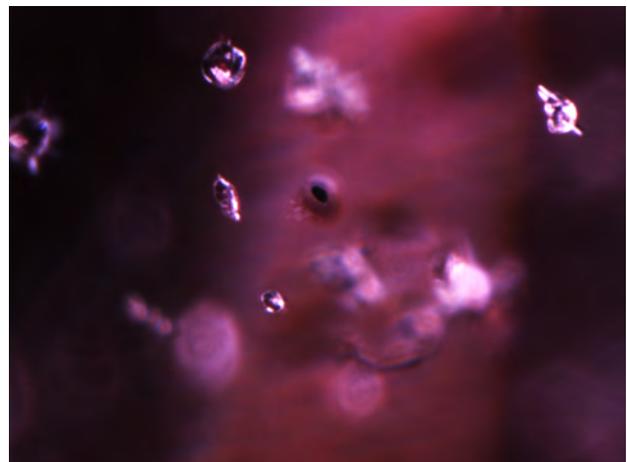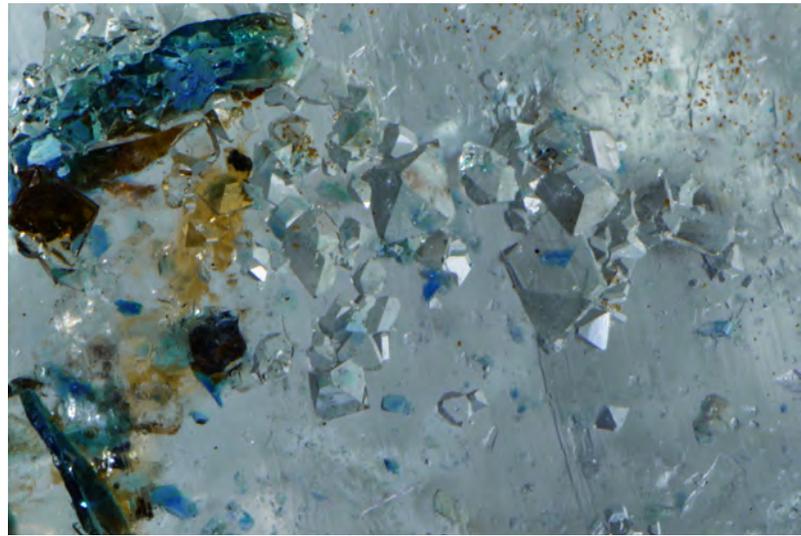farther from the black crystal as light is scattered off of the disrupted region. An everyday example of this comes from observing the sun before it rises above the horizon, an optical phenomenon that would not occur without the gradational refractive index of the atmosphere bending the light. The refractive index of the atmosphere decreases with altitude. Because light rays are bent toward the higher refractive index, we may surmise that the inclusion's halo has a lower refractive index than the rest of the taaffeite host. To support this explanation, in-depth exploration of the geometry of the halo's refractive index will be needed.

In the early days of radioactivity studies by scientists such as G.H. Henderson (in a series of five papers published between 1934 and 1939), these inclusions were known as "pleochroic halos." Although this term may be misleading, the halos' appearance is partially the result of localized changes in optical properties in the vicinity of the inclusion. Such inclusions are also relevant in determining the age of the planet by studying the characteristics and effects of radioactive guests in various minerals.

Elise A. Skalwold and William A. Bassett
Ithaca, New York

Figure 11. Inclusions of lazulite in this Canadian quartz were photographed using a partial immersion technique. A drop of mineral oil was placed on the surface to create a temporary window into the interior. Photomicrograph by Nathan Renfro; field of view 4.45 mm.

Figure 10. Recovered from Canada's Yukon Territory, these doubly terminated parallel-growth quartz crystals are decorated with deep blue crystals of lazulite. This specimen weighs 76.19 ct and measures 36.12 × 22.24 × 16.95 mm. Photo by Kevin Schumacher.

Quarterly Crystal: Quartz and Lazulite

Before a gemstone is fashioned by a lapidary, it enters the gem trade in its natural state, in a form generally referred to as "rough" or "gem rough." Not all rough is gem quality, nor is most so-called rough appropriate for fine mineral collections. Only a very special piece of rough is suitable for gem use or fits the visual definition of a fine mineral specimen. When such crystals are encountered it then becomes a difficult decision, often financially based, whether to leave them in a natural state or fashion them into polished gems.

Our new "Quarterly Crystal" section of the Micro-World column will feature very attractive inclusion-bearing minerals that could also be fashioned by a skilled lapidary into a gem or a polished inclusion study block. The quartz and lazulite specimen shown in figure 10 is one such mineral.

These parallel-growth, doubly terminated glassy quartz crystals were recovered from Rapid Creek in the Dawson mining district of Canada's Yukon Territory. While this is a nearly perfect mineral specimen, hosting swarms of deep blue lazulite crystals both on the surface and within (figure 11), it also makes a remarkable piece for any inclusionist's collection. Since this is a very uncommon mineral association from the locality, whether to polish it is a difficult decision. Fortunately, this dilemma can often be avoided with a simple trick: A small drop of mineral oil placed on the surface serves as a temporary window through which the inclusions may be observed and photographed.

John I. Koivula

TUCSON 2016

For decades, buyers and sellers from every aspect of the gem and jewelry industry have flocked to the gem fair in Tucson, a town in the heart of Arizona's Sonoran Desert that is rich in cultural and natural heritage. The annual shows are widely considered a forecast for the rest of the year. While the shows of the past few years have reflected a sluggish industry, the atmosphere in 2016 was dramatically different, with an increase in both attendance and business. The 34th AGTA GemFair saw record pre-registration numbers, and more than 300 exhibitors greeted a full house of buyers on the opening day. Gabrièl Mattice of Pala International (Fallbrook, California) said that sales were very strong this year, even on the first day of the show. The energized interaction between exhibitors and buyers was evident throughout the

Figure 1. Tucson's GJX show saw considerable traffic this year, including a higher number of American buyers. Photo by Andrew Lucas.

convention center. Though diamond sales have slowed, colored stones have gradually gained momentum among jewelry customers, and designers are responding in kind. Although the overall market share for colored stones is still small compared to the diamond sector, efforts to promote them have had very positive results.

More Serious Buyers. After the surge of foot traffic on the opening day, attendance remained stable at the shows for the rest of the week (figure 1). Vendors saw fewer Chinese buyers than in 2014, though Josh Saltzman of Nomad's Co. (New York) indicated that those who came were serious buyers picking up high-quality goods. Gaurav Shah from Real Gems Inc. (New York) confirmed that his company has seen greater demand for emerald in mainland China since 2007, a market that slowed in 2015. He said that the Chinese are more cautious and specific in their purchases, and he predicted an upswing in Chinese buying activity in the near future. Joseph Nakamura of Shogun Pearl (White Plains, New York) said that 95% of his customers were from the United States, while Gabrièl Mattice also saw many Europeans on the floor, especially French buyers. Many new buyers attended, possibly due to the stabilized prices and heightened interest in colored stones (figure 2). Mr. Shah observed three categories of clients in Tucson: buyers from television and Internet companies, retailers, and designers.

David Bindra of B&B Fine Gems (Los Angeles) noted that the number of transactions relative to the attendance was much higher than in previous years. He felt that this year's AGTA show was much better than the September 2015 Hong Kong Jewellery and Gem Fair, where many sellers felt the slowdown of the mainland Chinese market.

Figure 2. A customer examines some calibrated emeralds at the Real Gems booth in the AGTA show. Photo by Tao Hsu.

Figure 4. Morganite attracted many American buyers this year. Photo by Andrew Lucas.

Calibrated Goods. Though high-end colored gems continue to set auction records, the market for these stones remains slow. As a result, the colored stone trade still mainly consists of goods in standard calibrated sizes rather than custom-cut material (figure 3). Many cutting factories are able to provide a greater selection of sizes that fit their clients' requirements. This especially benefits the jewelry manufacturers in China and India, as setting calibrated gems is the bulk of their workload. Thus, mid-priced colored goods were the overall best sellers in Tucson. Nirmal Bardiya of RMC Gems (Bangkok) informed us that calibrated goods of various millimeter sizes are best sellers in the American market, while Arthur Groom Jr. of Eternity Natural Emerald (Ridgewood, New Jersey) noted that Afghan emerald melee is one of his biggest sellers. Guarav Shah reported that the most popular calibrated cuts are oval, emerald, and pear shapes; these goods generally range from $200–$2,000 per carat.

Classics. No single stone stole the show this year. Some relatively new varieties were available, but their potential is still hard to evaluate. Some people asked about the color-change pink pyrope garnet that has recently been covered by multiple trade magazines, including the Winter 2015 *G&G*. Ms. Mattice said it will take time to educate people about this stone, and it is not easy to predict the market potential. Mr. Bardiya informed us that morganite (figure 4), aquamarine, and blue topaz were popular among RMC's American clients. According to Joseph Nakamura, white pearls still dominate, while other colors come and go with different fashion trends. According to multiple dealers, Paraíba tourmaline is still in high demand (figure 5).

Even so, the "big three" of ruby, sapphire, and emerald still dominate the market and fetch higher prices, which was reflected in this year's shows. Corundum is still the most popular material in the high-end sector. David Bindra and Gabrièl Mattice both said that sapphires sold very well,

Figure 3. Assorted goods in calibrated sizes sold very well at the shows. Photo by Tao Hsu.

Figure 5. According to many exhibitors, Paraíba tourmaline remained one of the shows' best sellers. Photo by Andrew Lucas.

Figure 6. Colored stone jewelry is becoming increasingly popular among consumers, as designers such as Paula Crevoshay use colors in more creative ways. Photo by Tao Hsu.

and Mr. Bindra thinks that blue and green material will be especially strong this year, though yellow sapphires drew more interest than at previous shows. Pink and pastel-colored sapphires also attracted many buyers, perhaps because they evoke rose quartz and serenity blue, Pantone's colors of the year for 2016.

Interest and Demand for Color. As one of the best platforms to trade and promote colored gemstones, the Tucson shows provide buyers with the finest goods sourced from all over the world. Some one-of-a-kind stones debut here, such as the 332.24 ct Imperial topaz carving seen on pp. 88–89. Spectacular stones such as these usually attract immediate attention.

Mr. Bindra tied the increase in sales to a growing awareness of colored stones. Once-daunted consumers are becoming more knowledgeable about different varieties and are better prepared before they purchase. This interest in learning was reflected at the AGTA GemFair seminars, which saw a 30% increase in attendance.

Greater appreciation for colored stones motivates designers and retailers to source more of them (figure 6). Mr. Shah did business with more designers than in previous shows. The authors themselves saw materials in more unique cuts that seemed intended to capture the designers' imagination (figure 7). Mr. Shah said that even though Real Gems is a wholesaler, the company does not have a minimum order requirement for any buyers. This is very helpful for many designers, especially the young ones. This exhibitor feels that it is worthwhile to do business with people who are willing to work with and promote colored stones in their own work.

Summary. Based on their own observations, the authors were not surprised to hear vendors say that this was one of the strongest Tucson shows in recent history. People were encouraged by the renewed momentum of the American market, even though high-end buyers were still cautious. Relatively stable prices also contributed to increased sales, although the price of sapphire, ruby, and emerald remained high. With the positive forecast from Tucson, the trade is expecting a prosperous 2016.

We thank the many exhibitors who provided insight, photos, and materials.

Tao Hsu and Andrew Lucas
GIA, Carlsbad

Afghan emerald, Tajik ruby, and clarity-enhanced tourmaline. Eternity Natural Emerald (Ridgewood, New Jersey) exhibited a number of fascinating stones at the AGTA show. The emerald melee from Afghanistan (figure 8) immediately caught our attention. One of the authors was present in Afghanistan when Eternity's Arthur Groom ex-

Figure 7. Some pieces offered excellent options for designers who wish to create a unique look. Photo by Tao Hsu.
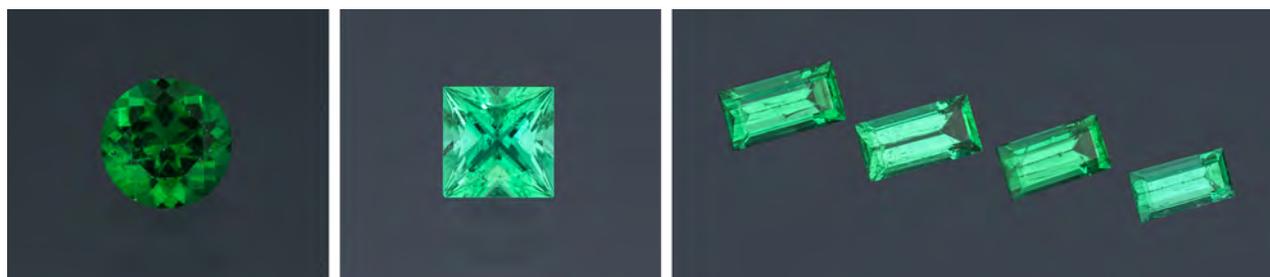
Figure 8. Left: Eternity Natural Emerald offered precision-cut Afghan emeralds, including "star" (left), princess (center), and baguette cuts (right, ranging from 6 × 3 mm to 5 × 2 mm). Photos by Robert Weldon/GIA, courtesy of Eternity Natural Emerald.

amined the original material (called "pencil rough" for its long and thin shape). The color was retained even when cut into small stones.

This rough is typically not treated, but a consistent supply of Afghan emerald is difficult to obtain. Prices are high, and negotiating is complex. Security concerns make it difficult to move rough in the country, and material is often smuggled to Dubai for the international market. To purchase the material, the company makes four to six buying trips a year, with permanent buyers located in Kabul and the Panjshir Valley. Much of the rough consists of the pencil crystals used for cutting precision melee. Once the pencil rough is sawn and preformed, the stones are cut for maximum brightness and the tightest measurement tolerances possible. All melee is cut in Sri Lanka.

The emeralds were displayed in a variety of cuts and sizes. Most of the production is between 2 and 4 mm; they try to cut the melee within 0.05 mm tolerance. Mr. Groom expects to unveil 10,000–15,000 carats at the 2016 JCK show in Las Vegas. Eternity Emerald is also purchasing rough from Zambia and Brazil to ensure a continuous supply of melee.

We also saw a 12.52 ct cushion-cut emerald (figure 9) that came from a 60 ct Afghan rough. The stone was difficult to cut because the rough was highly fractured and color zoned. Also from the 15,000-carat parcel purchased this year were four stones that did not require enhancement, the largest of which weighed 4.61 ct. Mr. Groom estimated that, given the same size and quality, the value difference between treated and untreated emerald ranges from 20% to 100%.

Also on display was a 17.14 ct ruby that had the intense red color of marble-hosted material and a slightly sleepy transparency. The untreated ruby was cut from a 45.37 ct rough, part of a parcel of more than 1,000 carats, purchased directly from Tajik miners in May 2015. While this rough is available within Tajikistan, Mr. Groom said the material is not easily found on the global market. The asking prices for the rough were high and firm. The parcel was much more difficult to evaluate than ruby from Myanmar or Mozambique, as the rough was highly fractured. This is not uncommon for Tajik ruby, and it makes determining the yield and quality of the finished stones problematic. Due to the fracturing of the rough, heat treatment may not be a viable option for color improvement. The parcel

Figure 9. This 12.52 ct cushion-cut Afghan emerald came from a highly fractured and color-zoned 60 ct rough. Photo by Robert Weldon/GIA; courtesy of Eternity Natural Emerald.

Figure 10. The decision to recut a 21.17 ct ruby into this 17.14 ct gem added substantial value. Photo by Robert Weldon/GIA; courtesy of Eternity Natural Emerald.
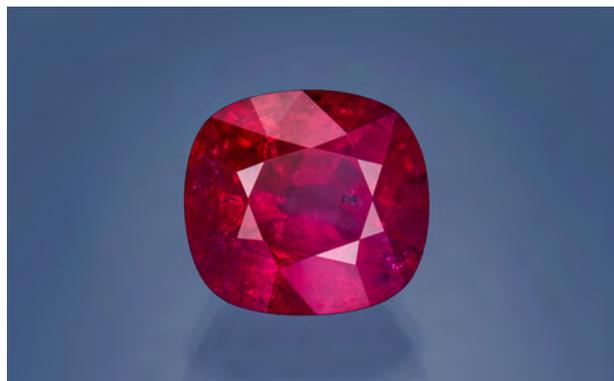
Figure 11. The surface-breaking fissure in this faceted Paraíba tourmaline (left) is less visible after cleaning and filling (right). Photos courtesy of Eternity Natural Emerald.

Figure 12. Prior to treatment, the highly visible fissure detracted from the rubellite's clarity (left). After treatment, the fissures were less visible, and the stone had a more uniform clarity (right). Photos courtesy of Eternity Natural Emerald.

yielded a total of nine faceted stones, none of which were heat treated. The largest, a 21.17 ct stone, was cut from the original 45.37 ct rough. A large black inclusion was still visible after cutting. After being shown to several potential buyers, the ruby was recut to 17.14 ct. The inclusion was less visible in the resulting gem (figure 10), and the color and brightness were also improved. Mr. Groom said recutting increased the ruby's overall value more than 30%.

At the booth, we also saw photos of their clarity-enhanced tourmalines. Clarity Enhancement Laboratories (CEL) performs the filling of the surface-reaching fractures. Mr. Groom pointed out that fracture filling of tourmaline is nothing new. Most of the material he has seen in the market has been filled with oils and resins, often without disclosure, since the trade has not traditionally thought of fracture filling as a way to improve tourmaline's apparent clarity. In August 2015, CEL announced tourmaline clarity enhancement service. The process, which is similar to its ExCel method for filling emerald fractures, is offered in their New York City laboratory for all colors and varieties of finished tourmaline. This treatment is not available for rough material.

Although they will fill any variety and color of tourmaline, CEL has mostly received Paraíba (figure 11), rubellite (figure 12), and bicolor material. Mr. Groom attributes this to the intrinsically higher values for these varieties. These color varieties often have surface-reaching fractures, and the filling process makes the material much more marketable. Since there is a high demand for these types of tourmaline, treated goods are still of value to dealers. Mr. Groom hopes to promote CEL's clarity enhancement method as a positive thing that will be fully disclosed through the value chain.

Tao Hsu and Andrew Lucas

Rare emerald from China and pink sapphire from Sri Lanka. At the AGTA show, David Nassi of 100% Natural

Ltd. (New York) showed the authors a 5.06 ct bright yellowish green emerald from China's southwestern Yunnan province. The stone had some eye-visible inclusions, mainly fissures (figure 13). Other than a few tiny chips along the girdle, the cut gave the emerald a very elegant appearance. Mr. Nassi purchased the stone from a reliable Thai gem dealer who bought it from a Pakistani merchant who obtained it along the China-Pakistan border. Since Mr. Nassi is a cutter who deals with many antique jewelry pieces mounted with stones, he usually recuts stones before selling them. He kept this emerald "as is" due to the superb quality and size for this specific source. The stone was certified by the American Gemological Laboratory as without oil treatment, with China as the country of origin.

China's only economically viable emerald deposit is located in Malipo County in Yunnan province. The deposit was first discovered in the early 1990s but has never been

Figure 13. This 5.06 ct emerald from China's Yunnan province is one of the finest from this source. Photo by Robert Weldon/GIA, courtesy of 100% Natural Ltd.

Figure 14. Due to the fissures in Chinese emerald, stones are usually marketed as mineral specimens. This emerald crystal is still in the matrix. Courtesy of Yunnan Emerald Magazine.

extensively prospected or mined. Emerald specimens and crystals are extracted as the byproduct of the tungsten and tin deposit. Geologically, the ore body occurs in a core complex and is related to granitic intrusions in that area. Geochemical studies revealed that the trace element vanadium concentration is about one magnitude higher than that of chromium, indicating that V is the predominant chromophore in Yunnan emerald.

The size and quality of this emerald are rare for Yunnan. Since the stones contain abundant fissures, most of the production is sold as mineral specimens or ornamental pieces (figure 14). A very small percentage can be faceted for jewelry. As the local government pays more attention to this emerald resource, new development and further exploration are expected.

Mr. Nassi also showed us an intensely saturated 24.69 ct Sri Lankan pink sapphire (figure 15), from a necklace he had obtained from another estate jewelry dealer. Although

Figure 15. This 24.59 ct Sri Lankan pink sapphire was removed from an estate necklace and recut to bring out its full potential. Photo by Robert Weldon/GIA, courtesy of 100% Natural Ltd.

the necklace itself was unattractive, Mr. Nassi immediately saw potential in the sapphire. He estimated the weight of the mounted stone and made an offer to buy the necklace. The stone, which was abraded with multiple scratches, lost two carats in its recutting but showed a dramatic improvement.

Tao Hsu and Andrew Lucas

Fordite from the Corvette assembly plant. Gemstone cutter and mineral specimen collector Jason Baskin of Jay's Minerals (Flemington, New Jersey) presented some spectacular freeform fordite cabochons, a byproduct of an automobile painting process that is long gone.

Workers once painted automobile bodies on train cars, which are commonly used on large assembly lines. As the paint was sprayed onto the target, the overspray collected on the train cars, and the accumulated layers of excess paint went together with the painted car body to the oven. The factory removed the accumulation periodically to clean the working platform and possibly recycle the paint. Mr. Baskin was informed by his contact in the factory that it takes about 997 layers of paint to build a one-inch-thick fordite slag specimen (figure 16). Since hand spraying has been replaced by powder painting, fordite is no longer produced, and the material on the market is all that exists. Fordite was first collected at Ford Motor Company in Michigan in the 1940s. The material saved from the 1960s and 1970s has the boldest colors, since cars were painted in very bright colors during that period.

Mr. Baskin was introduced to fordite about three years ago by a friend and fellow gem cutter whose uncle worked at the Corvette assembly plant in Bowling Green, Ken-

Figure 16. Three fordite slag specimens alongside a partially open piece that shows paint layers with various colors and thicknesses. Photo courtesy of Jay's Minerals.

Figure 17. Different patterns may be exposed when the fordite material is cut open. The original profile of the paint slag can be kept as well. Strata and concentric color circles are some of the most spectacular patterns. On the left is a 32.36 ct (52 × 64 mm) specimen; the one on the right is 41.86 ct (28 × 73 mm). Both pieces were polished by Jason Baskin. Photo by Robert Weldon/GIA; courtesy of the Clamshell.

Figure 18. The finished pieces shown here are some of the finest fordites on the market. Photo by Orasa Weldon/GIA; courtesy of Jay's Minerals.

tucky. Mr. Baskin and his friend now own a substantial collection of the material from that location. Mr. Baskin is also pursuing other sources, including Lincoln-Mercury paint from a Canadian plant and Ford paint from Detroit. He is also looking for fordite from Harley-Davidson motorcycles to fulfill the appetite of Harley lovers.

The color layers and patterns of polished fordite are eye-catching, and experienced cutters know how to unveil its most beautiful side (figure 17). Because it is composed of paint, the material is very light. Protection such as a dust mask is necessary during the cutting and polishing processes.

Mr. Baskin noted that jewelry designers and hobbyists purchase most of his fordite, though he also sells the cut material (figure 18) through other gem dealers. Some of the knobs from the heaters and gear shifters in the old Corvettes had a piece of embedded plastic; clients have him cut Corvette fordite to replace that plastic. Pricing ranges from $20 to several hundred dollars apiece. A very rare type of fordite from 1972 with large metal flakes sold for $400 once it was cut into a 40 × 30 mm cabochon.

Tao Hsu and Andrew Lucas

Imperial Flame topaz sculpture. One of the 2016 Tucson show's most noteworthy gems was a 332.24 ct freeform Imperial topaz (figure 19) at the GJX booth of gem cutter Alexander Kreis (Sonja Kreis Unique Jewelry, Niederworresbach, Germany). Topaz with this red, pink, or orangy yellow color component is rare and highly sought after in the trade. Named the "Imperial Flame" by the Kreis family, the crystal was reportedly recovered from Brazil's Ouro

Preto topaz mines two decades ago. Topaz has been known from this area of Minas Gerais since 1768 (P.C. Keller, "The Capão topaz deposit, Ouro Preto, Minas Gerais, Brazil," Spring 1983 *G&G*, pp. 12–20).

Although mining was extensive at Ouro Preto in the mid-1990s (D.A. Sauer et al., "An update on Imperial topaz from the Capão mine, Minas Gerais, Brazil," Winter 1996 *G&G*, pp. 232–241), the Kreis family confirmed that there is currently no large-scale mining. They visited the area after a collector informed them of a 615 ct crystal with exceptional color and clarity (figure 20). According to their contact, the crystal is "old production" mined at least 20 years ago. After analyzing the rough over a period of four months, the family purchased it in December 2015 with

Figure 19. The Imperial Flame, a magnificent natural-color Brazilian topaz, was cut from a 615 ct crystal recovered some 20 years ago. The finished 89.53 × 20.56 × 19.15 mm sculpture weighs 332.24 ct. Photo courtesy of Sonja Kreis Unique Jewelry.

Figure 20. The original 615 ct Imperial topaz crystal from which Alexander Kreis fashioned the 332.24 ct Imperial Flame. Photo courtesy of Sonja Kreis Unique Jewelry.

the objective of cutting the largest, highest-quality Imperial topaz known.

Due to the gem's perfect basal cleavage, cutters must avoid grinding the stone perpendicular to the cleavage plane, while also accounting for inclusions that might cause the stone to break on the wheel. According to Sauer et al. (1996), well-formed, largely inclusion-free crystals typically yield up to 2 ct per gram (5 ct), which is a 40% recovery rate. Cutting the Imperial Flame took approximately eight days, spread over a period of 3–4 weeks, to allow Kreis to make trial carvings with smaller Imperial topaz pieces to test his cutting concepts. The cutting process began with sawing off the included portions and grinding to shape the solid crystal (figure 21), followed by

faceting and carving to produce the reflective, grooved surfaces. The fashioning process yielded a spectacular gem measuring 89.53 × 20.56 × 19.15 mm. At 332.24 ct, it had a finished yield of 54%.

Intended as an arresting gem sculpture for a connoisseur or high-end collector, the piece is for sale.

Duncan Pay
GIA, Carlsbad

Update on the Scorpion tsavorite mine. At the AGTA show, Bruce Bridges (Tsavorite USA Inc.) detailed current activity at the Scorpion mine in Kenya and showed some new production (figure 22). The mine lay dormant for more than five years after the 2009 murder of owner Campbell Bridges, who originally discovered tsavorite. While waiting for the courts to hand down verdicts, the Bridges family and their employees were the target of numerous death threats. In January 2015, after four of the eight defendants received sentences of 40 years without parole, the mine reopened with a larger scale of operations than ever before.

Activities expanded for a variety of reasons. As a corporation rather than a small family operation, the Bridges family felt that they were less of a target for criminals. The Bridges also found that the demand for tsavorite rose exponentially during the mine's closure. With a limited supply and greater popularity, the higher selling price has made larger-scale mining more feasible.

There are 80 to 100 workers at the Scorpion mine, three times the number employed when it closed in 2009. The miners work in continuous shifts seven days a week. Mechanization has increased to include more powerful generators and 15-kilowatt fans for ventilation in the tunnels. The tunnel is now below the oxidized zone, requiring a blast approximately every half meter of forward progress.

Figure 21. After trimming away included portions of the crystal's base, Alexander Kreis gently removes any surface-reaching inclusions and begins to shape the crystal to his own unique design. Photo courtesy of Sonja Kreis Unique Jewelry.

Figure 22. The new production from the Scorpion mine includes these 6.48 ct and 3.43 ct tsavorites. Photo by Robert Weldon/GIA, courtesy of Tsavorite USA Inc.

The stronger fans allow the ventilation system to remove the smoke and dust in about two hours rather than the full day previously needed. They have also invested heavily in trucks, buildings, jackhammers, drills, and more explosives. Campbell Bridges's original campsite and tree house remain intact.

The main focus of the current operation is the Bonanza tunnel, also called tunnel 4, which was Scorpion's most prolific tunnel in the 1980s. They are also working the adjacent tunnel 2, the largest producer in the 1990s. Tunnel 2 produced five kilograms of facet-grade material over one carat from one pocket during this period. A few kilometers from Scorpion is mine GG2, which typically produces tsavorite with lighter tones. GG2 is an open-cast operation on a hill, with plans to move into a tunnel phase later this year. An untouched surface deposit near tunnels 2 and 4 is also in development for open-cast mining, and the Bridges have high hopes for it, as the ratio of yield to waste is high on new deposits. Other sources include GG3, which is several kilometers away and primarily uses tunnel mining, and Snake Hill, which is one kilometer from Scorpion and has been mined by both open-cast and tunnel methods. Snake Hill is also a tanzanite source. These deposits have been put on hold in favor of tunnels 2 and 4 and GG2, as well as the untouched surface deposit.

There is now greater sophistication and manpower in Tsavorite USA's mining process. The drill team bores large holes in the tunnels and then places the explosives. After the blast, the air is flushed out by the new ventilation system. The removal of waste has been accelerated by the use of a mono winch, which allows up to eight tons of waste to be removed hourly. The waste is hauled to the dump site, where it is separated from the rock face. The mine manager examines the rock face for tsavorite crystals or nodules, also checking for indicators in the reef such as calcite, quartz, and pyrite. Depending on the indications, teams will either continue blasting or extract material with hammer and chisel until the gem body is reached. At that point, miners use sharpened six-inch nails and finally their hands. The gem-bearing specimens are bagged and marked for quality. Once out of the mine, the material is washed and the tsavorite crystals are separated from the host rock. Sieves are used to sort the production by size before it is graded on a sorting table (figure 23). It is then bagged, sealed, and taken to Nairobi by ground or air, depending on its value.

All rough that can be cut to yield a 50-point stone or higher will be cut in-house in Kenya, while the cutting of smaller rough is outsourced. Campbell Bridges learned to cut gemstones in Idar-Oberstein, Germany, and he later trained local Kenyans. One expert cutter on-site is cutting at least 200 stones a month. The Bridges family is proud of their high cutting standards and that they cut most of the high-quality rough in Kenya (figure 24). They also pay a higher export value for finished cut stones than rough, generating more revenue for Kenya. The stones are exported to Tsavorite USA's main sales office in Tucson or to customers worldwide.

Figure 23. Prior to cutting, the Bridges operation sorts the tsavorite rough into categories by size, color, clarity, and shape. Photo courtesy of Tsavorite USA Inc.

Even with the new investment and expenses, current production is only about 10% higher than before the mine was closed. Electromagnetic surveys have shown extensive anomalies that indicate tsavorite enrichment zones. Most experts believe the reserves are very good, and Campbell Bridges himself believed he could follow the lines of the Scorpion mine's saddle reef structure and the nose of the folds for two kilometers while producing tsavorite in pockets. Each tunnel at Scorpion is about 200 meters deep. These reserves must be balanced, however, with the growing cost of delving every meter further into the earth.

Bruce Bridges told us that "demand is through the roof" for tsavorite. With its popularity potentially on the rise, Tsavorite USA will have to outsource rough. Melee demand is at an all-time high, particularly in China and other Asian countries, where it far exceeds the available supply. Mr. Bridges foresees overall growth for tsavorite through

Figure 24. The Bridges intend to keep their tsavorite cutting in Kenya for as long as it is economically viable. Photo courtesy of Tsavorite USA Inc.

television sales, but he wants to keep as much cutting in Kenya as possible. Challenges for the company include possible changes in the political scene, mining regulations, and the threat of crime and violence. Upon returning to Kenya, Mr. Bridges reported to the authors that death threats had started again.

Tao Hsu and Andrew Lucas

Jewelry Television in Tucson. Jay Boyle, senior gemstone buyer at Jewelry Television (Knoxville, Tennessee), spoke with us about the importance of the Tucson shows to JTV as well as the impact of television on the trade at large. We saw him conduct live broadcasts from the gem fair and interview dealers at their booths (figure 25). Mr. Boyle said the key to buying for television is finding beautiful gems at low market prices and being able to tell the story and romance the stone while educating the customer.

He pointed out that finding beautiful stones is easy, but it is considerably more difficult to obtain them at a great value price point that is right for the television network's customers; in fact, there is an art to the process. Major dealers from all over the world come to Tucson and sell all varieties of gemstones, making it advantageous for JTV to attend. These dealers frequently sell stones among themselves at true wholesale prices, so Mr. Boyle has the opportunity to find attractive stones at the right price and value

Figure 26. During times when prices are firm, buying decisions and quality control are even more crucial. Jay Boyle and Natalie Tjaden of Jewelry Television keep this in mind as they examine gemstones in a dealer's booth. Photo courtesy of Jewelry Television.

Figure 25. Broadcasting from the gem shows helps Jewelry Television educate viewers about colored gemstones. Photo courtesy of Jewelry Television.

for television (figure 26). In Tucson, buyers can survey everything coming from the sources, including new production, and discover the true market prices, all within one week. He added, "If you have a reputation as a serious, knowledgeable buyer that buys in quantity and has cash to buy, you can find the real market price."

According to Mr. Boyle, the best time to purchase is when the material first hits the market. Another good time to buy is when there is a sudden increase in production. In 2001, JTV bought a large tsavorite lot containing more than 2,200 carats of material ranging from 2 to 10 ct per stone. The color and clarity were fine, and the price was a good value at $350 per carat. They took a small margin and sold the production quickly; 5 to 7 ct gem-quality tsavorites went for $500 per carat. Today, the wholesale prices for the material are many times that price, and longtime customers see the value of purchasing at the right time. Another successful venture began in 2006, when Mr. Boyle started buying "best of show" material of all gem species, at the best price possible. These stones were sold during special broadcasts called "The Vault" (figure 27). The highest price recorded on the show was a $400,000 sapphire. Regular viewers know that at times JTV has sold remaining inventory below cost, and some actually make a business out of reselling this merchandise.

Founded in 1993, Jewelry Television broadcasts 24 hours a day, reaching 84 million homes. Ninety-five percent of the gemstones sell for $10 to $5,000 apiece. Viewers are introduced to gemstones they had never encountered,

such as padparadscha sapphire, Paraíba tourmaline, and color-change garnet, while learning about the gem business and how to recognize bargains. Some steady customers tune in for 10 hours a day. When Jewelry Television first started offering loose colored stones, they were thrilled to sell $15,000 in an eight-hour period. Now they sell up to $400,000 of loose colored stones in an hour, and it is common to ship between 18,000 and 25,000 packages in one day. Mr. Boyle feels that JTV is driving business throughout the retail industry by promoting colored stones, as some viewers will learn about a given gemstone and then visit a local jeweler to make a purchase.

Between 30% and 35% of the company's $400–$500 million in annual sales are online at jtv.com, which complements rather than replaces television sales. The website is also used to clear inventory from television at liquidation prices. Due to the extremely high cost of airtime in the U.S., JTV must not only sell the entire inventory, but also sell it in a short time. That means the Internet can be used to move leftover inventory while fresh, faster-moving products are sold on television. The network plans to eventually host web-only streaming video broadcasts.

Interestingly, one of the most successful periods for Jewelry Television was during the global economic crisis. While many industry players had stopped buying by January 2009, Mr. Boyle had learned over the years that dealers sell below cost during a recession. At the 2009 Tucson show, he bought $7 million in gemstones, including $3 million in tanzanite from one dealer alone. Since Mr. Boyle had well-established buying relationships with dealers, they were willing to accept his plan to promote a buying opportunity for TV customers. The promotion of below-

Figure 28. The "Rainbow Over Montana" bracelet contains 76.83 carats of Montana sapphire (71.42 carats rough and 5.41 carats faceted). The ring from the same collection contains 11.57 carats of rough and 1.12 carats of faceted Montana sapphires. Photo by Robert Weldon/GIA; courtesy of Paula Crevoshay.

Figure 27. The pendant worn by host Dawn Tesh (left) contains a 102 ct aquamarine that was sold during a 2009 broadcast of "The Vault" on Jewelry Television. Photo courtesy of Jewelry Television.

market prices created a frenzy of activity for Jewelry Television. While these bargains were more plentiful in 2009, Mr. Boyle said there are still great opportunities below market value every year in Tucson. Although he was buying less than usual this year, JTV still actively sought material throughout the show. Among the stones we saw Mr. Boyle buying were rhodochrosite and Ethiopian opal.

Tao Hsu and Andrew Lucas

Paula Crevoshay's American Collection, plus jewelry with nontraditional gemstones. Paula Crevoshay's American Collection, created as a cultural and artistic inheritance for future generations, featured gemstones from the United States. The first pieces we saw were from her "Rainbow Over Montana" collection of rough and faceted Montana sapphires (figure 28). She used the faceted sapphires to show "the story of light" told by the gemstone after the human contribution of cutting, while the crystal slices display the natural hexagonal shape and luster of the flat crystal faces. The blue faceted stones represent the "Big Sky Country" of Montana, and the crystals demonstrate the range of rainbow colors in Montana sapphire.

Figure 29. This 31.34 ct bicolor tourmaline pin, which contains gemstones exclusively from the Stewart Lithia mine in San Diego County, has an emotional connection for the artist. Photo by Robert Weldon/GIA; courtesy of Paula Crevoshay.

Figure 30. While not as large as some of the other colored stones used by Paula Crevoshay, the intense color and unique cut of the 2.77 ct Oregon sunstone makes this ring one of her favorite pieces. The center stone's color is complemented by 3.24 carats of red spinel. Photo by Robert Weldon/GIA; courtesy of Paula Crevoshay.

The next piece was a pin featuring a 31.34 ct bicolor pink and green tourmaline (figure 29) from the Stewart Lithia mine in San Diego County, California. The stone was purchased back from a customer who had bought it from Paula's late husband, George Edward Crevoshay, who first cut the stone more than 30 years ago. The pink and green tourmaline melee in the piece was also cut by Mr. Crevoshay and came from the Stewart Lithia mine. Besides featuring gemstones from a famous U.S. mine, this piece carries the sentiment of a great love that inspired Paula Crevoshay to move from painting and sculpture into the world of gemstones and creating jewelry.

The third piece (figure 30) was a ring that contained one of the most intense red Oregon sunstones the authors had ever seen. The stone features the trademarked "Medicine Wheel" cut by award-winning lapidary Larry Woods. The ring also contains red spinels and diamonds.

While visiting her booth at the AGTA show, the authors also noticed some nontraditional stones ingeniously incorporated into jewelry. The first two pieces we viewed contained center stones of sphalerite (figure 31, left) and sphene (figure 31, center), both in pendants. For Ms. Crevoshay, creating jewelry is all about working with light. How she selects and combines gems depends on properties such as refractive index, bodycolor, luster, and phenomenal optical effects.

Figure 31. These Paula Crevoshay jewels include gems not typically used in jewelry. Left: The 8.25 sphalerite pendant creates an eye-catching fire, complemented by the play-of-color of the opal and the colorful sparkle of the diamond melee. Center: The green color of the 11.78 ct sphene pendant is accentuated by tsavorite melee, with the orange fire opals offering a striking contrast. Right: This dragonfly pin features a 38.24 ct hematite drusy as the insect's body. The drusy's iridescence and sparkle creates a shimmering effect that is intensified by the orient of the Tahitian cultured pearl used for the head. Photos by Robert Weldon/GIA; courtesy of Paula Crevoshay.

Both sphalerite and sphene are highly dispersive, and the flashes of rainbow color created by the dispersion excite the eye. For the sphalerite piece, she added Mexican opals showing a rainbow of colors, combining a highly dispersive gem with phenomenal accent stones to create a dance of colors across the pendant. The pendant also contains cognac and colorless diamonds to create even more of a symphony of colors. Ms. Crevoshay chose the sphene for its high dispersion and her attraction to the green bodycolor. As with the sphalerite pendant, she added Mexican opals showing a subtle rainbow of phenomenal colors. With both pieces, she combines gemological knowledge with art to create jewelry that paints with the surrounding light.

Another piece that caught our attention was a dragonfly containing rainbow hematite drusy as the insect's body (figure 31, right). With the hematite, Ms. Crevoshay was able to highlight the iridescent colors and sparkle of the drusy. She finds that the rainbow colors of the hematite are not as bold as those caused by dispersion from the sphene and sphalerite but still have a seductive effect.

Public awareness of gemstones such as sphene and sphalerite has been growing thanks to high-end designers such as Paula Crevoshay and through mass marketing of commercial jewelry on television. Ms. Crevoshay told us she often piques customers' interest by informing them about some of these lesser-known gem materials and how light interacts with them. The authors found this to be a fascinating look at how stones that were once a gemological novelty are becoming more widely known.

Tao Hsu and Andrew Lucas

Wheel of Light's mesmerizing optics. Lapidary artist Brian Cook, of Tucson-based Nature's Geometry, is astonished that the optical designs he has experimented with and refined for more than 25 years have finally come of age. Appreciation for his work culminated with a first-place award in this year's AGTA Spectrum's Fashion Forward category for his "Wheel of Light" Numinous pendant (figure 32), which graces the cover of this issue.

The 825 ct quartz center stone of this piece was carved to resemble a rounded disk with a softly contoured apex, or dome. After drilling the apex, Mr. Cook carefully inserted rough crystals of Paraíba tourmaline, haüyne, ruby, and spessartine garnet. The channel was then filled with jojoba wax and hermetically sealed with a quartz plug. The trapped "inclusions" are visible if the disk is observed from the side. As the disk is turned, with the viewer gazing down the apex, an interesting optical effect is noted: The colors corresponding to the included gem rough are revealed as concentric rings. To the eye, the ringed colors appear as painterly brushstrokes. Mr. Cook explained that the quartz vessel becomes both a frame and a mirror for what the eye sees. "The colors are amplified by the quartz, reflected off its inside surface. The jojoba wax, with a refractive index close to that of quartz, causes the channel to

Figure 32. The "Wheel of Light" Numinous pendant contains an 825 ct carved quartz centerpiece. Different rough gems have been placed into a channel drilled into the quartz by the lapidary artist, which was then set in 24K gold. Photo by Robert Weldon/GIA; courtesy of Nature's Geometry.

virtually disappear. This is how the luminosity and color of the included crystals is accentuated."

Goldsmith Paula Brent, a longtime collaborator, brings the pieces to completion. The wheels are crafted using 24K gold, which accentuates the strength and purity of the finished object.

Mr. Cook says that the work of Nature's Geometry is futuristic and imaginative, but at the root of it is a mystical, ancient attraction to the mineral world. The company is connecting with innovative young designers and is appreciative that the "millennial" generation is affected by the beauty and power of gems and hungry for a nontraditional approach to jewelry. Mr. Cook has been involved with the exploration for and marketing of copper-bearing tourmaline from Paraíba, Brazil, since 1988, shortly after its discovery. "The rough I saw were often too small for cutting, and the material was always extremely rare. But the color was so vibrant that I kept looking for a way to bring that 'electrifying' color to a greater audience."

With the Wheel of Light numinous pendant, Brian Cook has done just that.

Robert Weldon
GIA, Carlsbad

GILC 2016. The International Colored Gemstone Association (ICA) held its annual Gemstone Industry & Laboratory Conference on February 1 during the Tucson shows. Invited participants included jewelry trade association leaders, laboratory representatives, academic institutions, and ICA members. This year, other industry members were welcomed into the afternoon open discussion session.

Lore Kiefert (Gübelin Gem Lab, Lucerne, Switzerland), presenting on behalf of her colleague **Daniel Nyfeler**, spoke on age determination by radiogenic isotopes. Laser ablation–inductively coupled plasma–mass spectrometry (LA-ICP-MS) has enabled the Gübelin Lab to use radiometric dating to test inclusions at or near the surface of materials such as corundum and emerald, which do not have radioactive atoms. When traditional methods such as observation of inclusions and growth structure and trace element analysis lead to more than one possible country of origin, radiometric dating can furnish the decisive data. U/Pb decay in zircon has been well documented as a means to establish an approximate timeline for known sapphire and emerald populations. The corundum timeline established the oldest population as African, with an age of 450–650 million years (Ma), and the youngest as Colombian, at 10 Ma. Emerald formation ranged from South Africa at 2900 Ma to Colombia at 65–35 Ma. This method is limited when the gemstone presents no analyzable inclusions or has been treated.

James Shigley (GIA, Carlsbad) presented the Institute's latest research findings. GIA's work with color analysis has its foundation in observation and color grading of colored diamonds. Dr. Shigley noted that the visible spectrum is not the only cause of color; in fact, the face-up appearance is influenced by about 15 factors, including the emission spectrum of the light source, the absorption spectrum of the stone, and the color sensitivity of the eye. Since humans are more adept at distinguishing differences than similarities, the use of master stones and bracketing between pairs is well suited for visual grading. GIA uses instrumentation to supplement visual grading in face-down evaluation of round near-colorless D to Z diamonds; however, fancy-color diamonds are graded face up. GIA has been working on analytical tools that can "detect" color in the same way that the human eye processes it.

Bruce Bridges (Tsavorite USA, Inc.) asked whether gems can be reliably traced from the source to the consumer. Today's consumer wants to know where products come from and how their manufacture affects both the environment and workers. Vertically integrated companies can promote traceability and control over ethical sourcing, but the business model cannot be applied to the small-scale operations that characterize most of the industry. Bridges outlined the convoluted path from small-scale or individual miner through a series of brokers to cutting and the "end user" market, where it may go through another series of dealers before reaching a consumer. Most colored stone sources are overwhelmingly alluvial or placer deposits in remote areas, making them difficult to centralize. Traceability is even challenging at the mine, where it is not uncommon for material from a different location to be sold without disclosure. Traceability from cutting centers can improve as host countries introduce limits on rough exports and begin developing cutting facilities, which has happened in parts of Africa, South America, and Asia.

The conference proceeded to an open session for invited participants to discuss topics of concern, including:

1. The increasing use of color enhancement and "anti-scratch" (silicon carbide) coatings, which are virtually invisible and sometimes too thin to be detected with instruments. With advances in nanotechnology, more research is needed to develop detection strategies.

2. The inconsistent use of descriptive terminology in laboratory reports, a topic carried over from the 2015 conference. The laboratories maintained that they were responding to the demands of the trade. One participant pointed out that the terms "pigeon's blood" and "royal blue" had no meaning in Chinese culture until about ten years ago. Since then, they have become "deeply implanted," and a seemingly irreversible demand has been created for the level of distinction that these terms confer.

3. Unethical or fraudulent use of lab reports. An example cited is the treatment of a gemstone after it had received a "clean" report. Another is the manufacture of both treated and synthetic diamonds to match an existing natural diamond report. GILC participants stressed the importance of checking reports against stones through every phase of the grading process.

4. The use of "undetermined" on a lab report in regard to treatment or synthetic origin. Some participants voiced concerns that such determinations are beyond the technologies of labs, or that the word "undetermined" left untreated natural diamonds vulnerable to being matched with treated or synthetic stones.

At the conclusion of the conference, it was announced that AGTA had revised its code of ethics and principles of fair business practice. ICA is proposing to adopt AGTA's code of ethics, due diligence protocol, and source disclosure language as a basis for its own code.

Donna Beaton
GIA, New York
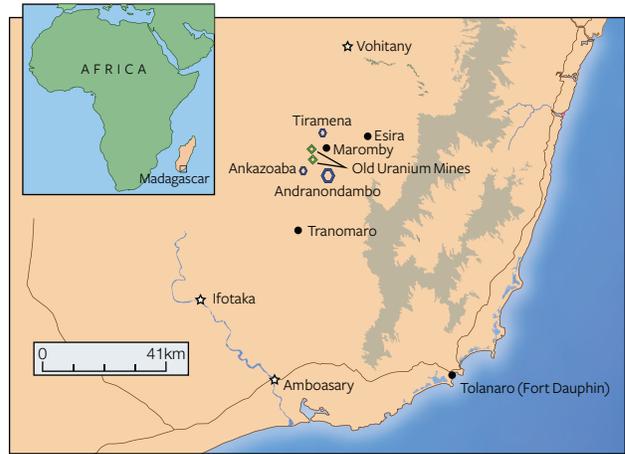
REGULAR FEATURES

COLORED STONES AND ORGANIC MATERIALS

Blue sapphires from a new deposit near Andranondambo, Madagascar. In January 2016, author VP was informed by Nirina Rakotosaona (Societe Miniere du Cap, Madagascar) and Jack Mampihao of a sapphire rush in the south of the island near Andranondambo. The blue sapphires (figure 33) are reportedly from a primary deposit and similar to those produced near Andranondambo, the region that put Madagascar on the map as a world-class sapphire source two decades ago (D. Schwarz et al., "Sapphires from the Andranondambo region, Madagascar," Summer 1996 *G&G*, pp. 80–99). Details emerged as miners returned from the rush in February. According to these firsthand accounts, the new mines are located near Vohitany, north of Tiramena (figure 34). They are only accessible by foot, and it takes about a day of walking from Tiramena to reach the area.

The author's contacts in Madagascar did not consider it safe to travel to that area, which is known to be a haven for bandits, called *malaches* or *dahalo*. In early February, the author learned from Karim Guerchouche (Premacut, Bangkok) that a 1 kg parcel of the new material had arrived in Thailand. The owner, Isaac Stern, wanted to perform some heat treatment experiments with Premacut. This offered us a chance to conduct a preliminary study of the material before visiting and collecting samples at the site.

Most of Mr. Stern's parcel consisted of rough weighing between 1 and 4 ct. The largest stone was an etched crystal weighing nearly 15 ct (again, see figure 33). The parcel was composed of attractive, well-formed crystals still associ-

Figure 34. According to miners, the new deposit is located near Vohitany, north of Tiramena. This remote area is only accessible by foot.

ated with kaolin. Out of more than 300 stones studied, only one showed some indication of weathering. This suggests that the material is from a primary deposit. The stones were euhedral transparent crystals with strong blue color zoning. Overall, the material was very similar to the specimens the author collected in Andranondambo and Tiramena during visits in 2005, 2008, and 2010.

Sixty-three stones from the original parcel (mainly clean and milky specimens) were selected for a heat treatment experiment. Fifteen other stones, most of which hosted inclusions, were studied at GIA's Bangkok lab (figure 35). The study confirmed their similarity to GIA reference samples from Andranondambo; details will be published in a *News from Research* entry on the GIA website.

The new stones showed a medium to high iron content (between 300 and 1100 ppma), consistent with the classic Andranondambo material. Strong blue color zoning and an abundance of negative crystals dominated the inclusion

Figure 33. These three rough unheated sapphire crystals, weighing (from left) 9.98, 14.56 and 7.7 ct, are reportedly from Madagascar's newest rush area. Beside them are heat-treated faceted sapphires believed to be from the old deposits around Andranondambo. The pear-shaped faceted stone weighs about 4.17 ct. Photo by Vincent Pardieu/GIA.

Figure 35. A detailed view of the 15 unheated samples selected for a preliminary study. The stones were placed on a light box and are seen here using bright diffused light. Under such conditions, the strong color zoning is obvious. Photo by Sasithorn Engniwat/GIA.

Figure 36. A blue sapphire from Madagascar's newest deposit hosts this group of negative crystals. Some crystals host white hairlike diaspore needles, identified using Raman spectroscopy. Photo by Victoria Raynaud/GIA; field of view 1.2 mm.

scene (figure 36). Many stones contained bands of minute particles, thin needles, and growth tubes. Calcite mineral inclusions were common; we also identified mica and apatite crystals.

The heat treatment experiment was successful. The light-colored, slightly milky material turned into fine transparent, deep blue stones after heat treatment under reducing conditions for seven hours at approximately 1600°C. Most of the included stones broke during the experiment, probably due to the presence of negative crystals.

This exciting discovery suggests that the Andranondambo sapphire deposit is much larger than originally expected. The main challenges are the security issues and the nature of the deposit itself, as the rocks hosting the sapphires are very difficult to work.

Vincent Pardieu, Supharart Sangsawong,
Wim Vertriest, Stanislas Detroyat,
Victoria Raynaud, and Sasithorn Engniwat
GIA, Bangkok

Red cordierite from Madagascar. At the Mineral Expo show in Paris in early December 2015, we procured a large piece of dark red cobbed rough presented as cordierite. This would be the first documented occurrence of red cordierite. The slightly fractured 3 cm rough offered a magnificent deep red color when examined using transmitted light from a Maglite illuminator. The identity of the rough as cordierite was confirmed using Fourier-transform Raman (FTR) spectrometry. The spectrum obtained showed excellent agreement with a reference spectrum for cordierite from Madagascar in the RRUFF database (http://rruff.info).

Author TP confirmed that the piece we examined was from the Iakora district, Fianarantsoa province, in southeast Madagascar. Cordierite has long been known in this general area (A. Lacroix, *Minéralogie de Madagascar*, A. Challamel, Paris, 1922). There is no mechanized mining. According to a miner's sketch obtained locally by one of the authors, red

cordierite occurs in a "vein" (probably a layer) associated with orange and blue cordierite, parallel to other layers containing kornerupine or blue spinel. The cordierite vein is about 1.50 m thick and wide and is apparently contained in a kornerupine layer. Cordierite is usually found in a metamorphic environment, but the layered appearance, with each band containing specific minerals in thicknesses of about 1 m, is reminiscent of metasomatic deposits. The association of cordierite with kornerupine and spinel is already known; blue gem-quality cordierite is found in such a metasomatic reaction zone in Kenya (C. Simonet, pers. comm., 2015).

To determine the material's gemological properties, three stones were fashioned by Jacques Le Quéré (Auray, France): a 2.69 ct modified rectangle; a 1.28 ct flat cabochon, cut to obtain a lighter color; and a 4.17 ct parallelepiped, faceted based on the optical directions to best show its trichroism (figure 37). The RIs, measured with a Rayner LED sodium-equivalent lamp, ranged from 1.527 to 1.541 (n_x = 1.528–1.530, n_y = 1.532–1.533, and n_z = 1.538–1.540). Interestingly, this crystal presented a biaxial positive character, whereas gem cordierite is typically biaxial negative.

The trichroism was very strong, as expected with cordierite. With a standard dichroscope, the colors ranged from deep red to orange to grayish brown with a hint of blue or purple (figure 38), this last color becoming black at a thickness of about 1 cm (figure 39). Hydrostatic SG measured 2.548–2.554. These properties are consistent with cordierite, though SG was at the lower end of the range.

As the rough was sawed, we noticed that the vivid red transparent color of the thick crystal turned to orange with reduced thickness. This is the definition of dichromatism, also known in gemology as the Usambara effect, a variation of hue that is affected by the optical path length.

The UV-visible absorption spectrum was measured on

Figure 37. These three gems, weighing (from left) 4.17, 1.28, and 1.28 ct, were fashioned from the same piece of cordierite rough; red is a new color for this gem. The specimen originated from a recently explored deposit in southeast Madagascar. Photo by Benjamin Rondeau.
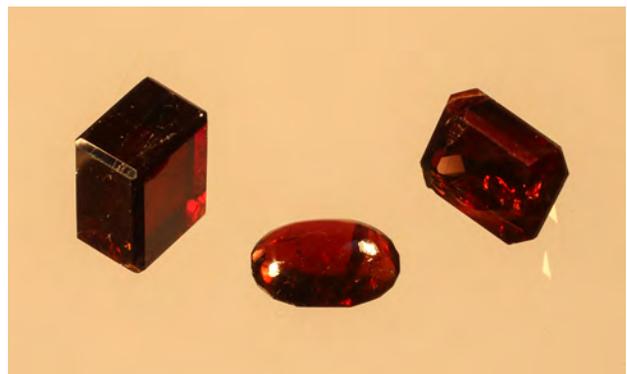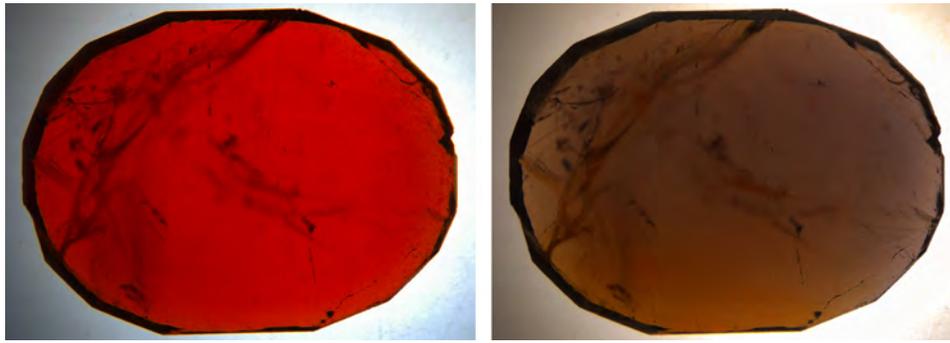
Figure 38. Pleochroism of the oval cabochon observed in polarized light in the two orthogonal directions. On this thinner sample (about 3 mm thick), the desaturated grayish brown color with a hint of blue or purple is best observed. The stone measures 9.85 × 6.75 mm. Photos by Emmanuel Fritsch.

a Unicam UV4. When the material was a few millimeters to a centimeter thick, in the direction where red is observed there is an extremely strong absorption in the violet and blue areas; this band leads to the red color. The absorption decreases abruptly from about 550 to 685 nm, with only a weak broad band from about 710 to 800 nm. This leaves a steep transmission window in the red, which is consistent with the color observed. The shape of the absorption and a rapid decrease in the orange-yellow also explains the Usambara effect. Through a few millimeters, the perceived color is orange; through a centimeter or more, it is deep red.

Emmanuel Fritsch
Benjamin Rondeau, University of Nantes, France
Thierry Peclet, Manakara, Madagascar
Patrick Lefebvre, Aix en Provence, France
*Yves Lulzac, Nantes, France*

Ruby and sapphire from Muling, China. Only a few Chinese sources produce gem-quality corundum, such as Changle, in Shandong province, but sapphires from that location are not considered top quality in the trade because of their dark hues. An emerging deposit in Muling, in northeast Heilongjiang province (figure 40), produces gem-quality corundum comparable to some world-renowned sources. The main deposits are seated in mountain valleys about 70 km from the town center. Corundum was known in Muling as early as 1985; after preliminary exploration, further activity

virtually stopped because of technical and logistical limitations. As a result, production has been very limited, and very little information was published about rubies and sapphires from Muling until 1995 (J.X. Sun, "Basalt related to ruby and sapphire in eastern Heilongjiang and reconstruction of paleovolcanic mechanism," *Acta Petrologica et Mineralogica*, Vol. 14, No. 2, 1995, pp. 126–132).

According to Aijun Yi, director of mineral resource administration in Muling, the region has produced large amounts of gem-quality eluvial materials since 1994, including corundum, brownish red zircon, garnet, and spinel (T. Chen et al., "Brownish red zircon from Muling, China," Spring 2011 *G&G*, pp. 36–41). As colored stones became more popular in the Chinese gem markets, interest in ruby and sapphire from Muling grew accordingly.

We acquired a parcel of rubies and sapphires from local miners. The stones ranged from 0.8 to 15.2 ct (figure 41). Most exhibited well-formed tabular hexagonal crystals, though some broken sapphires had a tumbled appearance. The sapphires were pink, yellow, violetish blue, greenish blue, light blue, and deep blue; there were also near-colorless specimens. Most of the rubies and pink sapphires had a purplish component. Samples other than the deep blue material showed high transparency. Rubies and pink sapphires exhibited medium red fluorescence under long-wave (356 nm) UV light and a weak reaction under short-wave (245 nm) UV. Other varieties of sapphire had no reaction under long- or short-wave UV.

Figure 39. Trichroism of the 9.45 × 6.95 × 5.28 mm cordierite parallelepiped observed in polarized light in the three orthogonal directions to represent the three "extreme" colors of the material's pleochroism: deep red, black (both seen with a thickness of 9.45 mm), and orange (seen with a thickness of 6.95 mm). Photos by Emmanuel Fritsch.
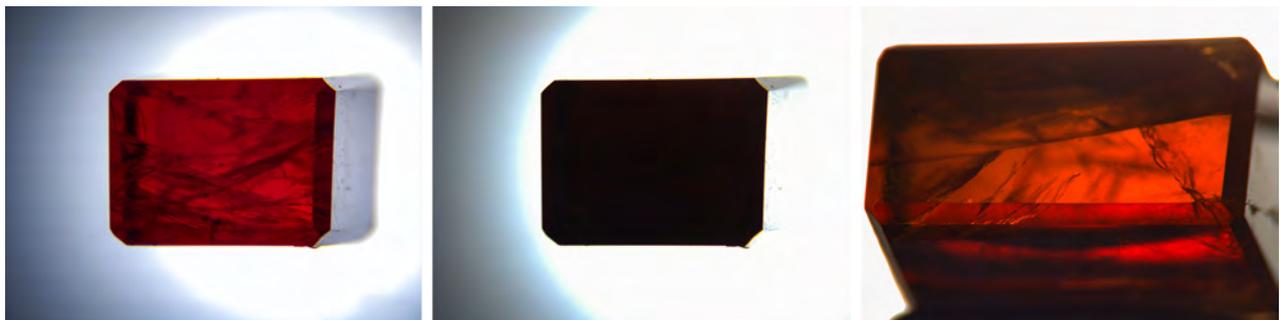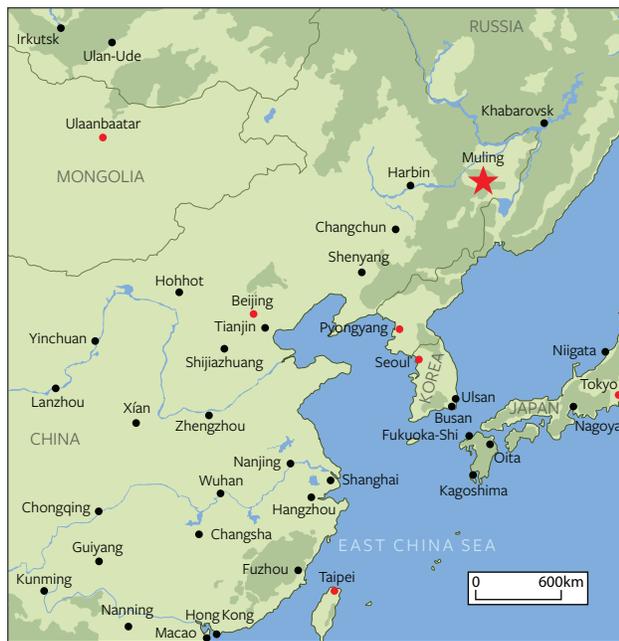
Figure 40. Muling, the site of an emerging corundum deposit, is located in northeastern China.

The samples generally showed abraded features and unhealed fissures, but some were predominantly clean under the loupe and large enough to be faceted. Fourteen stones were fabricated as parallel polished windows for microscopic examination. Several interesting internal features were visible under the microscope. The inclusions, which mainly appeared as rounded single crystals or multiphase syngenetic clusters, were in micron sizes (50–200 µm) and were identified by Raman as feldspar and sillimanite. The

Figure 41. Ruby and sapphire rough from Muling exhibited well-formed tabular hexagonal crystal forms; some sapphires showed a tumbled appearance in broken pieces. Photo by Yimiao Liu.

Figure 42. A detailed structure of whitish needles forming a three-dimensional skeleton network in a ruby sample. Photo by Yimiao Liu.

latter mineral only occurred as component mineral crystals in a multiphase inclusion. Most rubies hosted whitish needles forming three-dimensional skeleton networks that might be the result of diaspore exsolution (figure 42). Further microscopic observations under polarized light showed characteristic lamellar twining structures in every sample.

Trace element analysis by LA-ICP-MS showed a Cr content of 173–636 ppma in the pink-red series, accompanied by a significant level of Fe (1650–2510 ppma) and a noticeable level of Ti (36–70 ppma) to add a blue component through Fe-Ti intervalence charge transfer. This explained why Muling rubies and pink sapphires always had a purplish hue. Mg content was about 46–79 ppma, while Ga (13–17 ppma) fell into the expected range for natural corundum.

Yellow sapphires showed the highest Fe content (4480–4800 ppma); this contributed to their saturated yellow coloration. Iron content was much lower in blue sapphires, along with an appreciable amount of titanium (80–500 ppma) as a blue chromophore. Based on color distribution and transparency, blue sapphires could be grouped as either light blue or deep blue. Most of the light blue sapphires had very high transparency and even color distribution, while deep blue sapphires were less transparent, with hexagonal dark blue color zoning. Among all blue samples, Mg content ranged from 10 to 80 ppma and did not show clear correlation to color, while Ga content (10 to 100 ppma) was noticeably higher than in rubies and pink sapphires.

At Muling, most rubies and sapphires are found by casual surface digging. Gem-quality corundum usually occurs in eluvial deposits derived from weathered Cenozoic alkali basalts. Unlike other igneous-related deposits known for dark blue sapphires and very limited red material, such as Australia's Anakie and New England fields (T. Coldham, "Sapphires from Australia," Fall 1985 *G&G*, pp. 130–146) and Shandong, China (C. Simonet. et al., "A classification of gem corundum deposits aimed towards gem exploration," *Ore Geology Reviews*, Vol. 34, 2008, pp. 127–133), in Muling

ruby production was larger than that of sapphire; over 60% of pink sapphires and rubies were high-quality materials.

In some ways, some Muling rubies have competitive advantages over Mozambique specimens. Their high color saturations and particular internal features (whitish needles forming three-dimensional skeleton networks) resembled those of rubies from Mozambique and might cause confusion in gem markets. On the other hand, blue sapphires from Muling have a pure blue color with no gray component. The variety of colors and the amount of fancy sapphires found in Muling are quite different from sapphires from other classic igneous deposits (see again Simonet et al., 2008).

At present, the precise location of the Muling gem deposit source rocks has not been confirmed. According to previous geological studies, the area is localized in the northern terminal of the branch of the Tanlu fault (Z. L. Qiu et al., "Trace element and hafnium isotopes of Cenozoic basalt-related zircon megacrysts at Muling, Heilongjiang Province, northeast China," *Acta Petrologica Sinica*, Vol. 23, No. 2, 2007, pp. 481–492). The lava in this region can be divided into six volcanic eruption cycles; Muling has experienced three such cycles (Sun et al., 2005).

Based on mining and geological information and our analysis of Muling rubies and sapphires, we inferred that this material might have originated as xenocrysts from an earlier volcanic eruption and undergone subsequent high-pressure geological processes. These are likely non-classic alkali basalt deposits. Large corundum deposits exist from eastern China to Primorye in far eastern Russia (I. Graham et al., "Advances in our understanding of the gem corundum deposits of the West Pacific continental margins intraplate basaltic fields," *Ore Geology Reviews*, Vol. 34, pp. 200–215), but exact locations have not been confirmed.

Although Muling's corundum deposit have yet to be mined commercially, the existing production has drawn the attention of Chinese gemologists and gem dealers. The production may rival that from other high-quality deposits, and this source holds great promise for the future.

Yimiao Liu and Ren Lu
Gemmological Institute, China University of Geosciences
Wuhan, China

"Star of David" spinel twin crystal with multiphase inclusions from Mogok. In December 2015, author VP obtained from the Mogok gem market a remarkable spinel crystal with a fascinating Star of David (figure 43). This unusual pattern was formed by two triangles on opposing sides of a central 12-sided polygon. Furthermore, the specimen hosted some conspicuous crystals that resembled fluid inclusions, which are rare in spinel. The stone was reportedly mined in the early 2000s near Pein Pyit, a village in eastern Mogok that is famous for such twinned spinel crystals (T. Themelis, *Gems & Mines of Mogok*, published by the author, Bangkok, 2008). Hundreds were found in the Mogok market between 2002 and 2004, but most were tiny or broken (V. Pardieu, "Hunting for 'Jedi' spinels in Mogok," Spring 2014 *G&G*,

pp. 46–57). The newly acquired crystal was added to the GIA reference collection. With a chemical formula of $MgAl_2O_4$, spinel belongs to the cubic crystal system. It is often found as octahedrons (with o faces), but sometimes dodecahedron d faces are visible. This specimen presents a fascinating case of twinning parallel to the octahedral plane O (111), commonly called "spinel-law" twinning. The general crystal outline is a 12-sided polygon instead of the expected hexagon. If a spinel crystal shows only o faces, a crystal flattened along the (111) plane will appear as a hexagon. But a spinel with both o and d faces that is flattened along the (111) octahedral plane will show 12 sides, as in this specimen.

The crystal hosted several fractures as well as interesting fluid and crystal inclusions. Fractures are very common in such thin crystals, causing them to break easily. This specimen broke during the cleaning process (figure 44), and extra care should be taken while handling such crystals.

One inclusion was a flat, opaque, and foliated black crystal (possibly graphite) that we could not identify with Raman spectroscopy. There were also carbonate inclusions (identified as calcite and dolomite using Raman spectroscopy). The most fascinating features were the multiphase inclusions; at least eight were located in the center of the specimen (figure 45). They were composed of a negative crystal filled with colorless liquid, hosting a flattened or spherical bubble, filled with a liquid and a gas. This was unlike the features in spinel from Man Sin, where negative crystals are filled with an orange liquid rich in sulfur (again, see Pardieu, 2014).

We assumed that the gas inclusions were mainly CO_2, as some of the small bubbles disappeared while the stone was under the microscope and gently heated by the well light. This could not be confirmed by Raman analysis; the CO_2 concentration in the solution may have been too low.

FTIR spectroscopy confirmed the presence of carbonates and oil in some fractures. This might be explained by the

Figure 43. This 12-sided crystal recently obtained in Mogok is a rare spinel macle, hosting fascinating multiphase (liquid + gas) inclusions. The stone is reportedly from the eastern part of the Mogok Valley. Photo by Victoria Raynaud/GIA; field of view 5.7 mm.

Figure 44. The Star of David spinel hosts some interesting multiphase inclusions. Such fractured, thin crystals are very brittle; this one was damaged during the cleaning process. Photo by Sasithorn Engniwat/GIA.
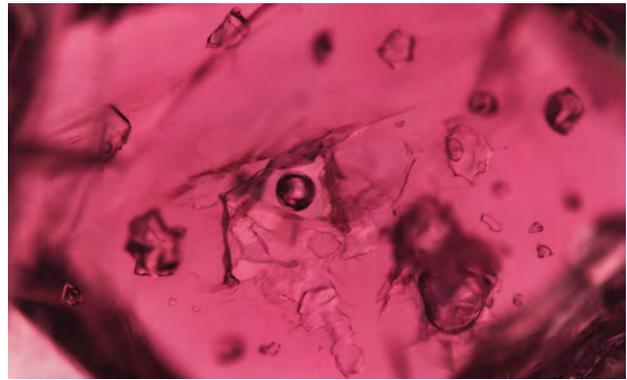

Figure 45. About five multiphase inclusions associated with colorless carbonate crystal are seen in the spinel's center, shown using diffused brightfield illumination. Photo by Victoria Raynaud/GIA; field of view 2.40 mm.

common practice (in Mogok) of keeping crystals in oil before selling them. We also studied the sample using photoluminescence and UV-Vis spectroscopy. The Cr^{3+} band in the PL spectra was approximately 0.89 nm wide. In the UV-Vis spectra, there was a clear absorption in the green around 537 nm. These features confirmed the absence of treatment (S. Saeseaw et al., "Distinguishing heated from unheated spinel," *GIA News from Research*, 2009, www.gia.edu/ongoing-research/distinguishing-heated-unheated-spinel).

The sample was analyzed using LA-ICP-MS. Three spots were studied and compared to GIA reference data obtained on other red spinels from different origins. The main trace elements observed were V, Cr, and Zn. Other elements (Li, Be, Ti, Mn, Fe, Co, Ni, and Ga) were also detected in lower but still significant concentrations. Based on GIA's reference data for origin determination, we would have identified these as Burmese, with other localities (Tanzania, Vietnam, or Tajikistan) excluded due to the elevated Zn and Ni content.

Star of David spinels are rare crystals that fascinate many gemologists and collectors. Studying these macles promotes our understanding of them and will contribute to origin determination for red spinel.

Vincent Pardieu, Supharart Sangsawong,
Wim Vertriest, and Victoria Raynaud

SYNTHETICS AND SIMULANTS

Large colorless HPHT synthetic gem diamonds from China. High-pressure, high-temperature (HPHT) technology for gem diamond synthesis has made rapid progress in the last few years. It is now being used to produce many melee-size diamonds around 2–3 mm in diameter and large colorless single crystals, all with significantly improved quality and growth rate. One Russian company is reportedly growing multiple large, gem-quality colorless diamond crystals in a single run (U.F.S. D'Haenens-Johansson et al., "Large colorless HPHT-grown synthetic gem dia-

monds from New Diamond Technology," Fall 2015 *G&G*, pp. 260–279). Here we report on large diamond crystals manufactured using a similar technology by Jinan Zhongwu New Materials Co. Ltd in Shandong, China.

We visited the Chinese factory in early March 2016 and obtained 50 crystals (figure 46). The crystals were examined using the instrumentation and techniques applied to all diamonds submitted to GIA for grading; all exhibited the typical characteristics of HPHT growth and were identified as synthetic. These were basically colorless, with only a few metallic inclusions observed. These crystals showed typical cuboctahedral morphology, with well-developed {100}, {110}, and {111} growth sectors and a weakly developed {113} sector. The crystals we obtained ranged from about 0.5 to 1.2 ct each. Absorption spectra in the infrared region showed they were type IIa diamond, but trace absorption from boron was detected (2800 cm^{-1}). Detailed gemological and spectro-

Figure 46. A factory in Shandong, China, is producing a large number of colorless HPHT synthetic diamonds for the jewelry industry. These crystals have typical cuboctahedral morphology and weigh up to 3.5 ct. Photo by Jian Xin (Jae) Liao.

scopic analyses are ongoing and will be reported separately. According to the manufacturer, large quantities of gem-quality colorless and blue diamonds are produced in this factory, in sizes up to 3.5 ct each. While the total production volume remains unclear, it is undoubtedly significant, and capacity is likely to expand in the near future. This strongly suggests that even more large HPHT synthetic diamonds will be introduced into the jewelry industry.

Wuyi Wang and Tom Moses
GIA, New York

TREATMENTS

Polymer-treated hessonite. Early in 2016, gem merchant Abdul Hafiz (Jaipur, India) showed this contributor a parcel of orangy brown rough hessonite he had purchased, said to be "glass-filled" hessonite. Upon initial observation, the specimens appeared to be treated, as individual crystals were stuck together (figure 47). This is commonly seen in glass-filled corundum rough; however, the typical glassy surface was absent. Rather, the surface appeared greasy, as if it was heavily oiled. Since the crystals were stuck together, it was obvious that some more stable form of treatment has been performed. Further testing was conducted to identify the treatment.

Under 10× magnification, the joints and cavities showed a concentration of a foreign substance that was readily indented with a metal pin, ruling out the presence of glass. Because of the unpolished surface, we could not see the filler, but the stone was transparent enough for infrared spectroscopy. The spectra showed strong features at approximately 3060, 3032, 2923, and 2871 cm^{-1}; these peaks are associated with polymer. Other absorption features were

Figure 47. These three rough hessonite samples (17.92 grams total) are joined by a polymer, which is also found in surface cavities and joints. The treatment is evident from the rough's "oily" look. Also note the visibility of fractures in the 5.31 ct (left) and 5.35 ct (right) cut samples. Photo by Gagan Choudhary.
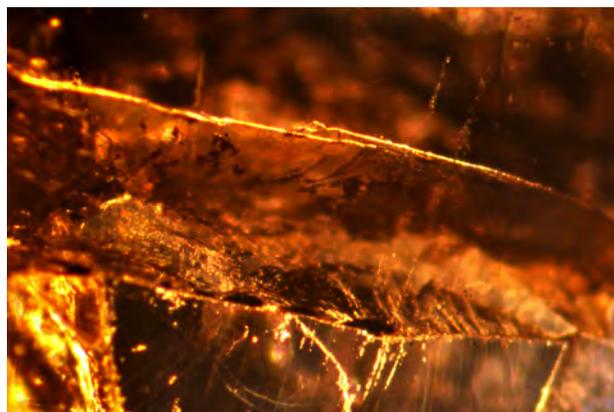
Figure 48. Fractures of the cut samples display thick and cloudy patches, suggesting uneven filling. Photomicrograph by Gagan Choudhary; image width 6.35 mm.

consistent with grossular garnet, specifically hessonite and tsavorite, according to the laboratory's database.

To check for a polymer filler and record gemological properties, two specimens were faceted, weighing 5.35 and 5.31 ct, respectively (again, see figure 47). Both specimens gave an RI of 1.745 and a hydrostatic SG of 3.60, within the range for hessonite (M. O'Donoghue, *Gems: Their Sources, Descriptions and Identification*, 6th ed. Butterworth-Heinemann, London, 2006). Both displayed a strong roiled or "heat wave" effect and numerous transparent rounded to elongated colorless crystals, features consistent with hessonite. The stones had obvious fractures visible to the unaided eye. When magnified, these fractures displayed thick and cloudy patches (figure 48), suggesting that a foreign substance was used to create an uneven filling. None of the iridescence or color flashes typically associated with a filled fracture were visible. Both faceted stones also displayed characteristic polymer-related peaks in IR spectroscopy.

This was our first encounter with a polymer-treated hessonite. Because the fractures were eye-visible, it is unclear how much value the treatment adds to these low-grade stones. According to Mr. Hafiz, the treatment is performed to stabilize the rough for cutting and polishing; otherwise the highly fractured material crumbles while processing. He added that hundreds of kilograms of such rough (reportedly African) have been sent to China for treatment.

Gagan Choudhary (gagan@gjepcindia.com)
Gem Testing Laboratory, Jaipur, India

ERRATUM

In the Winter 2015 GNI entry on grandidierite from Madagascar (pp. 449–450), the color of the sample was incorrectly presented in figure 4. Please go to www.gia.edu/gems-gemology/winter-2015-gemnews-grandidierite-madagascar to see its actual color.